



NTNU – Trondheim
Norwegian University of
Science and Technology

Atomistic Modeling of Fracture Mechanics Testing

Marie Jørum

Mechanical Engineering

Submission date: June 2015

Supervisor: Christian Thaulow, IPM

Norwegian University of Science and Technology
Department of Engineering Design and Materials

Preface

This report is the result of thesis work carried out at Norwegian University of Science and Technology (NTNU), for the Department of Engineering Design and Materials, during the spring semester of 2015. The extent of the thesis is 30 ECTS, expanding over a time frame of 20 weeks. The Master thesis is the conclusion of a five-year integrated Master of Science-program in Mechanical Engineering provided by NTNU. The work in this report is continued from the project thesis written autumn 2014, and hence certain parts are referred to the project rather than being elaborated in this report.

Parts of the modeling work have been executed in good cooperation with Ph.D. candidate Jørn Skogsrud. There has also been collaboration with Aksel L.L. Kvaal and Brage D. Snartland, who did similar physical experiments. Section 4.7 is dedicated to a comparison of results, and is a mutual section for all reports.

A compulsory risk evaluation was performed at the start of the semester, and this document can be found in Appendix D.

Marie Jørum
Trondheim, June 2015

Problem text

THE NORWEGIAN UNIVERSITY
OF SCIENCE AND TECHNOLOGY
DEPARTMENT OF ENGINEERING DESIGN
AND MATERIALS

MASTER THESIS 2015 FOR STUD.TECHN. MARIE JØRUM

ATOMISTIC MODELING OF FRACTURE MECHANICS TESTING

Atomistisk modellering av bruddmekanisk prøving

Modeling of the material properties at the nanoscale has become a reality. We have efficient and reliable programs, such as LAMMPS, and supercomputers, such as VILJE, available. In this Thesis the goal is to model nanosized cantilever beams with cracks in order to understand the detailed fracture mechanisms unfolding in the process zone at the crack tip. The material chosen is pure iron

The following tasks shall be performed

- Review the application of cantilever beam geometries in fracture mechanics, and the various requirements to obtain reliable results. Extend the application to the nanosize, and discuss the expected effects as a result of this change in dimensions.
- Review previous reports on atomistic fracture mechanics modeling. Highlight the main findings and challenges. Present a plan for your own modeling.
- Perform atomistic modeling and examine the effect of crystallographic orientations and the temperature. Other parameters, such as deformation rate, crack size and specimen size can also be included if time permits.
- Perform a detailed analysis of the processes accounting for the deformation and fracture in the process zone. This includes a detailed quantification of the dislocation activity
- Compare with experiments, based on FIB and nanomechanical testing.

Three weeks after start of the thesis work, an A3 sheet illustrating the work is to be handed in. A template for this presentation is available on the IPM's web site under the menu "Masteroppgave" (<http://www.ntnu.no/ipm/masteroppgave>). This sheet should be updated one week before the Master's thesis is submitted.

Performing a risk assessment of the planned work is obligatory. Known main activities must be risk assessed before they start, and the form must be handed in within 3 weeks of


properly covered by the general risk assessment shall be particularly assessed before performing the experimental work. Risk assessments should be signed by the supervisor and copies shall be included in the appendix of the thesis.

The thesis should include the signed problem text, and be written as a research report with summary both in English and Norwegian, conclusion, literature references, table of contents, etc. During preparation of the text, the candidate should make efforts to create a well arranged and well written report. To ease the evaluation of the thesis, it is important to cross-reference text, tables and figures. For evaluation of the work a thorough discussion of results is appreciated.

The thesis shall be submitted electronically via DAIM, NTNU's system for Digital Archiving and Submission of Master's theses.



Torgeir Welo
Head of Division



Christian Thaulow
Professor/Supervisor



NTNU
Norges teknisk-
naturvitenskapelige universitet
Institutt for produktutvikling
og materialer

Abstract

Nanomechanical testing has become a well-acclaimed way of researching material properties. Today, with supercomputers and advanced programming codes for Molecular Dynamics (MD) available, there is also the possibility of creating computational models of nano-sized specimens, such as pillars and cantilevers. MD gives us an opportunity to go into the very depths of the material: the atoms, and explore the mechanisms in a way not achievable in a physical test specimen. As the oil and gas activity is increasing in the Arctic region, MD is becoming a viable tool for exploring materials under difficult circumstances, and see how they are affected by external factors such as very low temperature.

An atomistic model of a full-3D, nano-sized, pre-notched cantilever beam has been made. It has a simulated indenter force embedded, and MD simulations have been performed to deflect the beam and initiate crack growth. The crucial process zone in front of the crack has been investigated with respect to linear elastic fracture mechanics, elastic-plastic fracture mechanics and plastic deformation mechanisms such as dislocations and twinning. The effect of crystallographic orientation, crack geometry and loading rate has been studied. The stress intensity factor K has been calculated with three different approaches. In addition, the J -integral and energy release rate \mathcal{G} have been computed.

The cantilevers proved to be highly affected by crystallographic orientation, displaying very different behavior from orientation to orientation. The loading rate did not appear to notably affect the fracture behavior, however, the two loading rates investigated are not highly different from each other, especially when compared to physical experiments. An even longer simulation would be exciting to examine, if time allows in future research. Two different crack geometries were also compared, one sharp and one round. The difference in crack geometry didn't affect the overall behavior of the crack growth as much, but in general, the sharp crack produced cleaner, more brittle crack growth.

The quantitative results showed that the K -calculations have expected results, based on previously obtained results. The energy release rate was obtained, and combined with the measured Crack Tip Opening Displacement (CTOD) used to find values for the yield stress, which fell within the expected range. The values acquired for J were compared with \mathcal{G} , and found to be a bit high. Some refining of the method used to obtain J is probably needed for the values to be more precise on this level.

The atomistic model was compared to physical testing of a cantilever beam. The calculated K and J were lower for the modeled cantilever than for the physical ones, which was explained by the difference in loading rate, notch geometry, specimen size and material purity.

Sammendrag

Nanomekanisk testing har blitt en anerkjent måte å undersøke et materials egenskaper. Nå, med tilgjengelig høyteknologi som superdatamaskiner og avansert programkode for molekylærdynamiske (MD) beregninger, finnes muligheter for å lage datamodeller av prøver helt ned til nanostørrelse. Med MD får man muligheten til å gå inn i selve dybden i materialet: atomene, og man får undersøkt mekanismene på en måte som ikke er oppnåelig i en fysisk prøve. Med den stadig voksende olje og gass-aktiviteten i Arktis, er MD et stadig mer pålitelig verktøy for utforskning av materialer i vanskelige miljø, og se hvordan de blir påvirket av utenforliggende faktorer som veldig lav temperatur.

Det ble laget en atomistisk modell i nanostørrelse og full 3D av en utkragerbjelke med sprekk. Den har en innebygget last for simulering av indenter, og bruddmekaniske forsøk ble utført ved hjelp av MD-beregninger: bjelken ble nedbøyd for å igangsette sprekkvekst. Den kritiske sonen foran sprekkfronten ble undersøkt med tanke på lineærelastisk bruddmekanikk, elastiskplastisk bruddmekanikk og plastisk deformasjon i form av dislokasjoner og twinning. Påvirkning av krystallografisk orientering, sprekkgeometri og deformasjonshastighet ble vurdert. Spenningsintensitetsfaktoren K ble funnet med tre forskjellige tilnæringsmetoder. I tillegg ble J -integralet og energifrigivelsesrate G regnet ut.

Utkragerbjelkene viste seg å bli svært påvirket av orientering, og utviste forskjellig oppførsel seg i mellom. Deformasjonshastigheten påvirket ikke bruddoppførselen nevneverdig, men de to hastighetene som ble testet er ikke veldig forskjellige i det store bildet, særlig ikke sammenlignet med fysiske forsøk. En enda lenger simulering ville vært spennende å se utfallet av, om tiden tillater i fremtidig arbeid. To forskjellige sprekkgeometrier ble sammenlignet, en skarp og en rund. Forskjellen i sprekk påvirket ikke den generelle sprekkoppførselen i stor grad, men den skarpe sprekken produserte litt sprøere og renere sprekkvekst.

De kvantitative resultatene fortalte at utregningene for K ga forventede, rimelige utfall, basert på tidligere oppnådde resultater. Energifrigivelsesraten ble funnet, og kombinert med den målte CTOD ble det kalkulert verdier for flytspenning, verdier som falt fint innenfor forventet intervall. De oppnådde verdiene for J ble sammenlignet med G , og funnet litt høye. Metoden brukt for å finne J må sannsynligvis gjennom en justeringsprosess for å bli mer nøyaktig i denne typen simuleringer.

Den atomistiske modellen ble sammenlignet med fysiske forsøk. De oppnådde verdiene for K og J viste seg lavere for modellen enn for de fysiske prøvene, noe som ble forklart ved forskjell i deformasjonshastighet, sprekkgeometri, prøvestørrelse og materialets renhet.

Nomenclature

a	Notch Depth
E	Young's Modulus of Elasticity
\mathcal{G}	Energy Release Rate
J	J-Integral
K	Stress Intensity Factor
K_Q	Conditional Stress Intensity Factor
K_{IC}	Critical Stress Intensity Factor
L	Bending Length
w	Specimen Width
Å	Ångström, 10^{-10} m
γ_s	Surface Energy
γ_{us}	Unstable Stacking Energy
δ	Crack Tip Opening Displacement
ε	Strain
ν	Poisson's Ratio
σ	Stress
σ_y	Yield Stress
BCC	Body-Centered Cubic
BOP	Bond-Order Potential
CMOD	Crack Mouth Opening Displacement
CTOD	Crack Tip Opening Displacement
EAM	Embedded Atom Method
EPFM	Elastic-Plastic Fracture Mechanics
FCC	Face-Centered Cubic
HCP	Hexagonal Close-Packed
LAMMPS	Large-Scale Atomic/Molecular Massively Parallel Simulator
LEFM	Linear Elastic Fracture Mechanics
MD	Molecular Dynamics

Table of Contents

Preface	I
Problem text	III
Abstract	V
Sammendrag	VII
Nomenclature	IX
Table of Contents	XI
1 Introduction	1
2 Theoretical Background	3
2.1 Molecular Dynamics	3
2.1.1 Interatomic Potentials	4
2.2 Crystallography	4
2.3 Dislocation Theory	5
2.3.1 Deformation of BCC Metals	8
2.3.2 Dislocation Loops.....	8
2.3.3 Twinning	9
2.3.4 Crystal Analysis Tool.....	9
2.4 Fracture Mechanisms	10
2.4.1 Brittle Fracture	10
2.4.2 Ductile Fracture	10
2.4.3 Triaxiality	10
2.5 Linear Elastic Fracture Mechanics	11
2.5.1 Stress Intensity Factor	11
2.5.2 Energy Release Rate.....	14
2.6 Elastic-Plastic Fracture Mechanics	15
2.6.1 <i>J</i> -integral.....	15
2.6.2 Crack Tip Opening Displacement	17
2.7 Atomistic Modeling of Fracture	18
2.7.1 Brittle vs. Ductile Response	19
3 Modeling and Simulation	21
4 Results and Discussion	27
4.1 Effect of Crystallographic Orientation	27
4.2 Effect of Loading Rate	33
4.3 Effect of Crack Geometry	34
4.4 Dislocation Analysis	37
4.5 Linear Elastic Fracture Mechanics Approach	45
4.5.1 Stress Intensity Factor	45
4.5.2 Energy Release Rate.....	46
4.6 Elastic-Plastic Fracture Mechanics Approach	48
4.6.1 <i>J</i> -integral.....	48
4.6.2 Stress Intensity Factor	51
4.6.3 Crack Tip Opening Displacemen	52
4.7 Comparison with Physical Experiments	54
4.8 Remarks	56
5 Conclusion	59
6 Further Work	61

7	References	63
8	Acknowledgments.....	65
	Appendix A: <i>J</i>-Δa Plots.....	67
	Appendix B: Through-thickness Crack Growth.....	69
	Appendix C: Input Script.....	71
	Appendix D: Risk Evaluation.....	79

1 Introduction

The Arctic region is becoming more and more important for the modern oil and gas industry. This is a part of the world known for its particularly rough environment, with temperatures down to -60°C , ice accumulation and harsh weather. Engineering materials today are not designed for these conditions, and because of the growing activity in the Arctic there is an increasing need to find out how materials behave when paired with this environment. Today's technology and high-end supercomputers allow us to explore materials in a way not even comprehensible a couple of decades ago. Molecular dynamics (MD) break the material down to the atomic level, and we get to see how each atom performs under certain constraints and conditions. It allows us to choose atoms with certain characteristics, such as high energy, high stress etc. This gives a wonderful opportunity to explore the material in a way that is not achievable in a physical specimen.

The main objective of this thesis is to examine an atomic model of a pre-notched cantilever beam, and to research the fracture mechanisms at the process zone near the crack tip. Load is applied to deflect the beam and initiate crack growth, and then the fracture behavior can be analyzed in a detailed way. Fracture occurs by either a brittle or a ductile manner, and which one wins the competition between the two is not always easy to figure out. Similar physical experiments are done concurrently in the lab, and the purpose is to match the simulations to physical experiments as closely as possible. Certain factors tend to affect the outcome, such as the orientation of the crystals, temperature and loading rate. A schematic illustration of the procedure is presented in Figure 1.

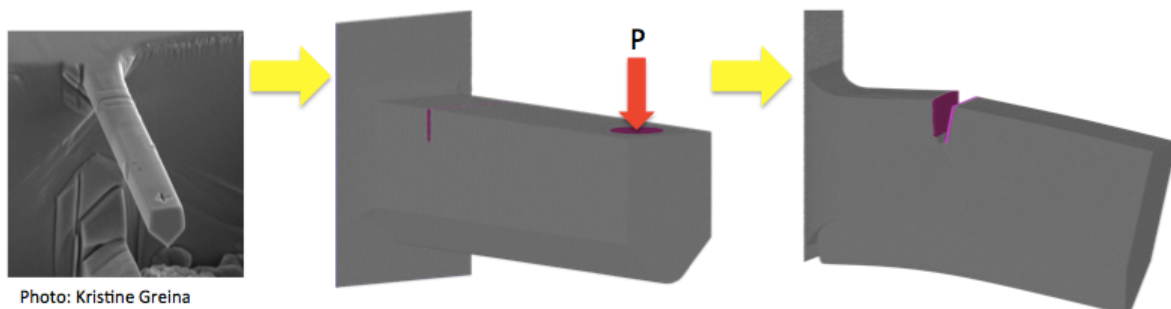


Figure 1: A schematic illustration of the procedure done in this thesis, from physical cantilever on the nanoscale to atomistic model.

In the work presented in this report, the effect of crystallographic orientation, loading rate and crack geometry are investigated. An analysis of the dislocation activity has been performed. The stress intensity factor K and the J -integral were calculated for the cantilevers. Three approaches to the geometric shape factors were considered in these calculations. The relationships between J , K and energy release rate \mathcal{G} were further explored to obtain values for

the yield stress. In addition, a section is dedicated to the comparison of the atomistic model and physical cantilever beams.

There are still many obstacles to overcome before the atomistic world truly meets the physical world. MD simulations are dependent on computational power, and this provides limitations in both sample size and run time. But the technology is improving every day, and so far, MD simulations and atomistic modeling serve as a good tool in materials science.

The contents of this report is organized as follows: In chapter 2, the relevant background theory to understand the results is presented, including a summary of previous findings in atomistic modeling of fracture in order to highlight some expected, or unexpected, results. Chapter 3 presents the model and simulation details used to perform the work. In chapter 4, the results of the simulations and calculations are presented and discussed with regards to theory and previously obtained results. The findings are concluded in chapter 5, and a proposal for further work on the subject is listed in chapter 6.

2 Theoretical Background

This chapter will present relevant background theory, explaining the observations later done in the experiments, as well as the methods used for analysis of the results. As the chosen material in this thesis is pure iron, the theory focuses on properties for body-centered cubic (BCC) crystals.

The chapter starts off by giving a brief introduction to molecular dynamics, as this is the main tool used to perform the work in this thesis. It is followed by an overview of the BCC crystal, explaining the crystallographic planes and directions embedded in a unit cell. These planes and directions are important in the next section, where plastic deformation mechanisms such as dislocation and twinning are presented. After this the main fracture mechanisms are summarized, and then the methods for obtaining stress intensity factor K and the J -integral are presented in detail. These methods are divided into two sections, one for linear elastic fracture mechanics and one for elastic-plastic fracture mechanics. Lastly, a summary of previous findings in atomistic modeling of fracture is found in section 2.7. The results obtained in the thesis work are later compared and discussed with regards to the theory presented here.

2.1 Molecular Dynamics

Molecular Dynamics (MD) has the purpose of simulating the trajectory of atoms. It does so by utilizing Newton's second law of motion over a series of discrete time steps. For an ensemble of N particles, equation (1) is integrated for each particle $i=1\dots N$.

$$\vec{F}_i = m_i \vec{a}_i \quad (1)$$

where m_i is the mass of each particle i , a_i its acceleration and F_i the force acting upon it due to interaction with other atoms. A molecular dynamics simulation gives us information of atom positions r_i , velocities v_i and accelerations a_i , which in turn can be used to study material behavior [1].

A molecular dynamics simulation can be broken down into three work packages: input, simulation and output, visualized in Figure 2.

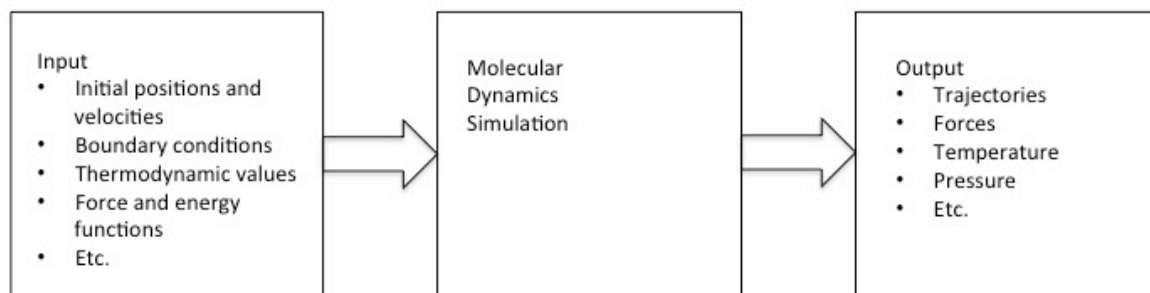


Figure 2: The three steps of molecular dynamics, with keywords of a typical input and output.

The input, in the form of a script, is where all parameters are defined, such as interatomic potential, model geometry, forces, boundary conditions etc., in addition to choosing what data to output. The second work package, the simulation, is in itself divided into two parts: relaxation and production. The purpose of the relaxation phase is to redistribute the energy so that the atoms reach their equilibrium state. The production part is the recording of necessary data. The output data comes in two forms: the log file and the dump file. The log file is a text file containing quantitative data; in the case of this thesis data such as beam deflection, load, CTOD/CMOD measurements etc. The dump file is used for visualization of the model, and typically outputs positions, energy, stress, among other things, for each atom at each chosen time step.

A more detailed description of the technicalities of MD is described in the project work [2] preceding this thesis.

2.1.1 Interatomic Potentials

Interatomic potentials for iron are usually of the Embedded Atom Method (EAM) type [3], though some Bond-Order Potentials (BOP) also exists. The EAM potential is quite computationally inexpensive, and as it is known to correctly predict the sixfold symmetry of screw dislocation cores it is well suited for simulations where dislocation emission is expected. The BOP differs from the EAM potential by taking directional bonding into consideration. This makes it more accurate, but also more computationally expensive, and it is sometimes needed in special cases that require a high level of accuracy.

2.2 Crystallography

Iron forms a body-centered cubic (BCC) crystal, where a unit cell is recognized by the sharing of atoms with surrounding crystals in all eight corners, in addition to having an atom in the center of the crystal, depicted in Figure 3.

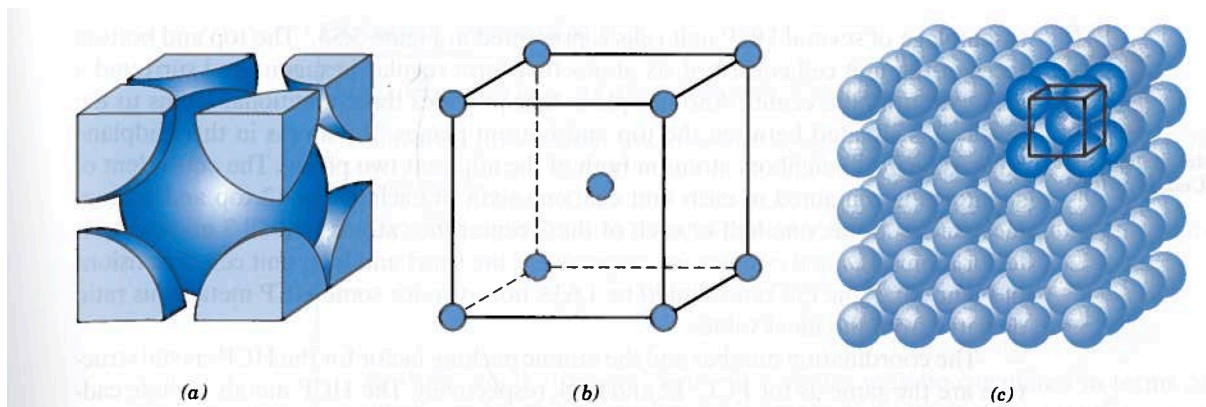


Figure 3: The BCC crystal: (a) full hard-sphere, (b) reduced-sphere unit cell, (c) the BCC unit cell in an array of crystals. Adapted from [4]

Within a crystal structure, there are several planes and directions that have great significance when it comes to a material's properties. Crystallographic directions are effectively vectors in terms of lattice dimensions abc corresponding to a global coordinate system xyz , as shown in Figure 4. A specific direction is put in square brackets [...], whereas angle brackets (...) represent a family of directions, i.e. directions that are symmetrically equivalent. Negative indices are denoted with a bar over the current index. For example, $[100]$, $[010]$, $[001]$, $[\bar{1}00]$, $[0\bar{1}0]$ and $[00\bar{1}]$ are equivalent and belong in the $\langle 100 \rangle$ family [4].

Crystallographic planes are specified by *Miller indices* (hkl). The Miller indices describe the orientation of a plane or a set of planes within a lattice in relation to the unit cell. Correspondingly to the crystallographic directions, a specific plane is put in parentheses (...), and a family of symmetrically equivalent planes are put in braces {...}. Parallel planes are equivalent and have the same indices. An interesting feature of cubic crystals is that a direction and a plane with the same indices are perpendicular to one another [4].

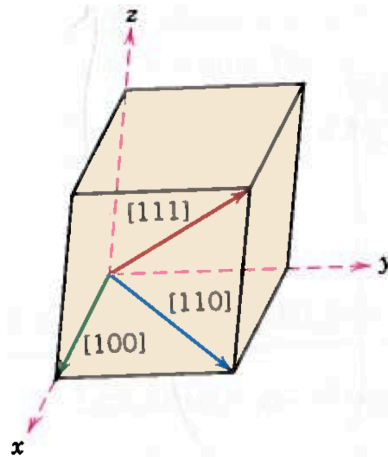


Figure 4: Three common directions, $[100]$, $[110]$ and $[111]$ shown inside a unit cell for reference. Adapted from [4].

2.3 Dislocation Theory

Metallic materials generally deform in two manners: *elastic* and *plastic*. Elastic deformation is reversible and exhibits linear behavior, while plastic deformation is irreversible and permanent and will occur after a certain stress limit is exceeded. An insight into the plastic deformation of BCC, such as dislocations and twinning, is presented in this section, with the main focus being on dislocations and their characteristics. A tool used to analyze dislocations in atomistic models is presented briefly towards the end of the section.

Plastic deformation usually happens due to a mechanism called *dislocation*, which occurs when adjacent atomic layers move relative to one another; their atomic bonds break and they re-bond with new neighboring atoms. Dislocations tend to happen along the densest packed atomic directions and planes within the crystal, also known as *slip systems*. There are two main dislocations types: screw dislocations and edge dislocations, depicted in Figure 5 [4].

Dislocations with both screw and edge characteristics are called mixed dislocations. Pure edge and screw dislocations are rarely seen in physical experiments; most observed dislocations are of mixed nature [5].

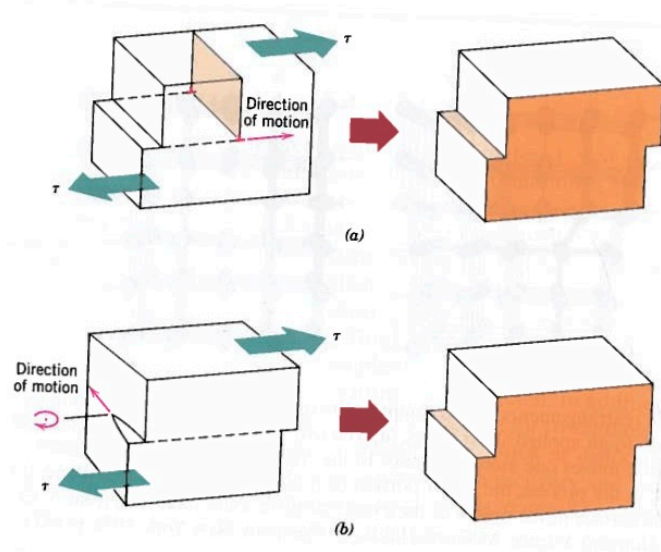


Figure 5: (a) Edge dislocation. (b) Screw dislocation. τ is shear stress. Note that the net plastic deformation is the same for both mechanisms. Adapted from [4].

A characteristic shear stress is required for slip to happen. Consider Figure 6, where a cylindrical crystal is loaded in tension. The tensile stress for such a configuration is $\sigma = P/A$, with A being the top surface area of the cylinder. The force P has a component in the slip direction, $P \cos \lambda$, working on the slip plane area $A / \cos \phi$. This yields that the *shear stress τ , resolved on the slip plane* is

$$\tau = \frac{P}{A} \cos \lambda \cos \phi \quad (2)$$

Where P is the applied force, A is the relevant area, λ is the angle between the force and the slip direction and ϕ is the angle between the force and the normal direction to the slip plane, all depicted in Figure 6. The quantity $\cos \lambda \cos \phi$ is called the *Schmid factor*. If P_c is the critical force at the point of slip, then τ_c is the corresponding, *critical resolved shear stress (CRSS)* for slip [5].

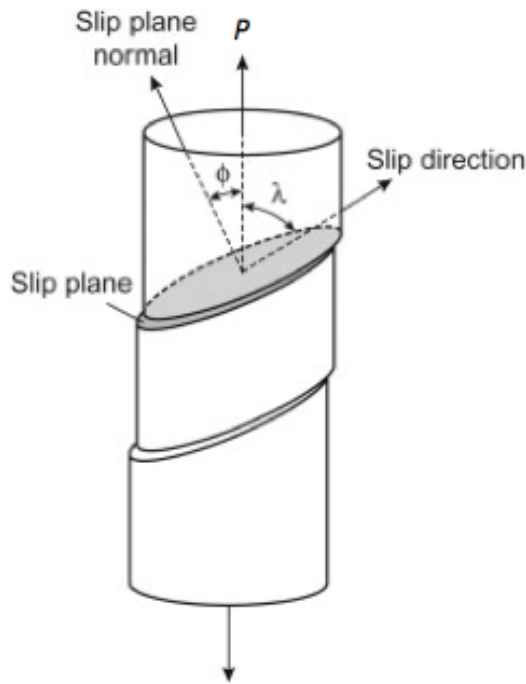


Figure 6: Depiction of slip. P is the acting force. Adapted from [5].

An important factor when considering dislocations is the *Burgers vector*, usually denoted \mathbf{b} . \mathbf{b} is a vector, describing the magnitude and direction of lattice distortion caused by dislocations. It is obtained by drawing an atom-to-atom path containing the relevant dislocation through only non-distorted crystals; see Figure 7. This path is known as the *Burgers circuit*, and the vector needed to complete the circuit is the Burgers vector [5].

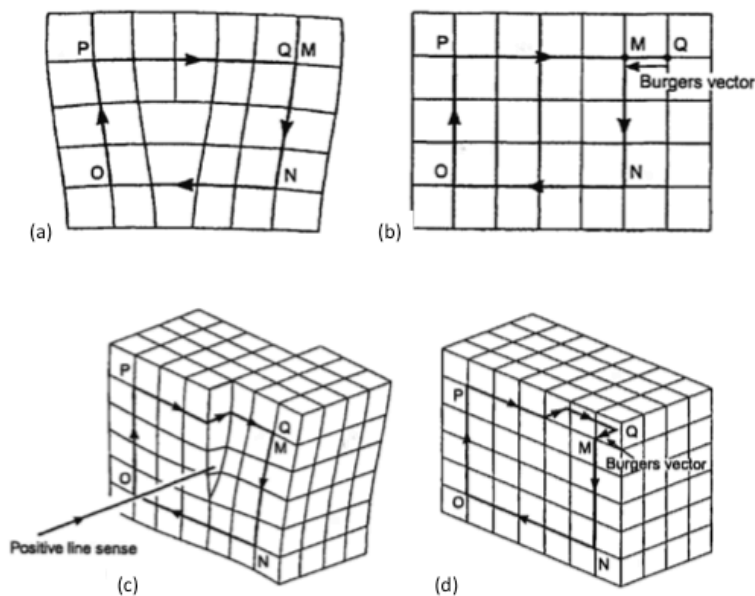


Figure 7: (a) Burgers circuit in an edge dislocation, (b) the same circuit on a perfect crystal, with Burgers vector described. (c) Burgers circuit in a screw dislocation, (d) the same circuit and Burgers vector shown, in a perfect crystal lattice. Adapted from [5]

For an edge dislocation, the Burgers vector is perpendicular to the dislocation line, whereas for a screw dislocation Burgers vector is parallel to the dislocation line. A mixed dislocation will thus have a Burgers vector with an arbitrary angle to the dislocation line [5].

Dislocations move in two ways: *glide* or *climb*. Glide is considered *conservative* motion, and occurs when the dislocation moves on the surface containing both the Burgers vector and the dislocation line. Climb, or *non-conservative* motion happens when the dislocation moves out of the glide plane, and thus normal to Burgers vector [5].

2.3.1 Deformation of BCC Metals

The slip systems for BCC materials are displayed in Table 1. The Burgers vector for a perfect slip dislocation, i.e. the shortest lattice vector, is of the type $\frac{1}{2}\langle 111 \rangle$.

Table 1: The available slip systems for BCC materials. Adapted from [4].

Slip Plane	Slip Direction	Number of Slip Systems
{110}	$\langle \bar{1}11 \rangle$	12
{211}	$\langle \bar{1}11 \rangle$	12
{321}	$\langle \bar{1}11 \rangle$	24

It is of particular interest that three {110}, three {211} and six {321} planes intersect on the same $\langle 111 \rangle$ direction, allowing screw dislocations to move on different planes of the same family or combinations of plane families, favored by the applied stress. This makes BCC dislocations complicated, and often poorly defined. Another interesting feature of the BCC crystal is its asymmetry of slip: the slip system activated due to compression is not the same as the system activated by tension. Hence, the shear stress needed to move a dislocation in a certain direction would not move the dislocation similarly in the opposite direction[5].

In certain dislocation networks, another set of perfect dislocations for BCC materials are occasionally observed; those with Burgers vector $\langle 100 \rangle$. These are believed to occur from a combination of two perfect $\frac{1}{2}\langle 111 \rangle$ dislocations [5]:

$$\frac{1}{2}[1\bar{1}1] + \frac{1}{2}[11\bar{1}] \rightarrow [100] \quad (3)$$

2.3.2 Dislocation Loops

A dislocation cannot end in a perfect crystal, and will therefore keep going until it meets a defect or a surface, or it will create a full loop. The loops can consist of edge or screw, as well as mixed characteristics. Dislocations loops are thought to nucleate with a Burgers vector

$\frac{1}{2}\langle 110 \rangle$ on $\{110\}$ planes. These partial dislocation loops strive to become perfect, so they shear at an early stage of growth, and become perfect by two possible reactions; equations (4) and (5) [5].

$$\frac{1}{2}\langle 110 \rangle + \frac{1}{2}\langle 001 \rangle \rightarrow \frac{1}{2}\langle 111 \rangle \quad (4)$$

$$\frac{1}{2}\langle 110 \rangle + \frac{1}{2}\langle 1\bar{1}0 \rangle \rightarrow \langle 100 \rangle \quad (5)$$

2.3.3 Twinning

Twinning is another form of metal deformation, known to occur in BCC material when it is deformed under high strain rate and/or low temperature. As an MD simulation is known for its high deformation rate, twinning is expected to occur in the present work. When twinning occurs, the atoms move in such a way that the new atomic structure mirrors the original structure, see Figure 8. BCC twinning happens on $\{112\}\langle 111 \rangle$ systems. The required shear to produce a twin in this system is obtained by a displacement of $\frac{1}{6}\langle 111 \rangle$ on $\{112\}$ planes, i.e. the Burgers vector for a twin dislocation is $\frac{1}{6}\langle 111 \rangle$ [5].

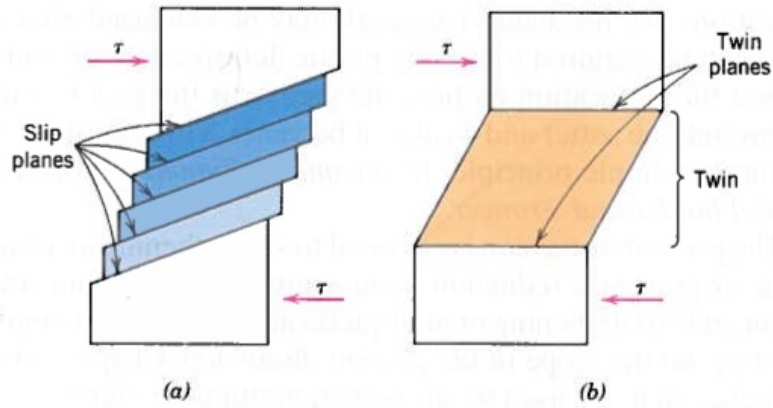


Figure 8: (s) Slip and (b) twinning. τ is shear stress. Adapted from [4].

2.3.4 Crystal Analysis Tool

A tool to detect and consider dislocations in atomistic simulation is the Crystal Analysis Tool. This is a computer code developed by Alexander Stukowski [6] [7] to analyze the output of atomistic simulations of solids. It will read a LAMMPS dump file, and implement algorithms to identify lattice structures and defect structures formed by atoms. The code is used in this work to detect dislocation lines and identify their Burgers vector, by the use of the Dislocation Extraction Algorithm (DXA).

2.4 Fracture Mechanisms

Modern fracture mechanics is usually divided into two parts: linear-elastic fracture mechanics (LEFM), and elastic-plastic fracture mechanics (EPFM). LEFM is based on material deformation that obeys Hooke's law¹, and works well for those cases. However, it's restricted in its use for nonlinear material, as it requires the structure's global behavior to be linear and elastic. This is where the EPFM comes in, with parameters that take nonlinear and plastic behavior into consideration, and thus making it more applicable for engineering problems [8].

A material fractures when the energy in the system is high enough to break the atomic bonds. The fracture mechanism is either ductile or brittle. These two mechanisms are further explained in the following sections.

2.4.1 Brittle Fracture

On an atomic level, brittle fracture is characterized by repetitive bond breaking. It is recognized by rapid, unstable crack propagation, and little plastic deformation. Most metallic materials that break in a brittle manner do so by cleavage fracture, a transgranular mechanism that crosses grain boundaries and move along specific crystallographic planes. The preferred cleavage planes are those with the lowest packing density (note: the opposite of preferred slip planes), as the spacing between planes is greater and hence fewer bonds must be broken for the cleavage to propagate [8].

2.4.2 Ductile Fracture

Ductile materials usually fail by micro void coalescence, due to either inclusions or second-phase particles. The crack growth is generally slow, and a considerable amount of plasticity develops at the crack front. The plastic zone near the crack tip dominates, and the materials resistance to fracture increases as the crack grows. On the atomic level, ductile crack growth is recognized as the shearing of adjacent atomic layers, initiating dislocation emission [9].

2.4.3 Triaxiality

Many engineering problems today are simplified by changing a three-dimensional state of stress into a biaxial stress problem. These stress states are referred to as plane strain and plane stress, respectively. Plane stress generally describes thin specimens, where one of the stress components is zero. Plane strain is applied to thicker specimens, and one of the strain vectors is set to be zero. Plane stress situations are much easier to handle computationally, but they are not very realistic.

¹ Hooke's law: $\sigma = E\varepsilon$

A thick, cracked specimen has significantly larger stresses near the crack front than in the bulk material. The elevated stresses normal to the crack plane, e.g. x-direction, will cause the y- and z-directions to want to contract. They will, however, be restricted to do so by the surrounding material, causing a triaxial state of stress in front of the crack in the middle of the specimen. The stress in the crack front direction will decrease closer to the free edge of the specimen, and on the very edge there will be a state of plane stress [8].

Tunneling is a phenomenon derived from triaxial problem, when a crack grows faster in the middle of the specimen due to the triaxial state and elevated stress there, making a tunnel-like crack growth [8].

2.5 Linear Elastic Fracture Mechanics

This section is dedicated to the introduction of two typical LEFM parameters, the stress intensity factor K and the energy release rate \mathcal{G} . The methods, which will be used later to obtain K , are presented, and the relationship between \mathcal{G} and K is identified.

2.5.1 Stress Intensity Factor

The stress intensity factor K is one of the most important factors in linear elastic fracture mechanics. K describes the stress field very close to the crack tip, where the process zone is dominated by the $\frac{1}{\sqrt{r}}$ singularity. K is usually denoted I, II or III based on what mode of loading is applied to the specimen, where mode I is tensile loading, mode II is in-plane shear and mode III is out-of-plane shear.

The critical stress intensity factor is given as

$$K_{Ic} = \sigma_c \sqrt{\pi a} \cdot F \quad (6)$$

where σ_c is the critical stress at fracture, a is the crack size and F is a geometric factor. Within certain validity criteria [10], see equation (7), K_{Ic} can be viewed as a material specific parameter and qualifies as the material's fracture toughness.

$$w, a, (h - a) \geq 2.5 \left(\frac{K_{Ic}}{\sigma_y} \right)^2 \quad (7)$$

where w is the specimen thickness, a is the notch depth, h is the height of the specimen and σ_y is the yield stress. Equation (7) is derived from the plastic zone size being proportional to K_{Ic}^2/σ_y^2 , and the thickness, ligament size and notch depth need to be considerably bigger than the plastic zone for LEFM to be applied. If the calculated K -value does not fall within these criteria, it is usually denoted K_Q , the *conditional K*, and cannot be quantified as the specific material's fracture toughness. For specimens on the nanoscale, it is often difficult to obtain parameters that match equation (7) due to very small sizes and large stress values. It is

therefore a good assumption to denote the K in equation (6) with a Q , and rather check the outcome's validity with eq. (7) to see if it can be classified as K_{IC} .

The literature reports many findings on K -calculations, and there are some different approaches to the geometric factor F . Many reports are based on a cantilever beam with square cross section, and to the best of author's knowledge only two papers report pentagonal cross section beams; Zhao et al. [11] and Di Maio and Roberts [12].

Zhao et al. used the following approach to obtain values for K_Q

$$K_Q = \sigma_c \sqrt{\pi a} \cdot F \left(\frac{a}{h} \right) \quad (8)$$

$$\sigma_c = \frac{PLy}{I} \quad (9)$$

where P is applied load, L is the length from notch to indenter center, y is the vertical distance between the upper surface and the neutral plane and I is the moment of inertia for the beam's cross section. I and y are given by equations (10) and (11), respectively.

$$I = \frac{wh^3}{12} + \left(y - \frac{h}{2} \right)^2 hw + \frac{w^4}{288} + \frac{w^2}{4} \left[\frac{h}{6} + (h - y) \right]^2 \quad (10)$$

$$y = \frac{\frac{h^2 w}{2} + \frac{w^2}{4} \left(h + \frac{w}{6} \right)}{hw + \frac{w^2}{4}} \quad (11)$$

h and w are shown in Figure 9 (a). The geometric factor is given by

$$F \left(\frac{a}{h} \right) = 1.122 - 1.121 \left(\frac{a}{h} \right) + 3.74 \left(\frac{a}{h} \right)^2 + 3.873 \left(\frac{a}{h} \right)^3 - 19.05 \left(\frac{a}{h} \right)^4 + 22.55 \left(\frac{a}{h} \right)^5 \quad (12)$$

Di Maio and Roberts altered the cross section parameters a little; making the height half the size, see Figure 9 (b). For this geometry they proposed the following solution for the geometric factor

$$F \left(\frac{a}{h} \right) = 1.85 - 3.38 \left(\frac{a}{h} \right) + 13.24 \left(\frac{a}{h} \right)^2 - 23.26 \left(\frac{a}{h} \right)^3 + 16.8 \left(\frac{a}{h} \right)^4 \quad (13)$$

Wurster et al. [13] have a different approach. They use the ASTM E-399 [10] standard to obtain K_Q , defined as

$$K_Q = \frac{P_Q L}{wh^{3/2}} \cdot F\left(\frac{a}{h}\right) \quad (14)$$

where P_Q is the critical force as determined by said standard, L , a , w and h are depicted in Figure 10 and $F\left(\frac{a}{h}\right)$ is given by

$$F\left(\frac{a}{h}\right) = 4 \frac{3\left(\frac{a}{h}\right)^{0.5} \left(1.23 - \left(\frac{a}{h}\right) \left(1 - \left(\frac{a}{h}\right)\right) \left(-6.09 + 13.96 \left(\frac{a}{h}\right) - 14.05 \left(\frac{a}{h}\right)^2\right)\right)}{2 \left(1 + 2 \left(\frac{a}{h}\right)\right) \left(1 - \left(\frac{a}{h}\right)\right)^{1.5}} \quad (15)$$

This factor is however intended for a beam with a square cross section, and needs some modification for usage on pentagonal cross section. One way to modify is to add the mean height of the triangular part below the square to the original height h in the calculations, and by this averaging the cross section area with a new value h^* :

$$h^* = h + \frac{w}{4} \quad (16)$$

h^* is also depicted in Figure 9. The cantilevers in this thesis have a pentagonal cross section, but a lot of the work that is described in the upcoming section is based on the Wurster approach, and thus this approximation is included.

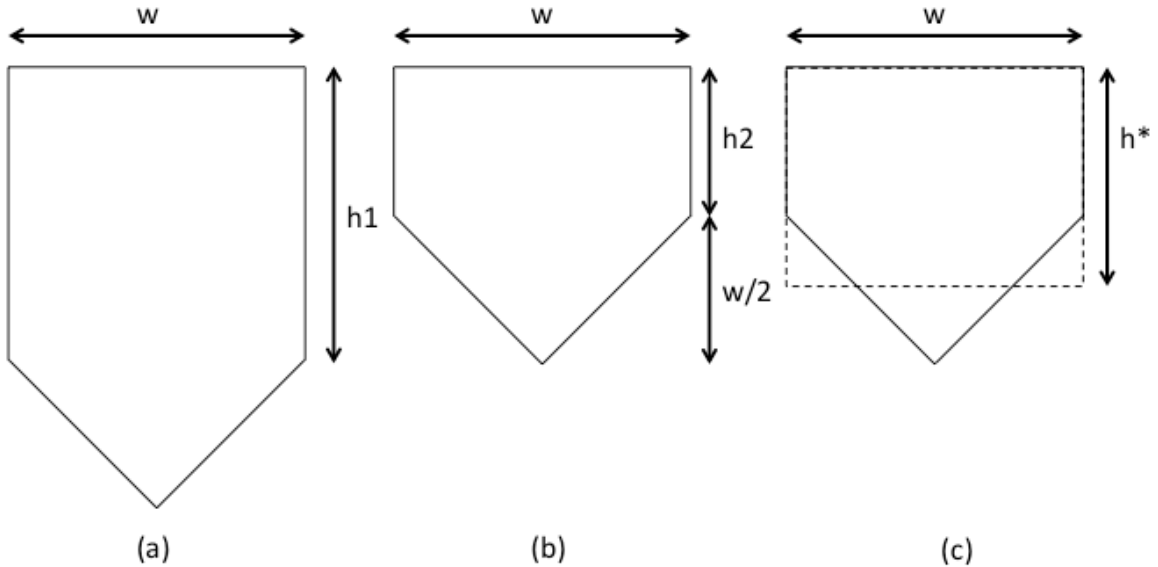


Figure 9: The two different cross section of the beam: (a) cross section for equation (12); (b) cross section for eq. (13). (c) is a graphical depiction of h^* , used in eq. (15)

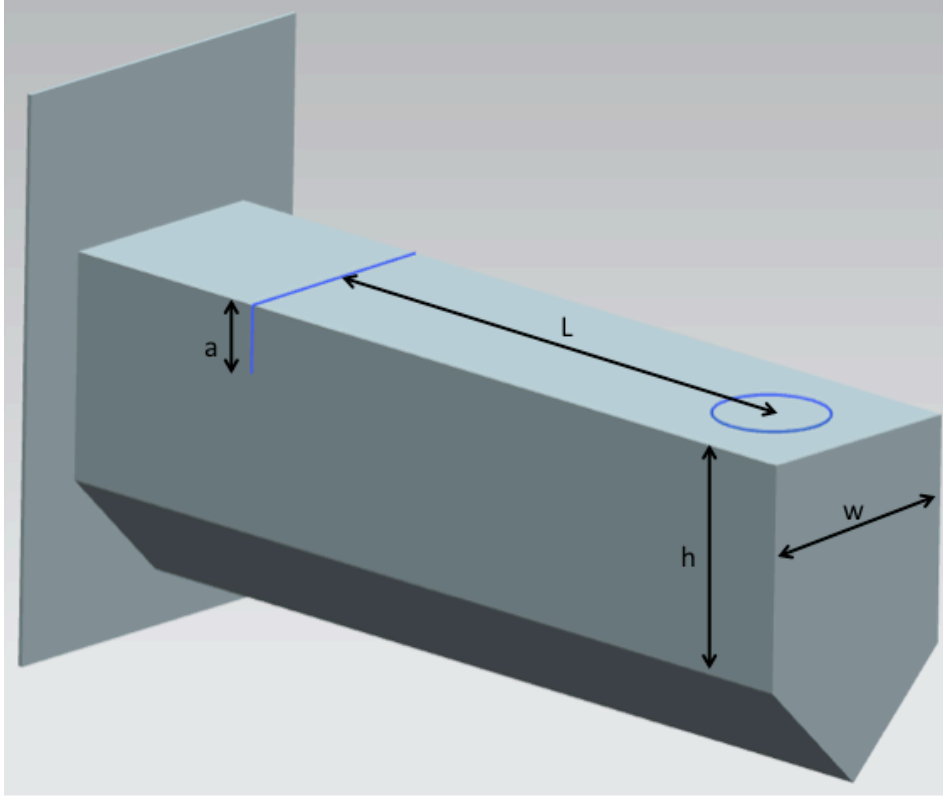


Figure 10: The parameters used in equations (8)-(15). The blue circle on the top beam surface is the point of the simulated indenter force, and the blue lines closer to the support wall represent the crack.

2.5.2 Energy Release Rate

Another important LEFM parameter is the *energy release rate* \mathcal{G} . This is the energy needed to create two new surfaces, i.e. the energy needed for crack extension in a brittle material

$$\mathcal{G} = 2\gamma_s \quad (17)$$

where γ_s is the material's characteristic surface energy. At the moment of fracture, $\mathcal{G} = \mathcal{G}_c$, the critical energy release rate, which is a measure for fracture toughness.

\mathcal{G} is uniquely related to K in the following way

$$\mathcal{G} = \frac{K_I^2}{E'} \quad (18)$$

where $E' = E$ for plane stress, $E' = E/(1 - \nu^2)$ for plane strain, and ν is Poisson's ratio.

2.6 Elastic-Plastic Fracture Mechanics

This section introduces EPFM parameters J -integral and Crack Tip Opening Displacement. A short background and a procedure for obtaining the J -integral are presented, and the relationship between EPFM and LEFM parameters are also recognized.

2.6.1 J -integral

The J contour integral was introduced by Rice in 1968 [14], and has become an important fracture characterizing parameter for nonlinear materials. He applied deformation plasticity to crack analysis in a nonlinear material, and showed that the *nonlinear energy release rate* J could be written as a path-independent integral along an arbitrary path Γ around the crack tip:

$$J = \int_{\Gamma} \left(w \, dy - T_i \frac{\partial u_i}{\partial x} \, ds \right) \quad (19)$$

where w is the strain energy density, T_i is the tractions vector components, u_i is the components of the displacement vector and ds is the length increment along the contour Γ .

The definition for the energy release rate is the same for nonlinear materials as it is for linear elastic materials. This yields that in the case of a linear elastic material, $J = \mathcal{G}$, and

$$J = \frac{K_I^2}{E'} \quad (20)$$

Rice & Rosengren [15] and Hutchinson [16] also concluded that the J -integral could be used to characterize stress and strain near the crack tip in nonlinear materials, thus J is also valid as a stress intensity factor.

To this day, most of the experiments done on micro-sized cantilever beams have not considered the elastic-plastic J -integral in their research, and mostly focused on the linear elastic stress intensity factor K . However, Wurster et al. [13] did include J -calculations in their fracture toughness research. They used the old ASTM standard for fracture toughness to calculate J , as the new standard requires a comprehensive knowledge of the crack extension and this is difficult to obtain in physical experiments. In atomistic modeling, however, a detailed view of the crack extension is easily managed. According to the newer ASTM standard for measurement of fracture toughness [17], J is the sum of its elastic component J_{el} and its plastic component J_{pl} :

$$J = J_{el} + J_{pl} \quad (21)$$

The components are defined as

$$J = \frac{K^2(1 - \nu^2)}{E} + \frac{\eta A_{pl}}{w(h - a_0)} \quad (22)$$

where K is calculated from equations (8)-(15), ν is Poisson's ratio, η is a constant equal to 1.9 [17], and A_{pl} is the area under the load-displacement curve, as depicted in Figure 11. w is the specimen thickness, h is the specimen height and a_0 is the initial notch depth, all depicted in Figure 10.

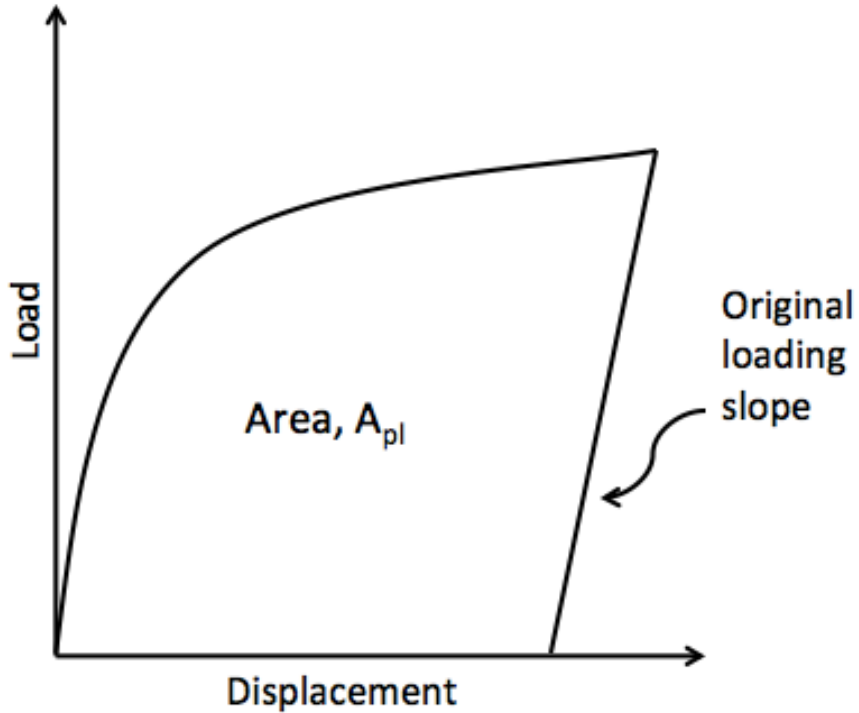


Figure 11: Depiction of the A_{pl} parameter used in equation (). The triangle created by the original loading slope is subtracted from the full area, as this is regarded elastic contribution and already contained in J_{el} .

By turning around equation (20), a new K_Q can be calculated based on the obtained value for J [13]:

$$K_{Q,J} = \sqrt{\frac{JE}{1 - \nu^2}} \quad (23)$$

where E is Young's modulus and ν is Poisson's ratio. J can, as K , be considered a parameter specific for the material in question, if fitting into the following validity criterion [13]:

$$w, (h - a_0) > \frac{25J_{Ic}}{\sigma_y} \quad (24)$$

where σ_y is the yield stress.

The most common single-specimen test method to obtain monitoring of the crack growth is to use the unloading compliance method. With this, the crack length is computed at regular intervals throughout the test procedure by partially unloading the specimen and measuring the compliance. As the crack grows, the specimen becomes more compliant, i.e. less stiff [8]. Wurster et al. [13] calculated J for every unloading step, and plotted J against crack growth Δa .

2.6.2 Crack Tip Opening Displacement

In 1961, Wells [18] proposed that the opening of the crack tip could be a useful measure in the decision of fracture toughness in elastic-plastic materials, a parameter today well known as the Crack Tip Opening Displacement (CTOD). There are two common definitions of CTOD: the 90° CTOD and the blunting CTOD, see Figure 12. The former is defined as the intersection of a 90-degree vertex of the crack flanges, whereas the latter is based on the displacement of the crack surfaces at the point of the original crack tip [8].

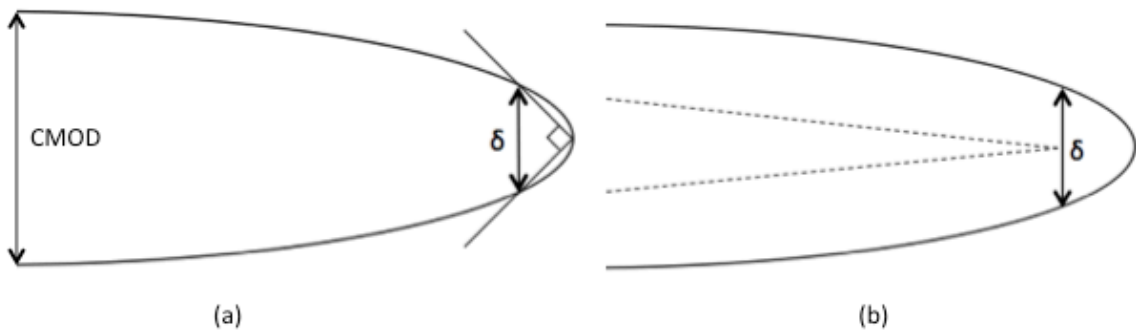


Figure 12: CTOD definitions; δ is CTOD. (a) 90° CTOD, also shows CMOD graphically, (b) blunting CTOD. The stippled line indicate original crack tip.

In small-scale yielding, the CTOD is related to the linear elastic parameters K_I and \mathcal{G} :

$$CTOD = \delta = \frac{K_I^2(1 - \nu^2)}{m\sigma_y E} = \frac{\mathcal{G}}{m\sigma_y} \quad (25)$$

where δ is CTOD, σ_y is the yield stress and m is a dimensionless constant that is approximately 1.0 for plane stress and 2.0 for plane strain conditions [8]. The small-scale relation $J = \mathcal{G}$ then yields

$$J = m\sigma_y\delta \quad (26)$$

In an atomistic model, the measuring of CTOD is easily done by choosing the atoms near the crack tip, and outputting the distance between them. This would be correlating to the blunting CTOD described in Figure 12.

A similar parameter also used in various toughness calculations is the Crack Mouth Opening Displacement (CMOD), which measures the opening at the top of the crack rather than the tip. CMOD is also depicted in Figure 12.

2.7 Atomistic Modeling of Fracture

Many reports have been made on atomistic simulations of fracture in BCC iron over the recent years. There are a number of different parameters one can take into consideration, such as crystallographic orientations, interatomic potentials, loading rate, temperature, etc. A collection of previous studies will be presented here. To the best of the author's knowledge, an atomistic model of a full cantilever beam has not been done, and the studies reviewed here is similar in crack geometry, i.e. through-thickness edge cracks. The results show that the brittle vs. ductile response of a crack under plane strain conditions to a large extent depends on the crystallographic direction of the crack and the available slip systems.

Some of the very first to present results from MD simulations were DeCelis et al. [19] in 1983, where a pair potential was used to obtain a fully brittle cleavage fracture for α -iron, consistent with the Griffith energy solution.

Gordon et al. [20] presented a thorough comparison of 4 different interatomic potentials, with 5 different orientations. This research showed very little deviation with respect to the different potential in the same orientation; only one orientation had different behavior with respect to the potentials, though the orientation in itself showed high significance for fracture behavior.

Machová and Beltz [21] simulated a (001)[110] crack with two different crack lengths, using a Finnis-Sinclair N-body potential. The longer crack experienced cleavage along the (001) crack plane, whereas the shorter crack displayed twinning in the "easy twinning" system $\{112\}\langle 111\rangle$, accompanied by slow, subcritical crack growth.

Hora et al. [22] compared a central (001)[010] crack with an (001)[110] edge crack, for temperatures 0 K and 300 K using a Finnis-Sinclair N-body potential. The central crack exhibited brittle crack growth on 0 K, but at 300 K displayed two different slip patterns. These patterns were found to be at 45° and 26.565° angles, on $\{101\}$ and $\{112\}$ planes, respectively. The edge crack showed, along with crack initiation, unstable stacking faults which would later turn into twinning in the $\langle 111\rangle\{112\}$ slip systems.

Vatne et al. [23] did simulations using the quasicontinuum (QC) method on similar models as the ones presented, with an EAM potential at 0 K. Four different crack orientations were explored in a thin specimen. For the (010)[101] and the $(1\bar{1}0)[001]$ crack, brittle propagation

in the crack plane was observed. The (010)[001] crack also displayed brittle crack propagation, but in a 45° angle from the crack front. In the (011)[011] crack there was dislocation emission on the {112}{111} slip system blunting the crack tip, and in turn no brittle crack propagation. These simulations were done in 2D, but was later extended by Vatne et al. [24] to full 3D simulations under loading modes I, II and III. Similar behavior was observed, implying that a 2D simulation will be sufficient for many simulation problems. The emission of full dislocation loops, however, is obviously not seen in 2D simulations and need 3D to be analyzed.

Ersland et al. [25] compared a through-thickness crack with an enclosed penny-shaped crack, the latter to explore the effect on a non-straight crack. This paper also compared the effect of full 3D simulations vs. quasi-3D. Both geometries were done with the crack plane located on three different crystallographic planes: the {100}, {110} and the {111} planes. The through-thickness crack had its crack front in two different directions for each crack plane. What was observed in the full 3D penny-shaped cracks was a small change in the crack shape, allowing for FCC formation, dislocation emission and twinning to happen, concluding that the material organizes itself so that the crack will favor blunting and grow as little as possible.

2.7.1 Brittle vs. Ductile Response

As stated in section 2.4, the crack tip response is basically a competition between atom bond breaking and dislocation emission, and which mechanism wins this competition is dependent on the ratio of theoretical shear strength to theoretical tensile strength, a criterion proposed by Kelly et al. [26] already in 1967. Rice & Thomson [27] took this into consideration and included the dislocation processes in their research, as plastic growth does not happen without the emission of dislocations.

In 1992, Rice [28] introduced a new parameter: the *unstable stacking energy* γ_{us} , defined as a material's resistance to dislocation nucleation. He found that the level of stress intensities needed to nucleate dislocations is proportional to $\sqrt{\gamma_{us}}$. γ_{us} is a parameter specific for its material, and is used to derive a new stress intensity factor K_d for dislocation emission, i.e. ductile crack growth, in contrast to K_c for cleavage which is based on the Griffith surface energy γ_s . Hence, in theory, if the applied stress intensity K_I exceeds K_c , the material will fail by cleavage, and if the applied stress exceeds K_d dislocations will emit and produce ductile growth [22]. K_c is defined by combining equations (17) and (18):

$$K_c = \sqrt{\frac{2\gamma_s E}{1 - \nu^2}} \quad (27)$$

and K_d is defined as

$$K_d = \sqrt{2\gamma_{us}\mu(1 + \nu)Y} \quad (28)$$

where μ is the shear modulus and Y is a geometric factor depending on the angle of dislocation emission (slip plane angle and direction of sliding) [9].

Both surface energies and unstable stacking energies are defined within the interatomic potentials used in atomistic simulations. The energies for relevant crystallographic planes for an EAM Mendeleev-II potential are listed in Table 2.

Ersland et al. [9, 25], while studying the crack tip response of an embedded penny-shaped crack, discovered that even though the energy obtained in the system was lower than the expected Griffith energy for cleavage, the initially round crack changed shape into a hexagonal shape, to easier allow for the crack to emit dislocations and blunt, instead of failing by cleavage.

Table 2: List of surface energies and unstable stacking energies for Fe in the Mendeleev-II potential [20].

Plane	γ_s [J/m ²]	γ_{us} [J/m ²]
{110}	1.65	0.663
{112}	1.91	0.770
{123}	1.87	0.755
{100}	1.79	
{111}	2.00	

Based on ranking of the surface energies, {110}, {100} and {123} planes will be the preferred cleavage planes, in that order.

NOTE: Due to time limitations, γ_s is not considered further in the results section, but is still mentioned here, as it is deemed an important field of research and an interesting aspect to look further into in upcoming work.

3 Modeling and Simulation

The work in this thesis was based on a model developed during the project work of autumn 2014 [2], with some necessary alterations done to account for different parameters, e.g. crystallographic orientations. This chapter will describe the model and the main aspects of how it's made, as well as the details for the simulations that have been performed. The model is a full-3D cantilever beam, connected to a support wall that is fixed to simulate the surrounding bulk material in a physical iron test specimen. The procedure is illustrated in Figure 1 in the Introduction chapter.

The bottom edge of the pentagonal cross section was rounded off to eliminate unwanted dislocations, see Figure 13. The model is set to be periodic in the y - and z -direction to simulate the support wall being indefinitely large, and non-periodic and shrink-wrapped in the x -direction, so the simulation box will move with moving atoms but no atoms will cross over boundaries. An example of the input script is found in Appendix C.

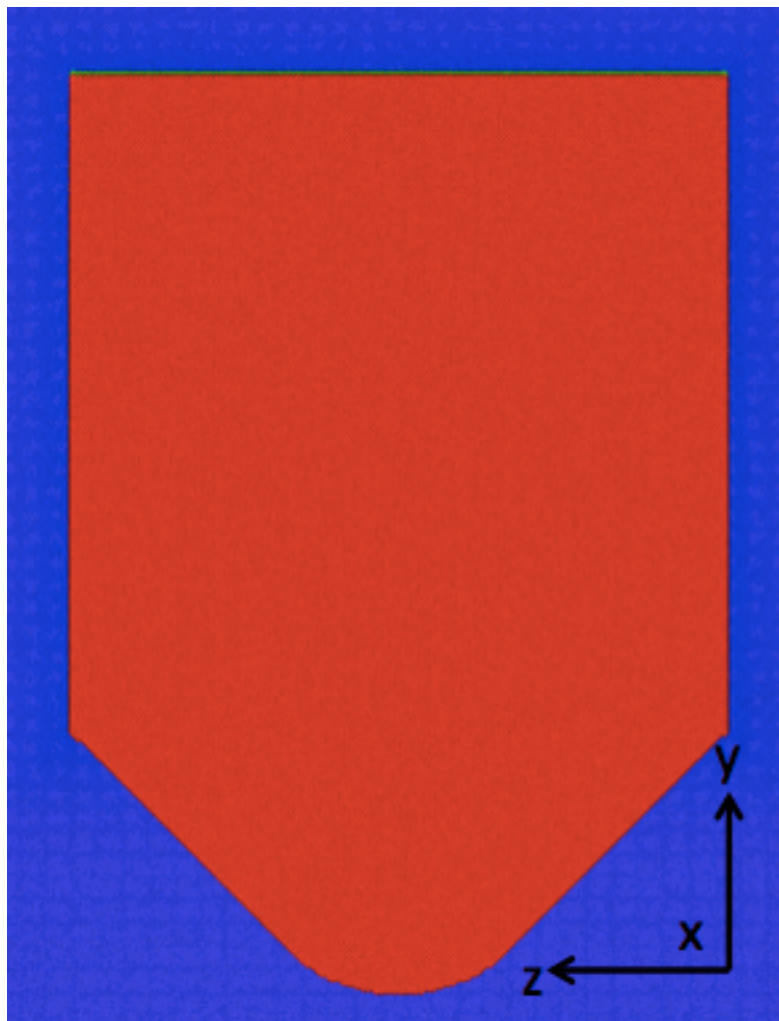


Figure 13: Cross section view of the beam displaying the rounded part at the bottom of the pentagonal shape. The x -direction is coming out of the paper plane.

Two different cross-sections were investigated, as described in section 2.5.1. The first cross-section is a square with an added triangle at the underside, previously depicted in Figure 9 in section 2.5.1. The second is a pentagon that is cut out of an initial square, also depicted in Figure 9. The second cross section was made on request for comparison purposes with specific, physical experiments performed concurrently in the Nanomechanical Lab at NTNU, whereas the main cantilevers with the first cross section aim to simulate micro-cantilever experiments in general.

The crack is atomistically sharp, and is simulated by assigning certain atoms into two groups on each side of the crack, and turning off the atomic interaction between them. To measure the CTOD/CMOD, atoms on each side of the crack were assigned to separate groups, and the distance between them calculated. These atoms lie on a line along the full beam width, and the distance between them are calculated from the mean x- and y-value.

The model was made so that the crack front was along the z-axis, the crack plane was the yz-plane, and thus the x-axis was perpendicular to the crack plane; see Figure 14. To examine the effect of crystallographic orientation, four different orientation systems were chosen for the crack plane and crack front; these are presented in Table 3. The crack plane and crack front direction are depicted with a reference unit cell for each orientation in Figure 15.

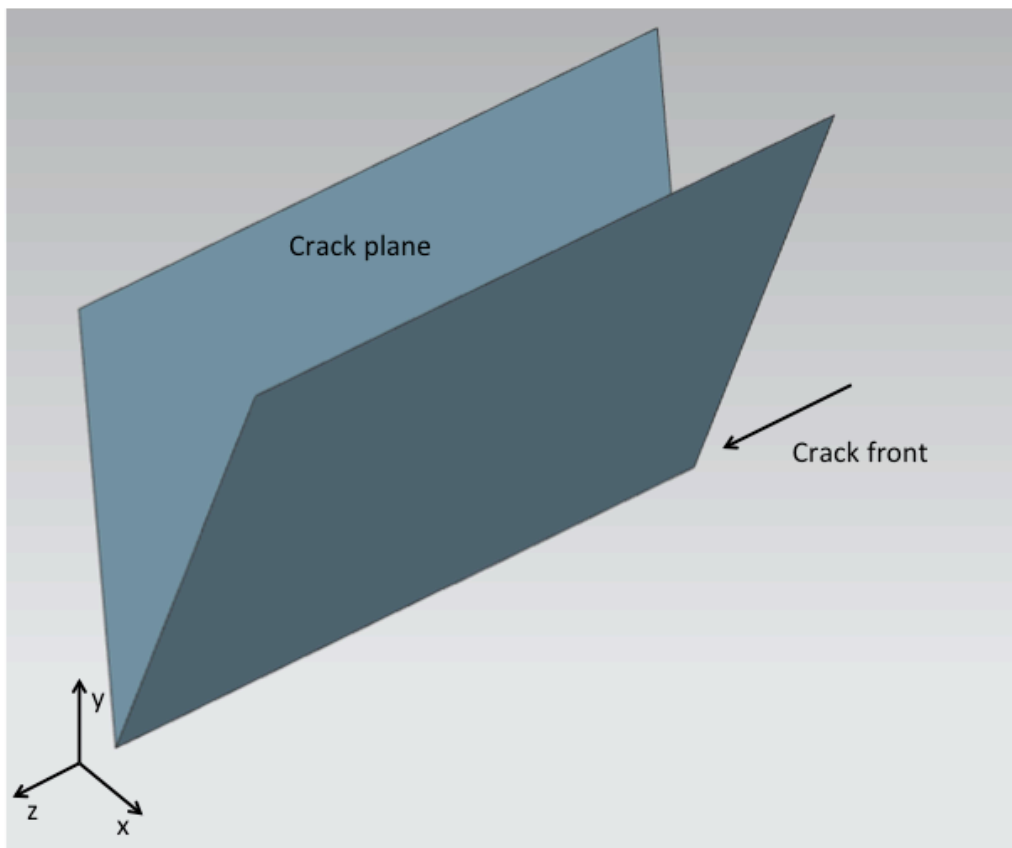


Figure 14: Description of crack plane and crack front.

Table 3: The four orientations chosen for the main simulations.

Orientation	Crack plane	Crack front
1	(100)	[001]
2	(110)	[001]
3	(10 $\bar{1}$)	[101]
4	(100)	[0 $\bar{1}$ 1]

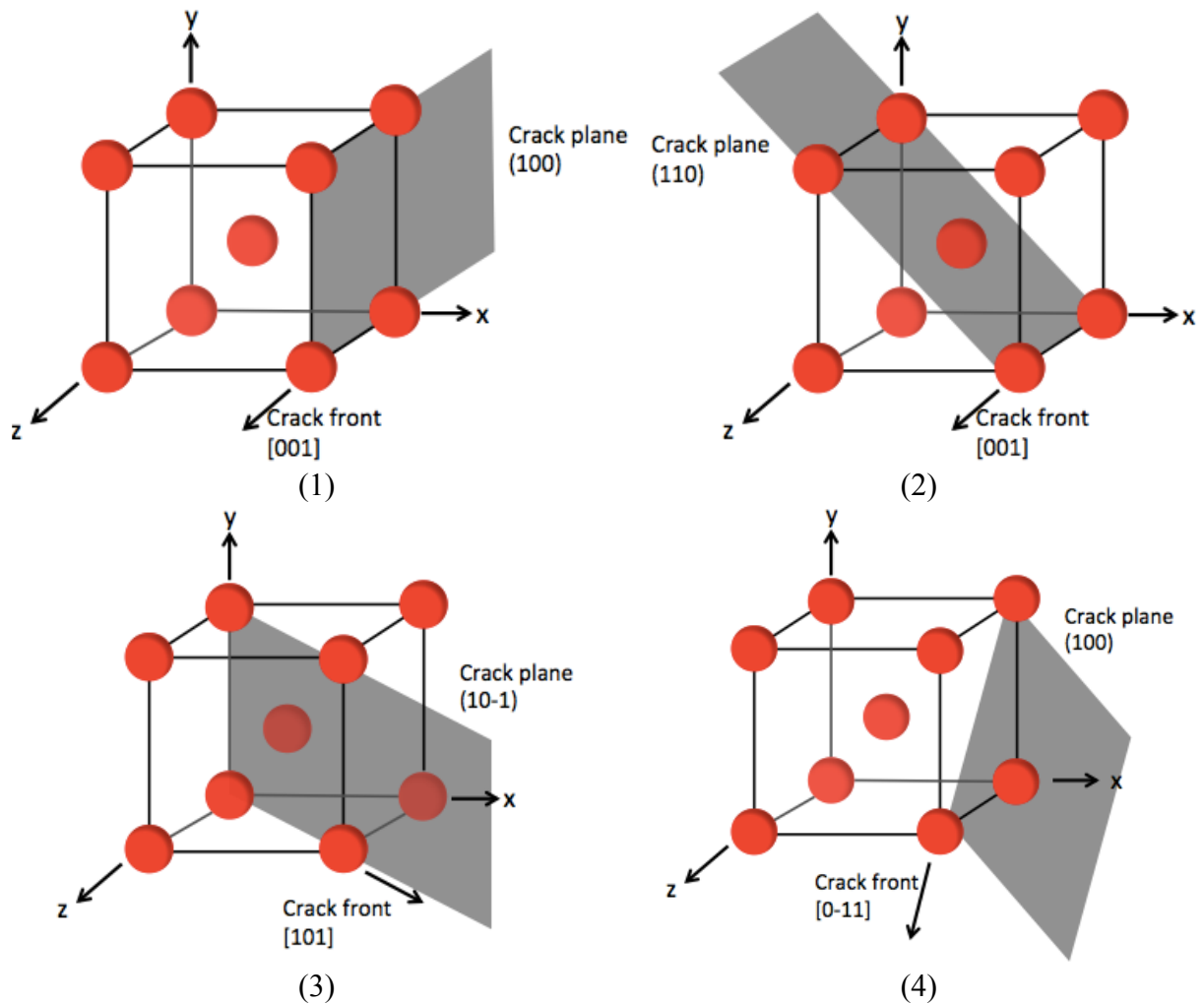


Figure 15: Schematic drawing of the crack plane and crack front orientation within a BCC crystal, denoted by orientation number from Table 3.

The indenter force deflecting the beam was simulated by applying a gradually increasing load to a group of atoms in a hemisphere close to the end of the beam. This gives a load-controlled experiment, where the load is connected to the time steps, and the end load is reached on the last time step. The end value for the load is chosen based on results from project work [2] and test simulations, as the load just after crack initiation for the corresponding cantilever. An overview of the simulations, number of time steps and total load is shown in Table 4. The load is applied to each atom in the given group. This value is multiplied with the number of atoms in the group, and also transformed into nN. Constant parameters for all simulations are listed in Table 5.

Table 4: An overview of the successful simulations.

Cantilever	Orientation	Time steps	h [Å]	End load per atom [eV/Å]	“Indenter” atoms	End load total [nN]
1	1	1 000 000	400	0.0035	181 636	1017.16
2	2	1 000 000	400	0.0035	182 201	1020.33
3	3	1 000 000	400	0.0035	181 688	1017.45
4	4	1 000 000	400	0.0035	182 201	1020.33
5	2	2 000 000	400	0.0035	182 201	1020.33
6	4	2 000 000	400	0.0035	182 201	1020.33
7	1	1 000 000	200	0.0013	181 636	236.13

Table 5: The constant parameters used in all simulations.

Constant parameters	
a/h	0.3
Temperature	300 K
Time step	0.0015 picoseconds
Relaxation	200 000 time steps
Material	BCC α -iron
Potential	EAM Mendeleev-II

For the remaining dimensions of the beam, see Figure 16. Here are also the x-, y- and z-axes represented in red arrows, placed in the origin of the beam.

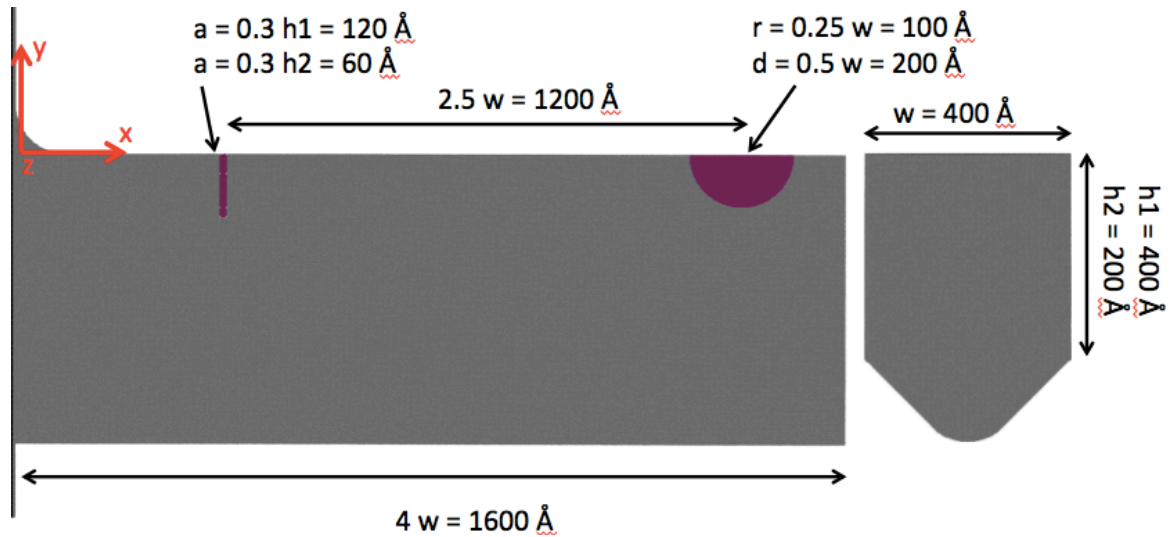


Figure 16: Dimensions of the cantilever beam, and the coordinate system placed in the origin. The z-axis is coming out of the paper plane. The hemisphere close to the end of the beam includes the atoms representing the indenter force.

Based on the findings described in section 2.7, some expected results, i.e. favored cleavage and slip systems, are presented in Table 6.

Table 6: Some preferred cleavage planes and slip systems for the orientations in question. The given angle is the one between the crack plane and the slip plane, normal to the crack front direction [9].

Orientation	(plane)[front direction]	Event	System/plane	Angle (°)
1	(100)[001]	Cleavage Cleavage	{100} {110}	0 ±45
2	(110)[001]	Cleavage	{110}	0
3	(10 $\bar{1}$)[101]	Cleavage Slip/twin Slip/twin	{110} {112}<111> {112}<111>	0 ±54.7 ±125.3
4	(100)[0 $\bar{1}$ 1]	Cleavage Slip/twin	{100} {112}<111>	0 ±35.3

Given that the simulations contain up to 30 million atoms, visualizing the full beam demands a very powerful computer. To ease the visualization process, different dump files were made with various amounts of atoms, as fewer atoms demand less of the computer power. The frequency of dumping out the different files is shown in Table 7. Alpha dump dumped all atoms that are not characterized as BCC, including the atoms on the whole beam surface. Beta dump excluded the surface atoms of the beam geometry, but kept the surface atoms in the notch.

Table 7: The frequency of the different dumping styles.

Dump	Every n time step
All atoms	100 000
2/3 length	50 000
Alpha	2 500
Beta	500

The program used for the simulations is the Large-scale Atomic/Molecular Massively Parallel Simulator (LAMMPS) [29], and the data are visualized in the Open Visualization Tool (OVITO) [30]. For more on how these programs work, please refer to project thesis [2]. The supercomputer Vilje, located on NTNU and run by NOTUR, was used to run the simulations. Vilje has 1404 nodes à 16 cores, giving a total of 22464 cores, and a 44 TB memory.

4 Results and Discussion

The results presented in this chapter are acquired from the simulations presented in Table 4 in the previous chapter. Cantilevers 1-4 are the main targets for the results section. They have the same run time and the same beam cross section, and only differ by crystallographic orientation. Cantilever 7 has a different cross section and the same orientation as cantilever 1, and is utilized in section 4.7 where it is compared to physical experiments. Cantilevers 5 and 6 are used in section 4.2 that focuses on different loading rates.

The structure of this chapter is thought to reflect chapter 2 in the best way possible. Firstly, the effect of crystallographic orientation is presented, focusing on cantilevers 1-4. Then the loading rate and crack geometry is considered, before a dislocation analysis is performed using the Crystal Analysis Tool. The LEFM and EPFM approaches are following, calculating stress intensity factor K , energy release rate \mathcal{G} and J -integral. The relationships between these parameters are utilized to obtain values for the yield stress σ_y . A comparison with physical experiments has been executed, and is presented in section 4.7.

4.1 Effect of Crystallographic Orientation

NOTE: For the graph shown in this section, the values have been truncated at $CTOD = 50 \text{ \AA}$. The CTOD is measured by calculating the distance between two lines of atoms on each side of the crack. The initial distance between these lines are subtracted prior to further processing of the results.

CTOD vs. displacement shows a significant displacement before there is any significant change in CTOD. This means that the beam is bending quite a bit before the crack starts to grow. What we see from Figure 17 is that cantilevers 2 and 3 and cantilevers 1 and 4, respectively, start propagating at the same displacement. Cantilever 3 does however get the most displacement, implying that the CTOD and crack growth doesn't influence overall deformation as much as the deflection of the beam. The opposite is observed for cantilever 4, for which the CTOD increases almost completely independent of the displacement on the graph after crack initiation.

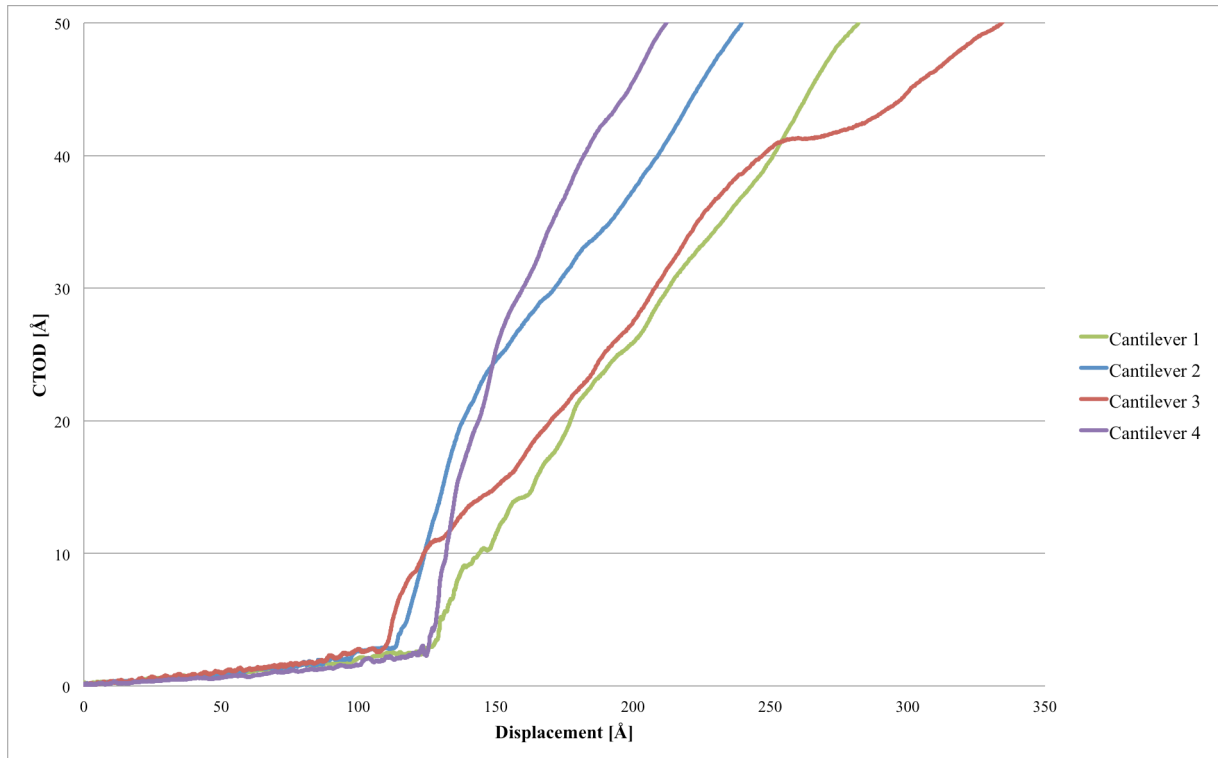


Figure 17: CTOD vs. displacement for the four different orientations, run over 1 million time steps.

In the elastic part of the simulation there is a development of non-BCC atoms near the crack tip. This is caused by the high stresses and strains pulling the crystal out of its desired cubic structure, and therefore causing LAMMPS to identify the atom as non-BCC. It is assumed that this is the plastic zone emerging on the crack front, and this will further be referred to as plasticity in the descriptions. The main results and findings of the four different cantilevers are presented on the next pages, including the main dislocation activity observed. A more detailed analysis of the dislocation activity is performed in section 4.4. The following figures include mid-beam ($z = 200 \text{ \AA}$) crack growth for all cantilevers, in addition to a depiction of the edge at the same time step ($z = 0$). For a full through-thickness growth depiction of cantilevers 1-4, see Appendix B.

Orientation 1, (100)[001]

Orientation 1 has the crack plane on (100), and the crack front along the [001] direction. Plasticity develops in an angle of about 45° from the crack tip. The first bonds break shortly before the crack starts to propagate, quickly followed by the first dislocation emission observed at $\text{CTOD} = 3.4 \text{ \AA}$. The crack propagates in a brittle manner, and stepwise. After some crack growth along the crack plane, the crack cleaves along the $(\bar{1}10)$ plane at an angle of 136.1° , depicted in Figure 18. At $\text{CTOD} = 19.8 \text{ \AA}$, FCC transformation in front of the angled cleavage is causing the crack to blunt. The crack growth happens only in the middle of the beam; the edges are blunted, also depicted in Figure 18. Twinning occurs at $\text{CTOD} = 15.3$

\AA in $z = 400 \text{ \AA}$, and shortly after also in $z = 0$. The twinning occurs on the expected $\{112\}$ plane. This cantilever shows similar crack growth behavior as observed in [23], [24] and [31] for the same orientation, and the cleavage plane is also expected according to Table 6. Hora et al. [22] observed slip at angles 45° and 26.565° when exploring the same orientation in a central crack on 300 K, inconsistent with what is observed here.

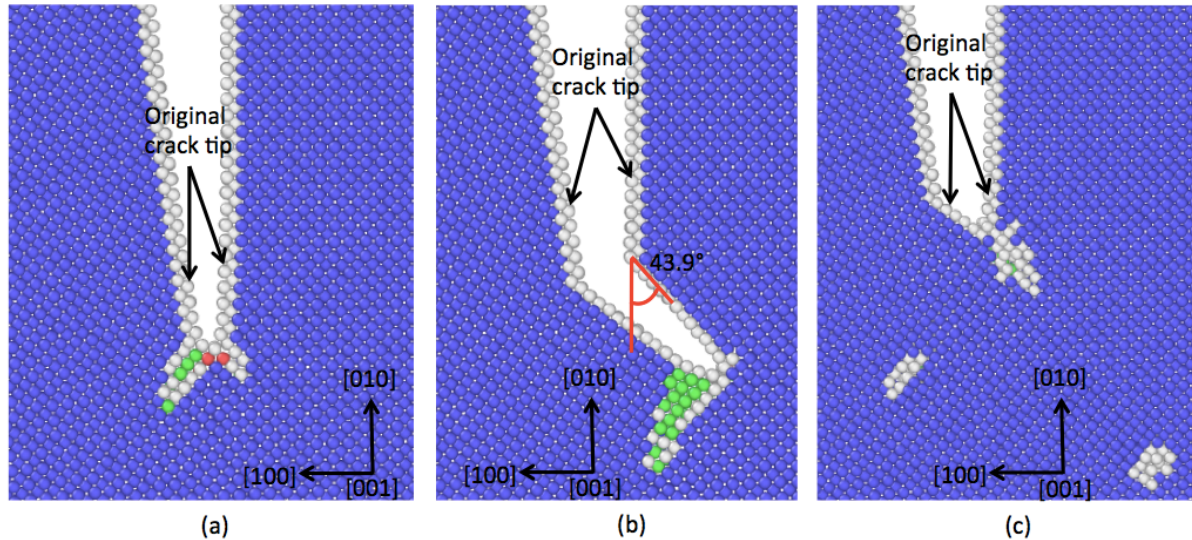


Figure 18: Crack growth for cantilever 1. (a) $z = 200 \text{ \AA}$ and $\text{CTOD} = 5.4 \text{ \AA}$, (b) $z = 200 \text{ \AA}$ and $\text{CTOD} = 10.4 \text{ \AA}$, (c) $z = 0$ and $\text{CTOD} = 10.4 \text{ \AA}$. Coloring is done by CNA, where blue is BCC, green is FCC, red is HCP and white is unidentified structure.

Orientation 2, $(110)[001]$

Orientation 2 has the crack plane on (110) , and the crack front along the $[001]$ direction. Plasticity develops almost perpendicular to the crack. Twinning starts in $z = 400 \text{ \AA}$ at $\text{CTOD} = 4 \text{ \AA}$, while a twinning plane develops in $z = 0$ when $\text{CTOD} = 7 \text{ \AA}$. As in cantilever 1, the twinning happens on $\{112\}$ planes. The crack grows visibly faster where the twinning is most developed, and therefore displays uneven growth before the twinning happens on both sides. The crack grows in a brittle manner in the middle, forming a triangle below the crack front. Dislocations emit from the twinning planes, blunting the crack below aforementioned triangle. It is apparent that the twinning and dislocation emission is relaxing the crack, causing it to blunt rather than propagate by cleavage. The edges of the crack are also blunted, which is the opposite of the behavior in the middle of the beam thickness, as portrayed in Figure 19.

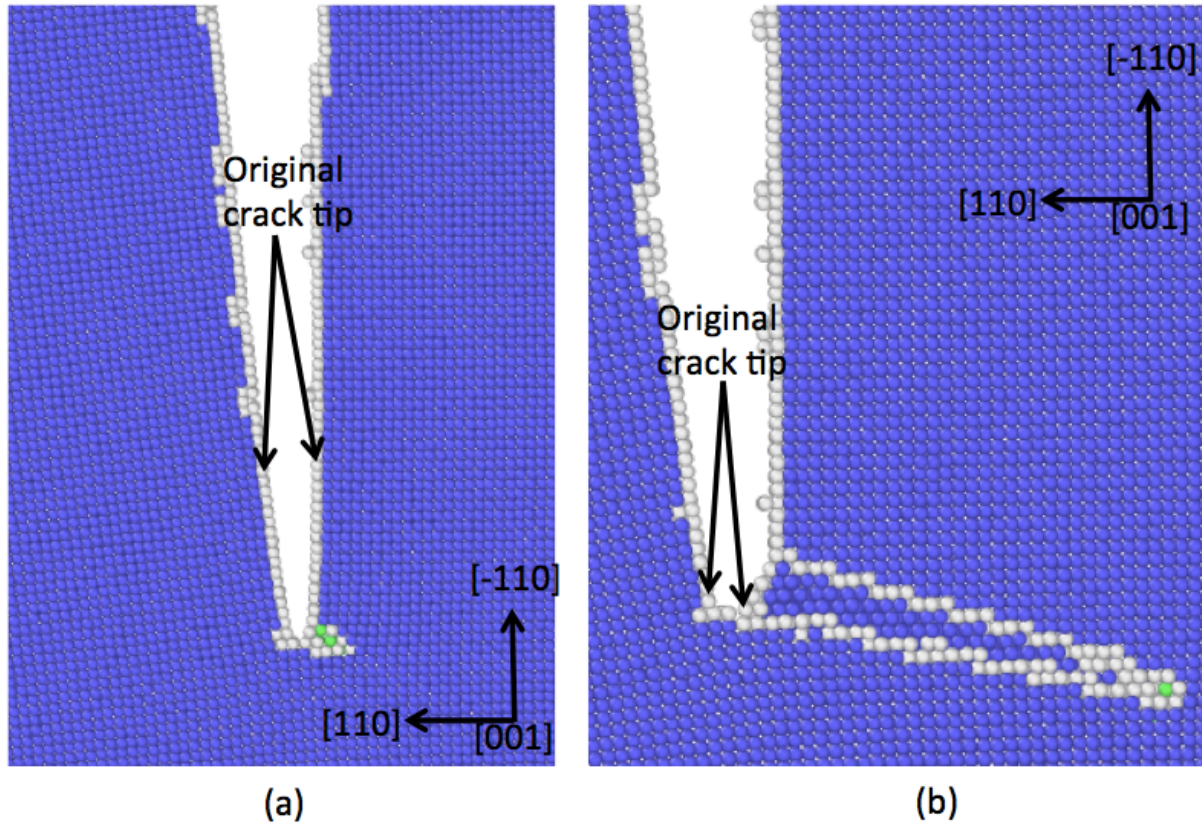


Figure 19: Crack growth for cantilever 2, at CTOD = 8.5 Å. (a) $z = 200 \text{ \AA}$, (b) $z = 0$. Coloring is done by CNA, where blue is BCC, green is FCC and white is unidentified structure. Note the twinning plane visible at the edge.

Orientation 3, $(10\bar{1})[101]$

Orientation 3 has the crack plane on $(10\bar{1})$, and the crack front along the $[101]$ direction. No plasticity of significance is developing before the crack tip starts to emit dislocations. First dislocation emits from $z = 0$ at CTOD = 3.1 Å, and loops towards the support wall, closely followed by another dislocation initiating in the middle of the beam and looping in the opposite x-direction. These dislocations release themselves completely from the crack tip and take place in rows at an angle of 52-58° on each side of the crack tip. From Table 6, slip is expected in an angle of 54.7°, so this shows good correlation. After several dislocations have travelled in this direction, they start to move upwards in positive y-direction, at an angle of 128.5° from the crack plane, still in good agreement with the expected result of 125.3° in Table 6. This orientation has the $\{112\}\{111\}$ slip system in the “anti-twinning” orientation [21]. This means slip is expected as dislocation emission rather than twinning, which is also what is observed here.

Orientation 3 exhibits less plastic development before dislocation emission and crack growth – and subsequently displays a significantly different behavior than the other orientations. The plasticity development happens due to high stress tearing the crystal out of their shape, making them characterized as non-BCC, and these high stresses are enough to initiate

propagation. In orientation 3 the stresses seem to be better distributed, as there is significantly less development of plasticity preceding the crack growth.

This orientation experiences quite heavy dislocation emission from the bottom of the beam. It was discovered late in the process that the rounding part had failed for this beam, and this might be the reason for this.

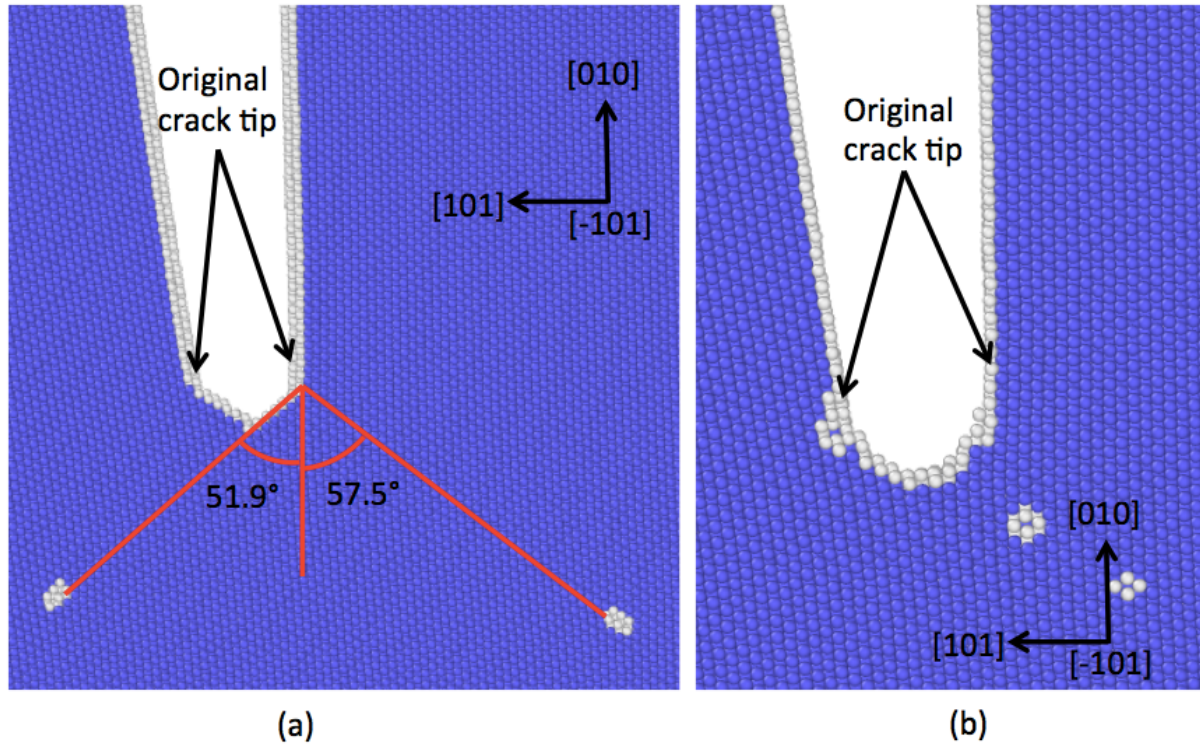


Figure 20: Crack growth for cantilever 3 at CTOD = 24.3 Å. (a) $z = 200$ Å, (b) $z = 0$. Coloring is done by CNA, where blue is BCC and white is unidentified structure.

Orientation 4, $(100)[0\bar{1}1]$

Orientation 4 has the crack plane on (100) , and the crack front along the $[0\bar{1}1]$ direction. Plasticity develops in no particular angle, just located below the crack front. The crack starts propagating in a brittle manner, slowly at first and then fast, along the (100) plane. The cleavage extends almost all the way to the edges. This one is by far the most brittle of the four orientations. At CTOD = 16.8 Å dislocations start to emit from the corners of the cleavage, looping towards the middle and hence blunting the crack in a triangular shape, though it is still brittle in the middle. This behavior is similar to that of orientation 2, only the initial cleavage fracture extended farther out on the edges and propagated longer before the triangular blunting. The edges are initially held together by a thin layer of atoms and a few, short dislocations on the edge of the cleavage fracture, but they are not blunted enough to withhold a fracture and this beam is the only one breaking all the way through. In Figure 21 (b), the edge is still being withheld by the small dislocations that are also visible as white atoms. However, a view of the full fracture is found in Appendix B.

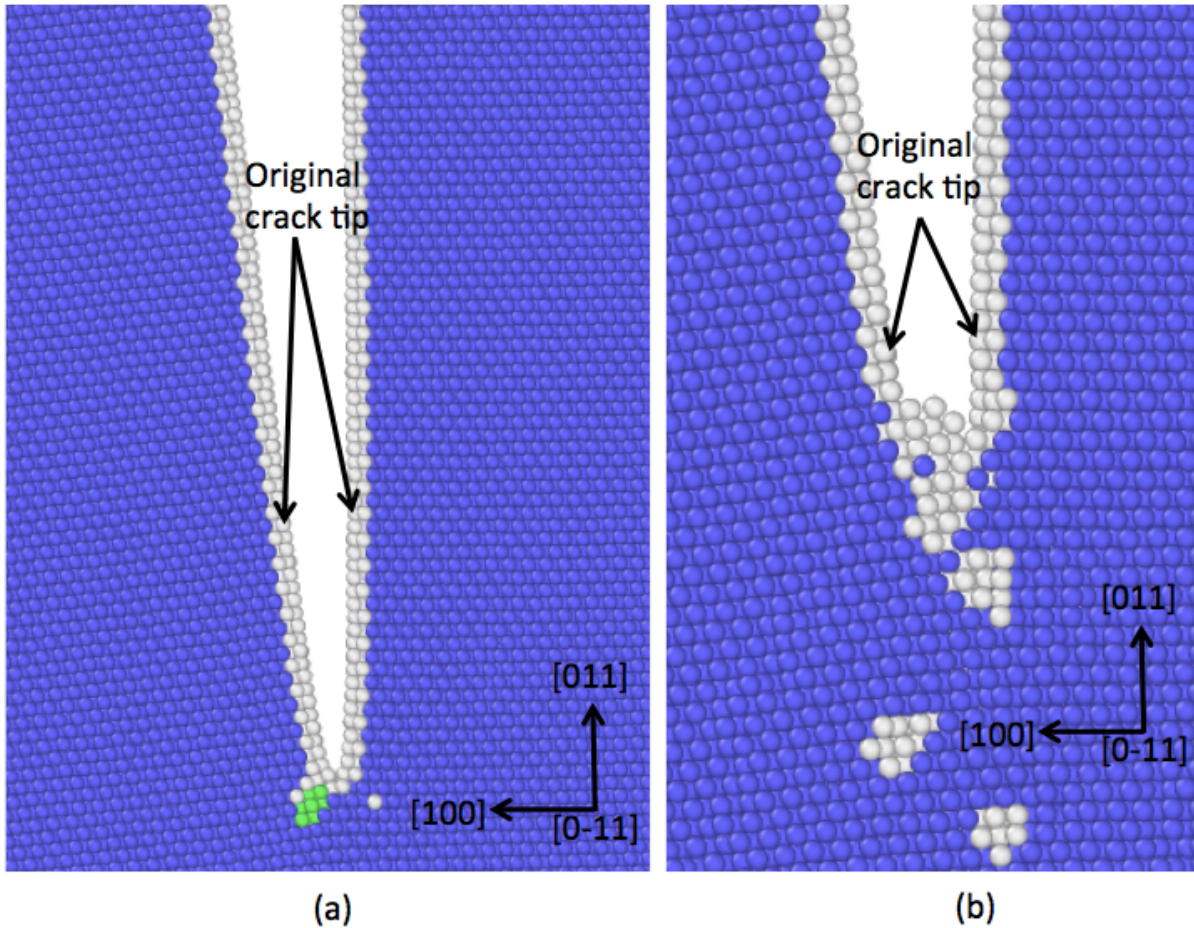


Figure 21: Crack growth for cantilever 4 at CTOD = 9.5 Å. (a) $z = 200$ Å, (b) $z = 0$. Coloring is done by CNA, where blue is BCC, green is FCC and white is unidentified structure. Note the small dislocations meeting the edge in (b).

The cantilevers tend to behave as expected, based on previous results. The behavior of the cantilevers are very similar to that observed in mode I loading by Vatne et al. [24] in 3D and also by Vatne et al. [23] in 2D. However, when reviewing the results obtained by Gordon et al. [20] for the same orientations and potential, only cantilever 4 exhibits the same behavior. They obtained ductile crack growth in orientation 2, and brittle in orientation 3, opposite of what is seen here. Orientation 4 has previously shown dependence on crack length: the longer crack propagated by cleavage, whereas shorter cracks developed twinning [21]. The crack length can therefore be explored further, to see if the same tendencies will be observed in the cantilever model, as the crack length researched here produced only cleavage.

All the cantilevers displaying cleavage fracture are doing so by propagating stepwise, like they are collecting enough energy to propagate further. The behavior is not reminiscent of unstable fracture, even though brittle fracture is usually known as unstable. Ersland et al. [25] observed that the penny-shaped cracks changed shape to easier emit dislocations and develop mechanical twins: the material was doing its best to avoid crack growth. This may also be the case for the cracks in the cantilever beams: even the very brittle will eventually emit dislocations or start twinning to relax the crack and slow down the growth.

In cantilevers 1 and 2, the edges are blunted regardless of the crack growing in the middle. This is due to the triaxiality of the beam, where the plane stress state on the edges withholds the growth, causing behavior reminiscent of *tunneling*. Tunneling was also observed in physical cantilevers in [13]. Cantilever 4 breaks all the way through, and cantilever 3 is as ductile in the middle as it is on the edges, implying that those two are not as affected by the triaxial state as cantilevers 1 and 2. This is also visible when looking at the cross sections for the beams at the end of the simulation, cantilevers 1 and 2 display considerable contraction at the crack edges, whereas cantilevers 3 and 4 look the same as pre-simulation, see Figure 22.

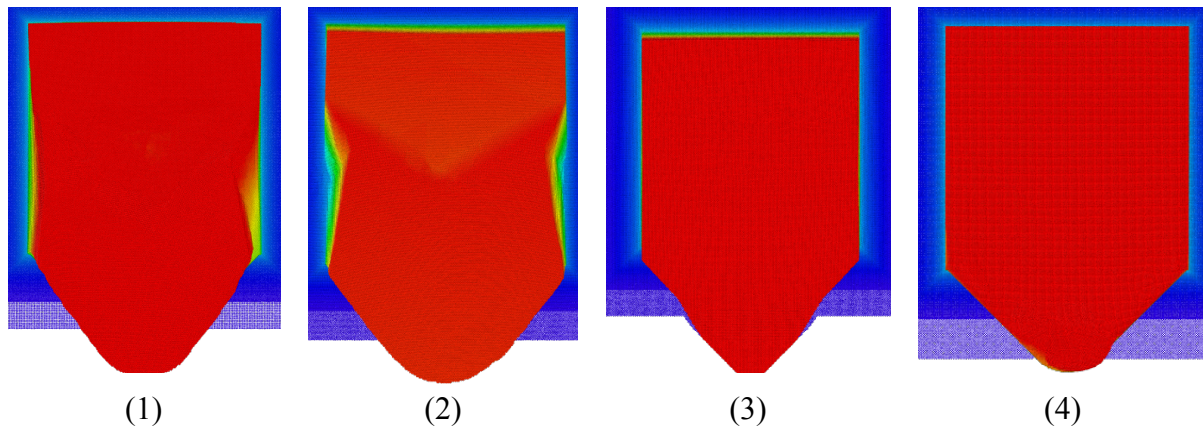


Figure 22: Last frame of all cantilevers, denoted by their respective number. The cut has been made at the crack for all cantilevers. Cantilevers 1 and 2 contract visibly, whereas 3 and 4 remain straight on the edges.

4.2 Effect of Loading Rate

As mentioned in chapter 3, orientations 2 & 4 were run with two different strain rates, over both 1 million and 2 million time steps, corresponding to cantilevers 2, 4, 5 and 6. The load vs. CTOD curves for the four simulations are shown in Figure 23. The 2 million jobs were aborted some time before the max load was reached, but as they had gone considerably longer than initiation they were deemed to be good for use anyway. This will, however, affect the plots, as the max load is lower for the simulations that did not completely finish.

The plots in Figure 23 show that the crack growth behavior is similar for the two orientations. It does seem however that cantilevers 5 and 6 show a more abrupt crack initiation, compared to cantilevers 2 and 4, which seem to initiate more smoothly. When the critical load is reached, cantilever 5 and 6 have been loaded for about twice as long as cantilevers 2 and 4, which might influence on the initiation behavior.

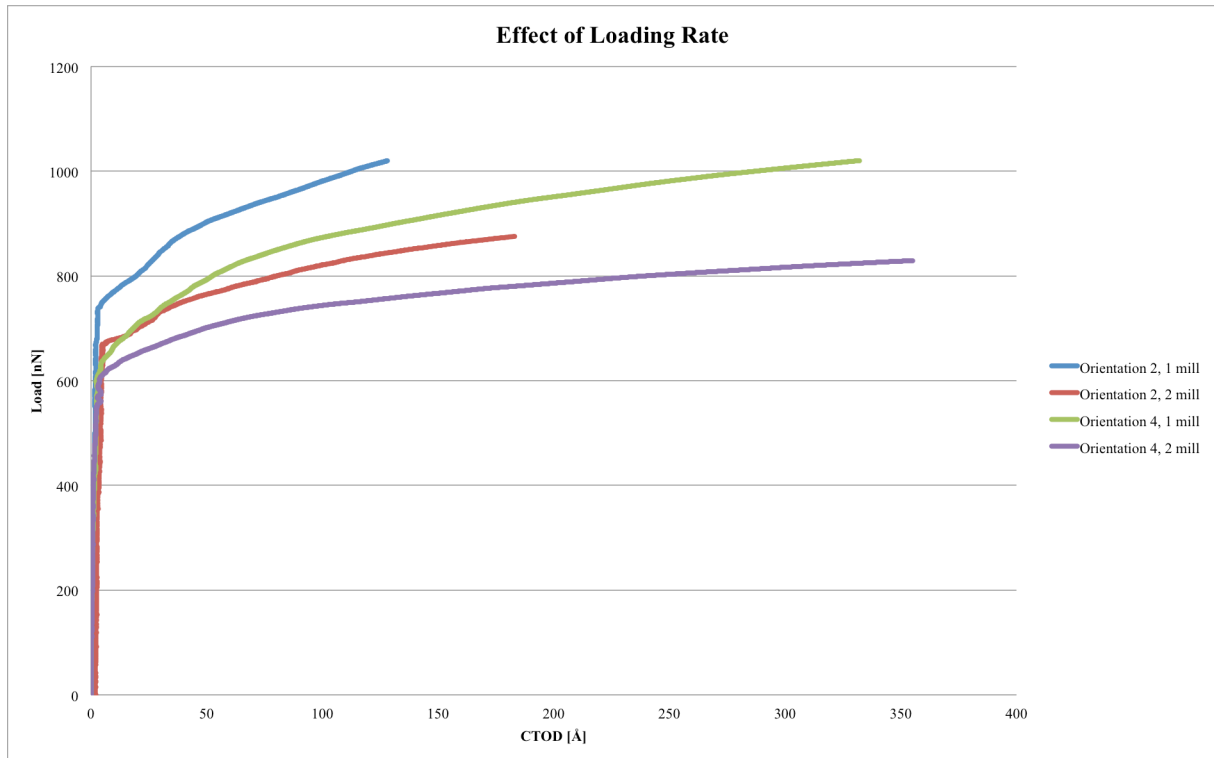


Figure 23: L-CTOD curves for orientations 2 and 4 over 1 and 2 million time steps.

Looking at the highest mutual load for all of them, 800 nN, it is evident that the cracks with the lowest loading rate have grown the most. This is also easy to spot when looking at maximum CTOD for the cantilevers, how the 2 million ones have grown more at their non-maximum load than the 1 million cantilevers have at their maximum.

It is already mentioned that the behavior seems to be similar for the two loading rates, and this is also confirmed when looking at the visualizations in OVITO. The beams exhibit pretty much identical behavior. The two loading rates are still both very high, and not highly different, when compared to physical experiments. This may explain the similarity in crack behavior. An even longer simulation would be interesting to see, but is also limited by computational power.

4.3 Effect of Crack Geometry

PhD candidate Jørn Skogsrud performed similar simulations concurrently with the work performed for this thesis. Instead of making an atomistically sharp crack, he created a crack with a certain width and a rounded crack front, closer to what a crack would be looking like when made by for instance Focused Ion Beam milling. The parameters for the cantilevers were otherwise the same. The two initial crack can be seen in Figure 24. The models with the rounded crack were run over 2 million time steps, twice as long as the sharp crack simulations. However, as the two different strain rates didn't have much influence on fracture behavior, as explained in the previous section, it is reasonable to assume that this comparison

still holds. Due to the different loading making the time steps un-relatable, a comparison was made based on similar displacement of the beams, the respective displacements listed in Table 8. The difference in the displacements is due to availability of dump files. It should be mentioned, that even though these comparisons are assumed to be reasonable, any differences might still be explained with the difference in loading rate and displacements.

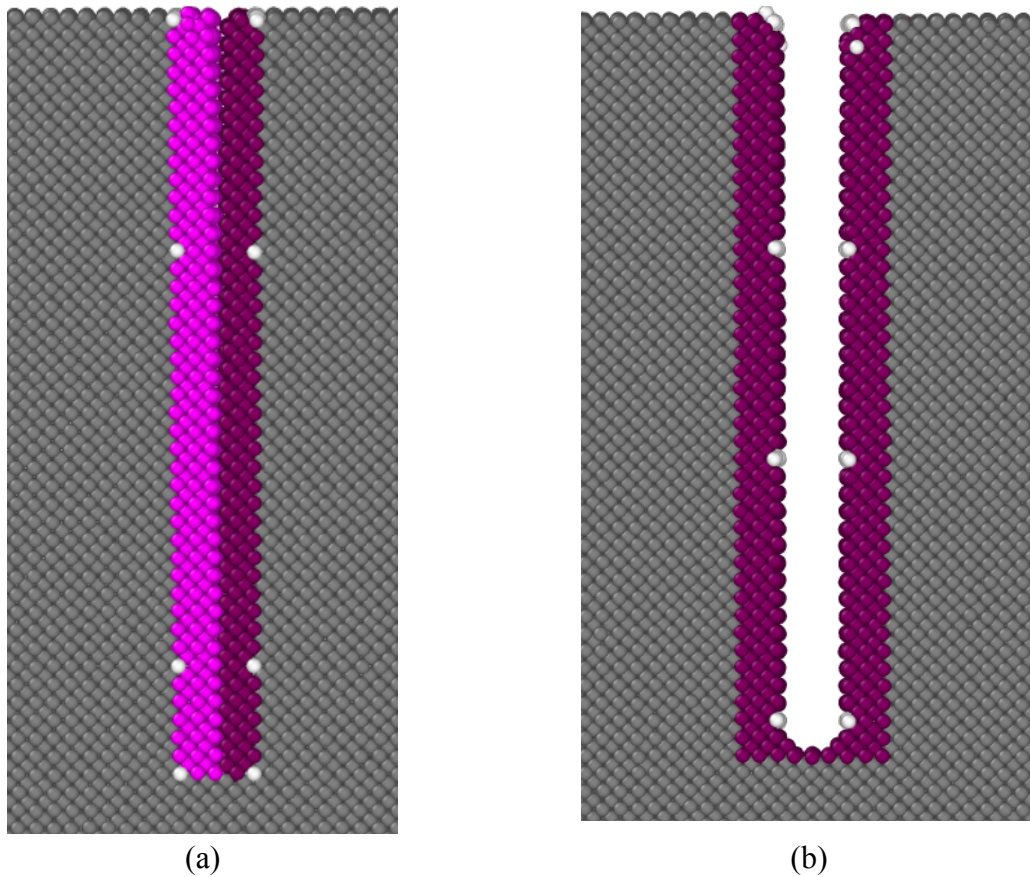


Figure 24: The two crack geometries before any deformation, (a) is atomistically sharp, (b) is rounded and with a certain distance (11-16 Å) between the walls.

Table 8: The different crack geometries and their respective displacements at the time of comparison.

Crack	Orientation	Crack Width [Å]	Displacement [Å]
Sharp	1	0	240
	2	0	193
	3	0	314
	4	0	245
Round	1	11	263
	2	16	188
	3	16	338
	4	11	226

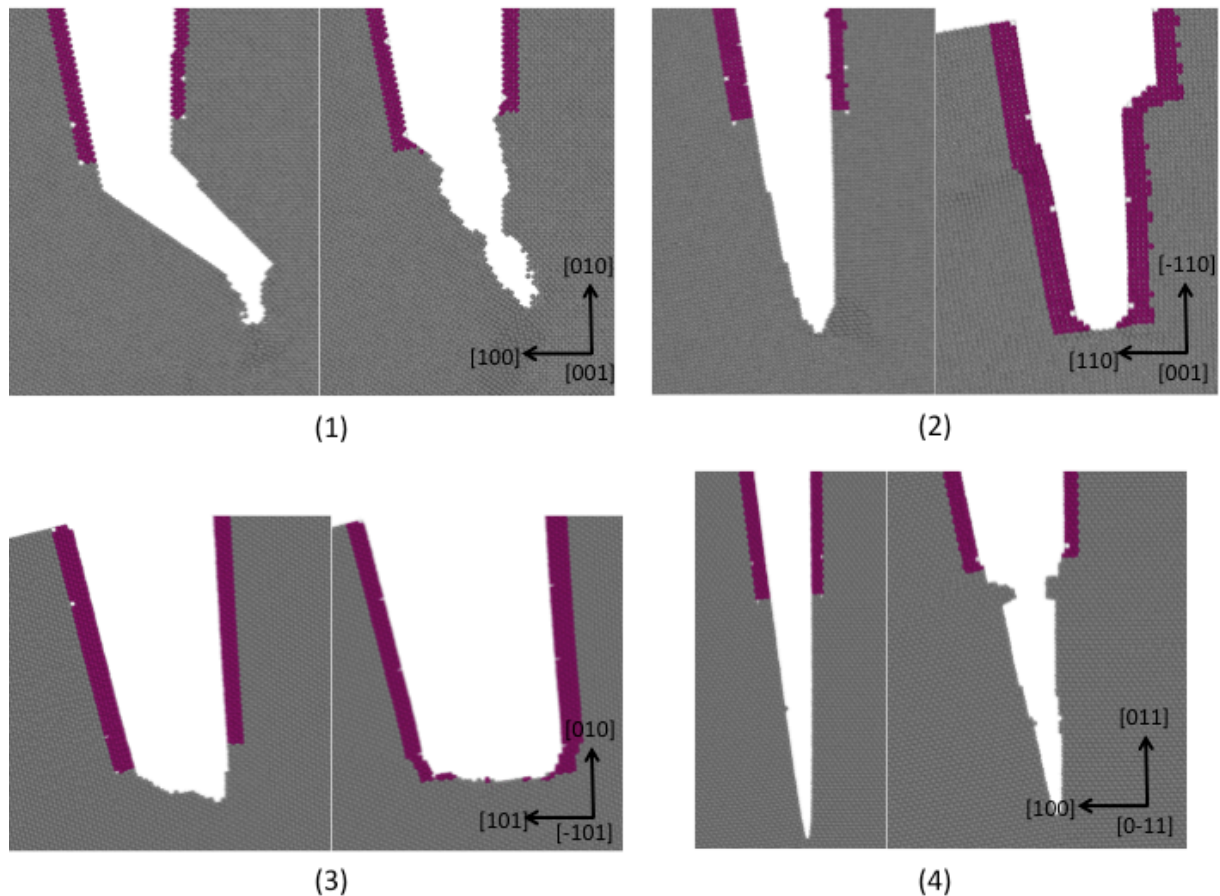


Figure 25: The four orientations, their respective number in parenthesis, with two different crack geometries, the sharp crack to the left and the blunted crack to the right.

As is presented in Figure 25, the two different crack types propagated in slightly different ways. This is probably due to the higher build-up of stresses in an atomistically sharp crack. The most similar are orientations 3 and 4. For the rounded crack, orientation 4 has some leftover “debris” from the original crack, but still shows very straight, brittle growth, if not as clean as the sharp crack produces. Orientation 3 is even more blunted, with less crack growth, with a rounded crack. The correlated displacements in orientation 2 are on different sides of the initiation point. However, the blunted version has a “kink” in the crack wall itself, something that is not seen for any of the other cantilevers. The kink develops due to dislocations trailing across the back of the crack wall. This naturally contributes to CMOD growth and overall increased displacement, and explains why the similar displacements for the two beams are on each side of the initiation point. Orientation 1 shows angled behavior for both beams, but the sharp crack produces much cleaner, more brittle growth than the blunted crack. In addition, the angle is sharper for the sharp crack cantilever. The crack geometry definitely affects the crack growth, which is expected due to the different distribution of stress. However, the general behavior of the cantilever is not very different between the two crack types.

4.4 Dislocation Analysis

A dislocation analysis was made for cantilevers 1-4, using the Crystal Analysis Tool (CAT). CAT reads a full dump file, not an alpha or beta file, and the first available dump file after crack initiation was chosen for the dislocation analysis. This section presents the CAT analysis of cantilevers 1-4, shown alongside the same time step in the beta dump file. The beta file is either colored by atom position or potential energy, based on which color-coding best described the dislocation. The directions of the x-, y- and z-axes are given for each cantilever. Two CAT files was made for cantilever 4, to account for both the small dislocations accompanying the crack growth, and the dislocation loops that emit later in the simulation. CAT returns all detected dislocations in a file that is visualized in OVITO. Dislocations with Burgers vector $\frac{1}{2}\langle 111 \rangle$ are shown in green, and the dislocations with Burgers vector $\langle 100 \rangle$ are shown in purple.

Cantilever 1

$$xyz = [100][010][001]$$

The first dislocation in cantilever 1 takes place before any significant crack propagation has started. The initial dislocations emit from the crack edges, like the one depicted in Figure 26. Probably the most interesting feature in the dislocation activity in cantilever 1 is the combination of dislocations, creating significant $\langle 100 \rangle$ Burgers vectors.

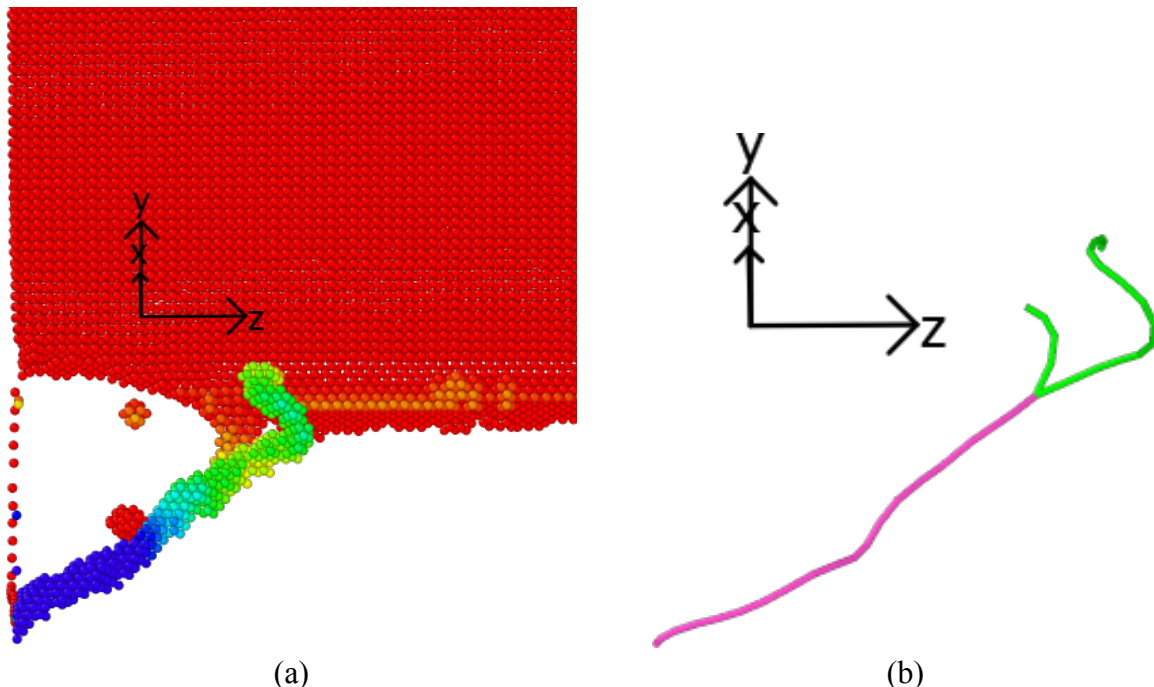


Figure 26: Dislocation development for cantilever 1 at CTOD = 5.4 Å. (a) shows the dislocation, colored by X-position, blue being closest and red farthest away. (b) shows the dislocation extracted, from the same position.

Cantilever 2

$$xyz = [110][\bar{1}10][001]$$

For cantilever 2, both dislocations and twinning are happening concurrently with crack initiation. The long dislocation in Figure 27, colored mostly in blue, emits from $z = 0$ (left side in figure), before any twinning has occurred. In $z = 400 \text{ \AA}$ (right side in Figure 27) twinning develops first, and the second dislocation emits from the bottom of the twinning plane. After substantial crack growth, both twinning planes emit dislocations regularly. Figure 27 also shows the uneven crack growth mentioned in section 4.1, the crack has clearly grown more underneath the most developed twinning plane.

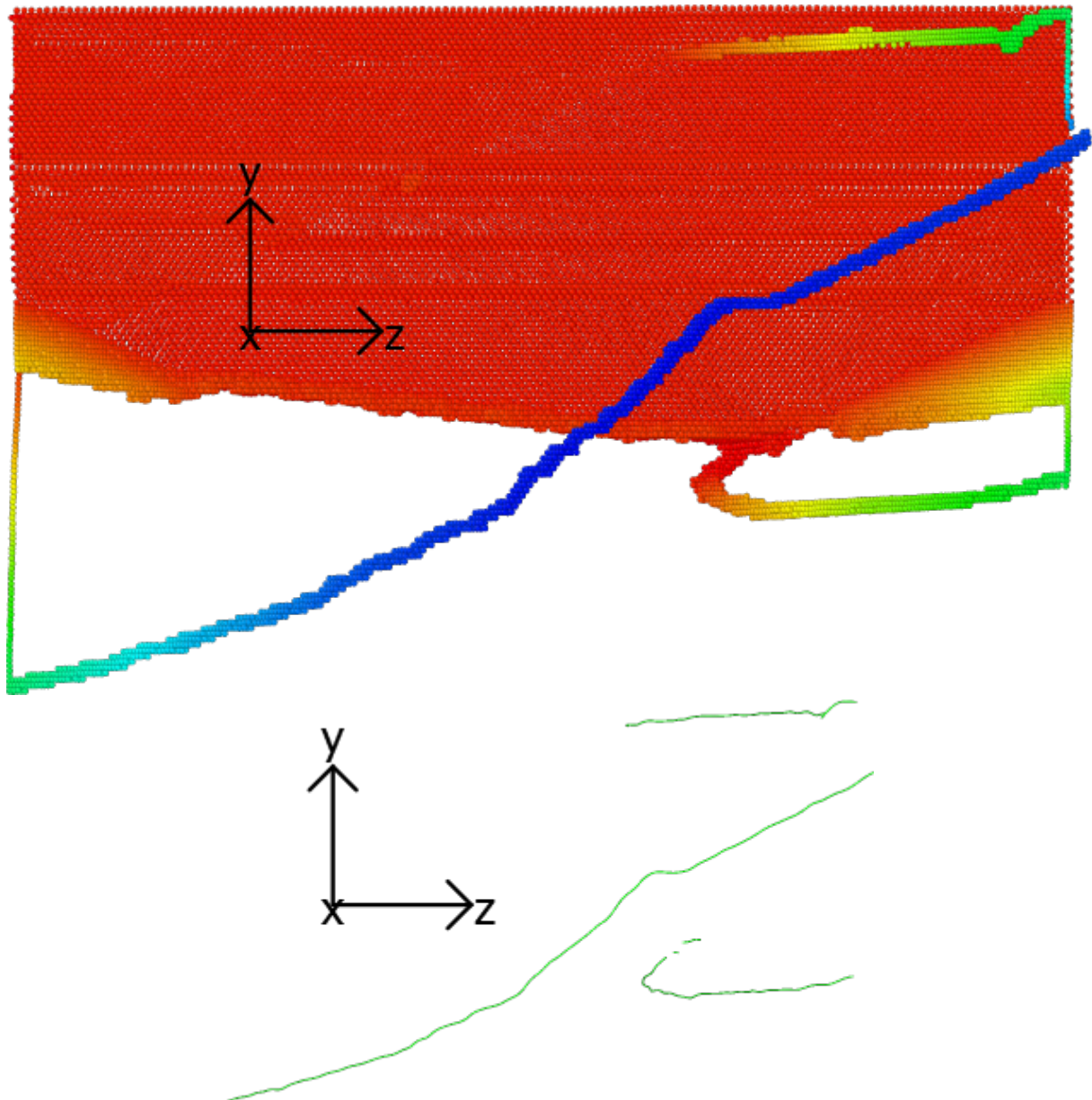


Figure 27: Dislocation development in cantilever 2 at $CTOD = 8.5 \text{ \AA}$. Top picture is colored by X-position, with blue being closest and red farthest away. The z-axis is aligned with original crack front. Bottom picture is the extracted dislocation from CAT.

Cantilever 3

$$xyz = [101][010][\bar{1}01]$$

Cantilever 3 has perhaps the most regular dislocation pattern of all the cantilevers. They emit from the crack tip, release themselves completely and follow the $\{112\}\langle 111\rangle$ slip planes at angles of $52\text{-}58^\circ$, as edge dislocations on each side of the crack tip. They go out on both sides of the tip, and moving downwards in a negative y-direction at first, see Figure 28. Late in the simulation, at $\text{CTOD} = 38.9 \text{ \AA}$, a new slip plane is activated, and the dislocations start moving in the positive y-direction in an angle of 128.5° with respect to the crack plane.

As mentioned in section 4.1, the rounding part at the bottom of the pentagonal cross section beam did not happen for this cantilever. Many dislocations emit from the corner of the beam and the support wall, and the lack of rounding is thought to abet this behavior. These locations portray the same type of behavior, lying organized in rows, but it is quite easy to detect which dislocations are coming from the tip or not. The dislocations detected from the bottom corner of the beam are partly cut out of the picture in Figure 29, but have been kept in Figure 28 to illustrate.

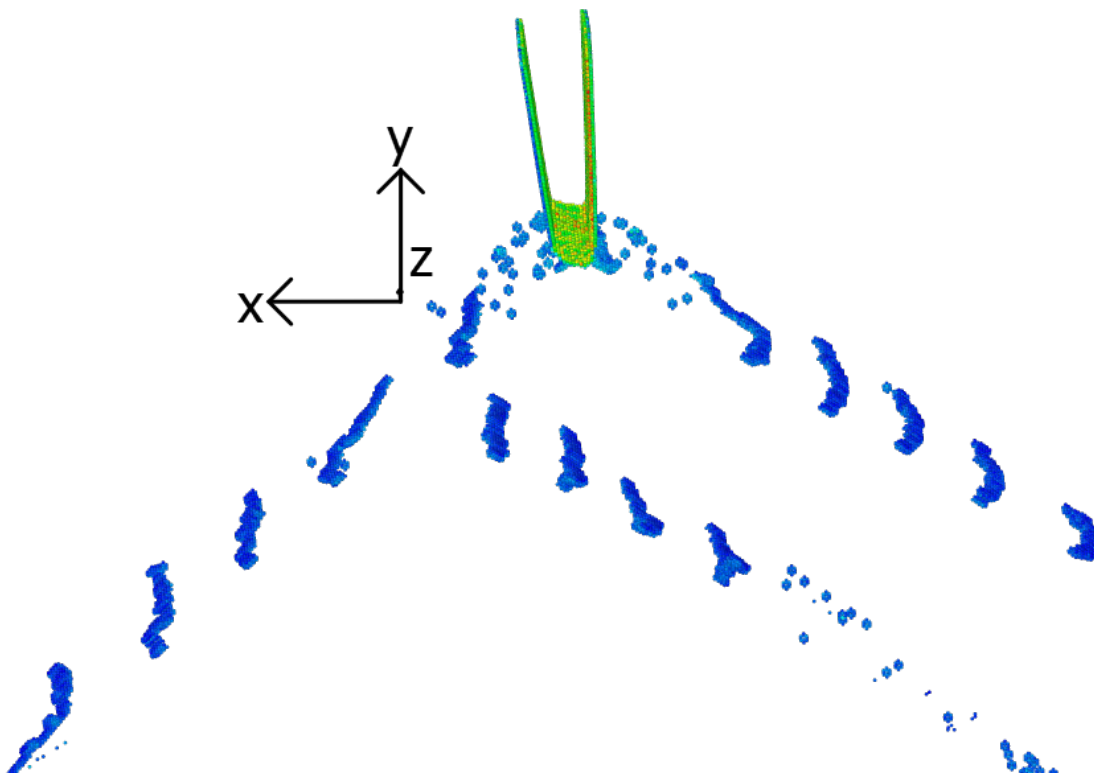


Figure 28: Visualization of the activated slip planes in cantilever 3. Note the separate slip plane occurring from the bottom of the unrounded beam geometry. The support wall is on the right-hand side in this figure.

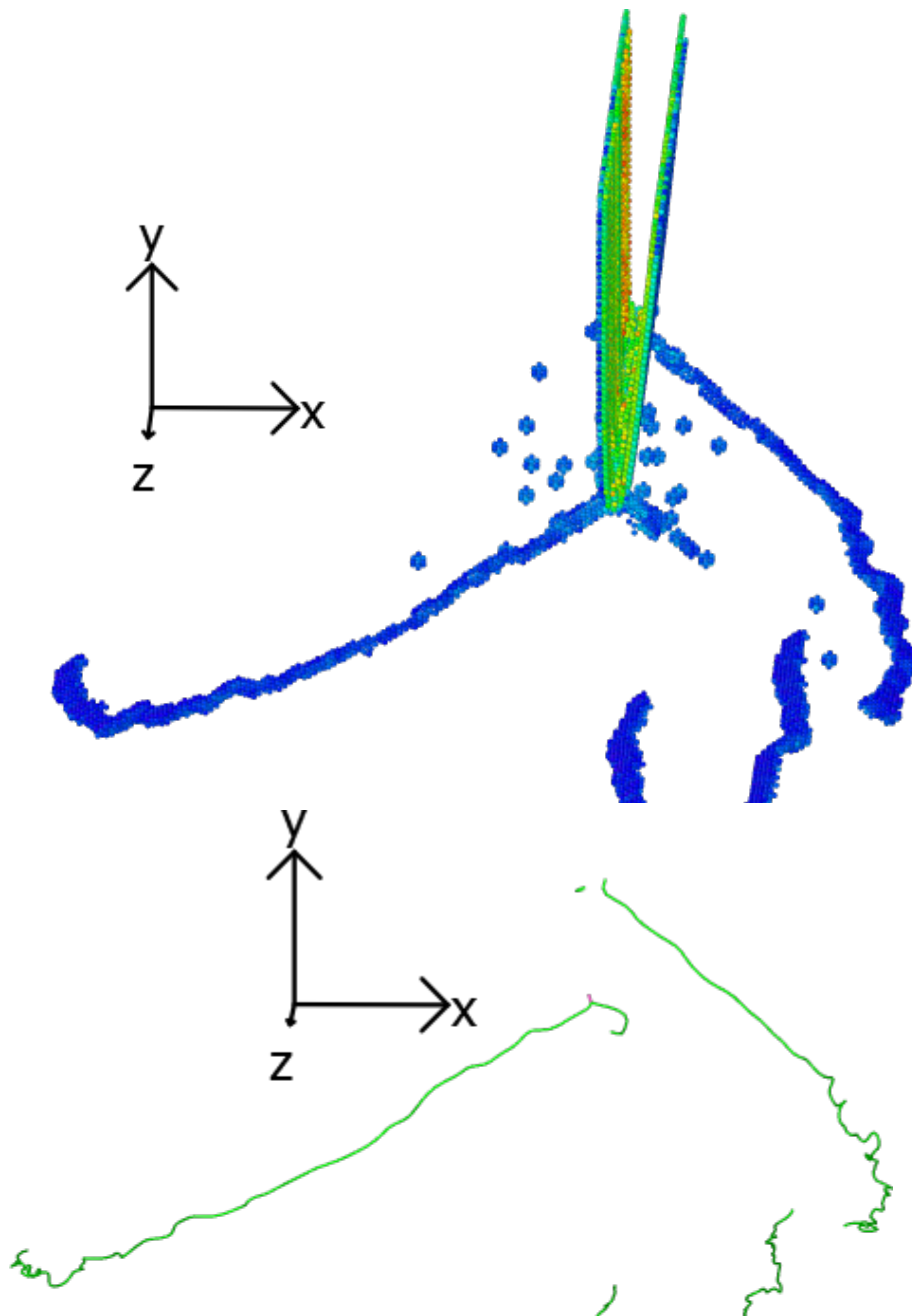


Figure 29: Dislocation development for cantilever 3 at $CTOD = 7.5 \text{ \AA}$. Top picture is colored by potential energy; bottom picture shows the extracted dislocations. The bottom two dislocations that have been partly cut out of the picture come from the corner of the beam and support wall and are deemed unimportant for the crack growth.

Cantilever 4

$$xyz = [100][011][0\bar{1}1]$$

Cantilever 4 has the least development of dislocations. There are small dislocations towards the edges of the beam, as is visible in Figure 30. These dislocations cross each other, and some even combine into a $\langle 100 \rangle$ Burgers vector dislocation, see Figure 31. After substantial crack growth, the dislocations emit as full loops; they relax the crack and slow down the growth. These loops can be seen in Figure 32. These dislocations emit very similarly on each side, and in general this cantilever shows very even, symmetric behavior. This symmetry is also clear for the cleavage propagation and the small dislocations shown in Figure 30.

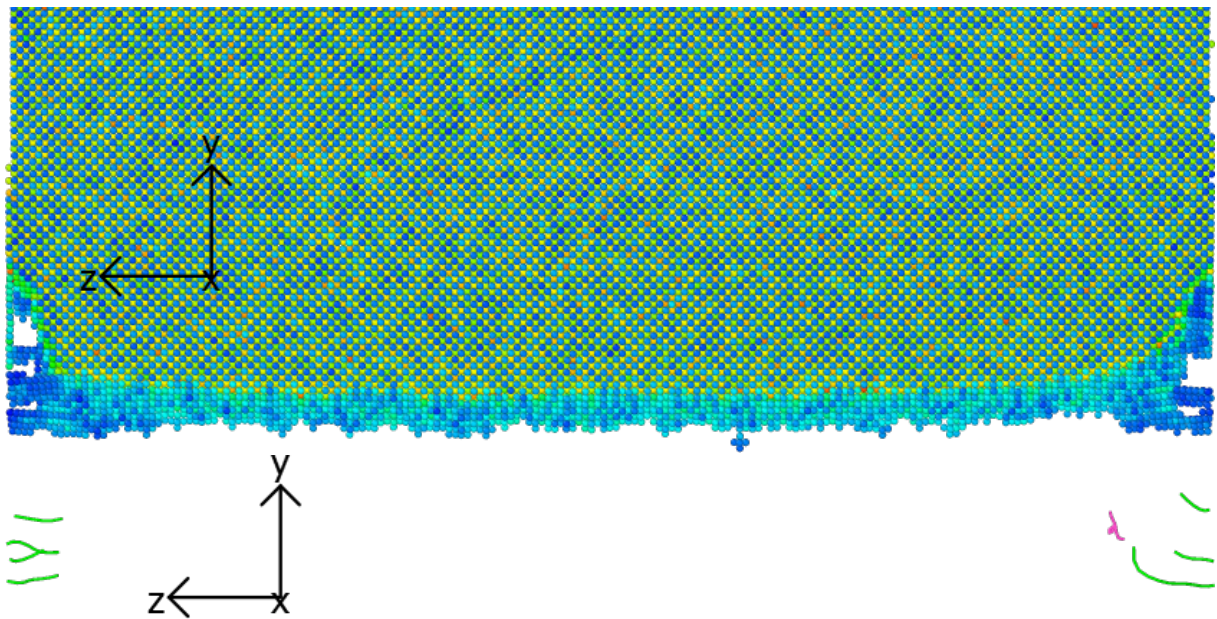


Figure 30: Dislocation development for cantilever 4 at CTOD = 9.5 Å, viewed from the end of the beam. Top picture is colored by potential energy.

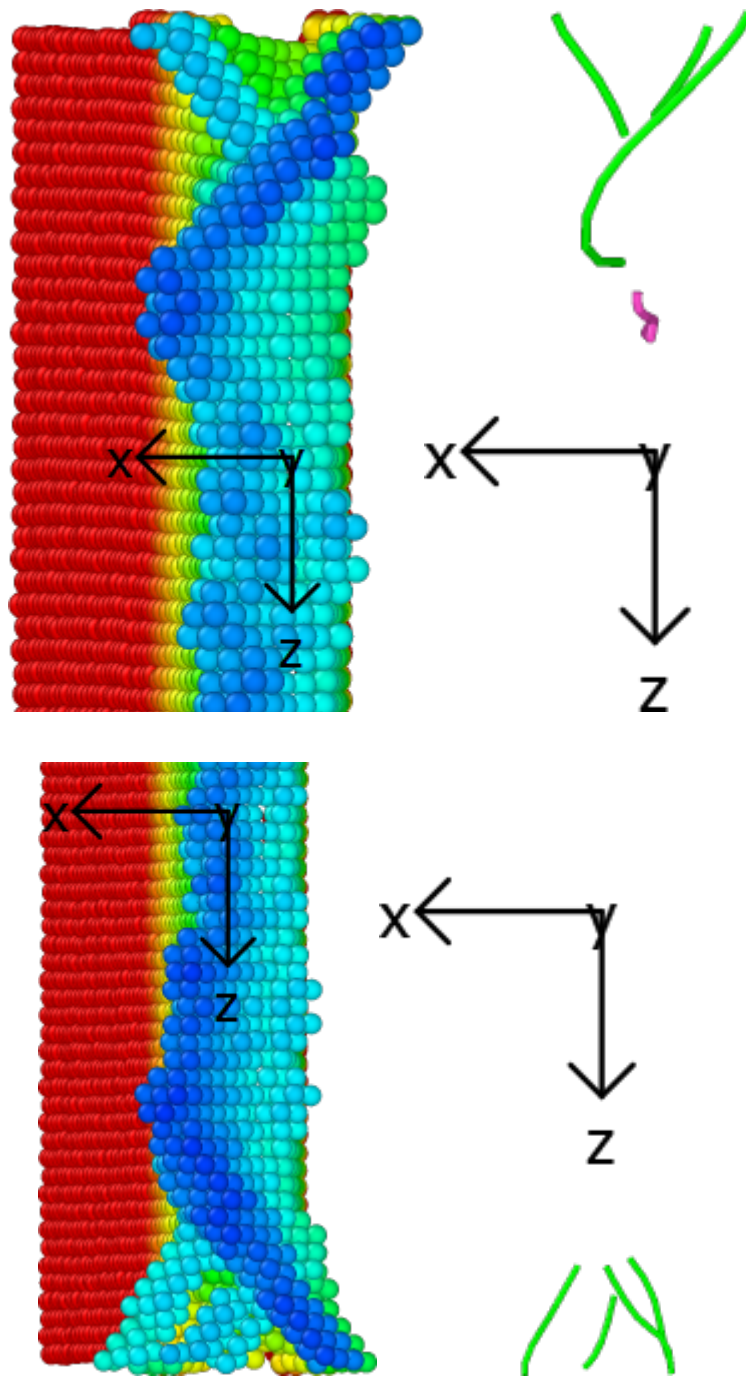


Figure 31: Dislocation development for cantilever 4 at $CTOD = 9.5 \text{ \AA}$, viewed from below the crack. Left pictures are colored by Y-position.

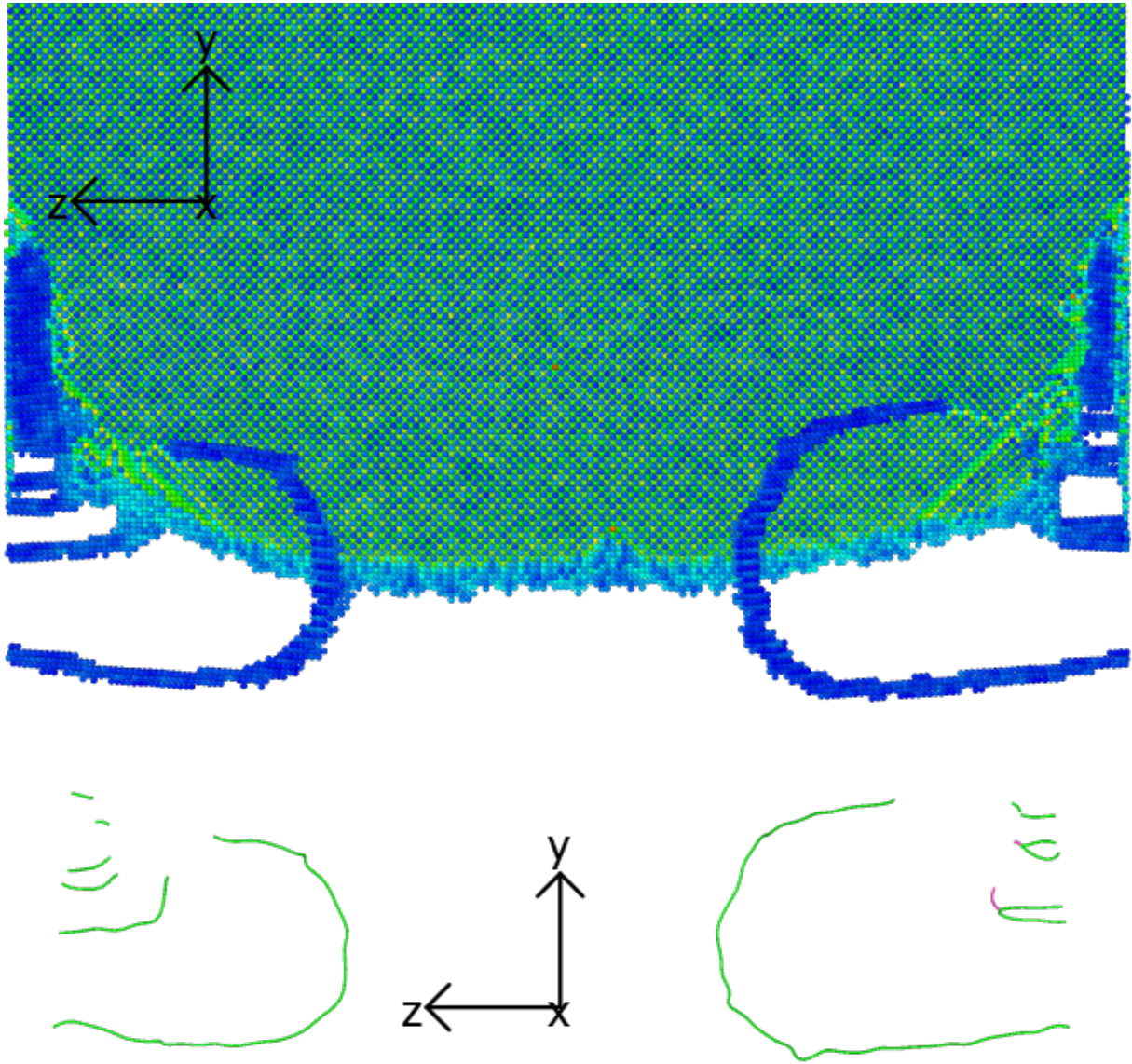


Figure 32: Dislocation development for cantilever 4 at CTOD = 21.9 Å. Top picture is colored by potential energy, and the z-axis is aligned with original crack front. Bottom picture shows the extracted dislocations from the CAT.

The beams emit mostly $\frac{1}{2}\langle 111 \rangle$ dislocations, and very different dislocation behavior between the orientations. The $\langle 100 \rangle$ dislocations come from two dislocations that merge. This is explained in section 2.3.1, and shown in Figure 33. The dislocations are generally of mixed character, though on some of the dislocations it is possible to spot screw and edge dislocation behavior, at emission point and at the beam edge, respectively. One example of this is depicted in Figure 34, for cantilever 3.

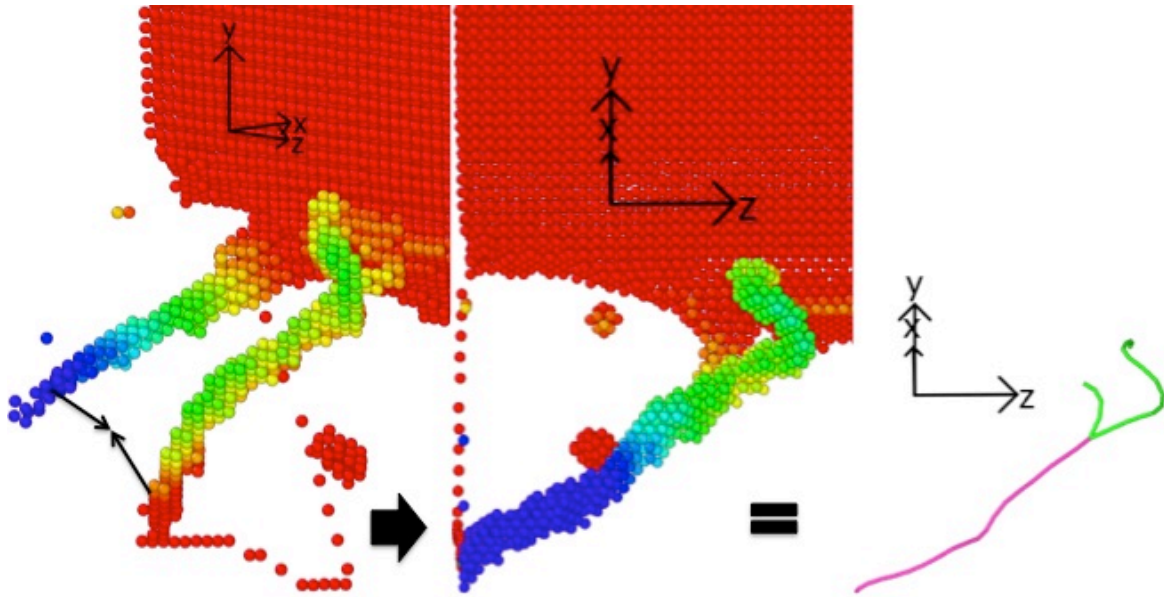


Figure 33: Development of a dislocation with $\langle 100 \rangle$ Burgers vector, when two dislocations merge into one.

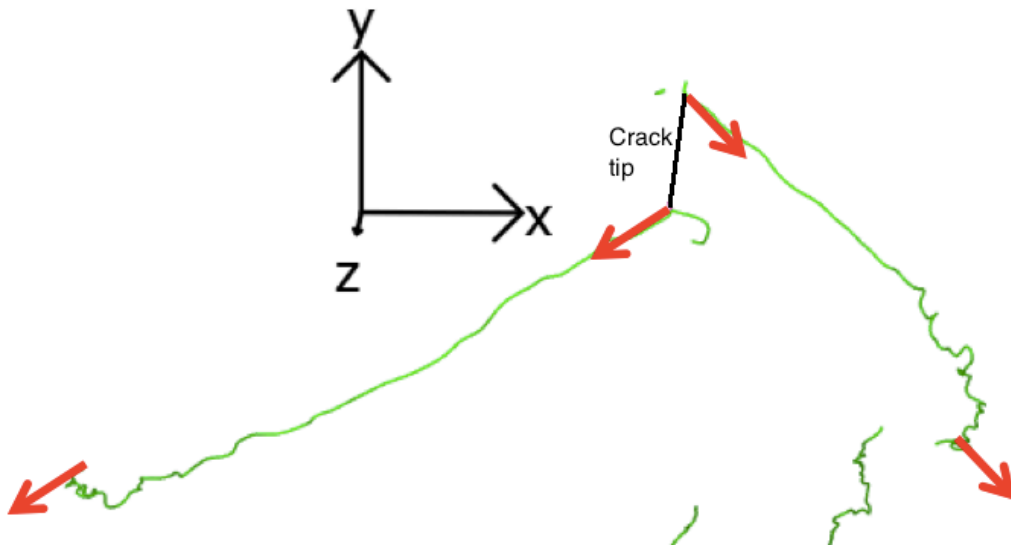


Figure 34: The red arrows represent the direction of the Burgers vector at emission point and at the edge. The Burgers vectors near the crack tip are parallel to the dislocation, and thus represent screw dislocations, whereas the remaining vectors are perpendicular to the dislocation and represent edge dislocations.

Since the CAT relies on a full dump file to do its analysis, one is limited to every 50 000th time step. To give some supplementary info, the first dislocation event is therefore found in OVITO for each cantilever. The corresponding point on the CTOD-displacement curve is then found and illustrated in Figure 35.

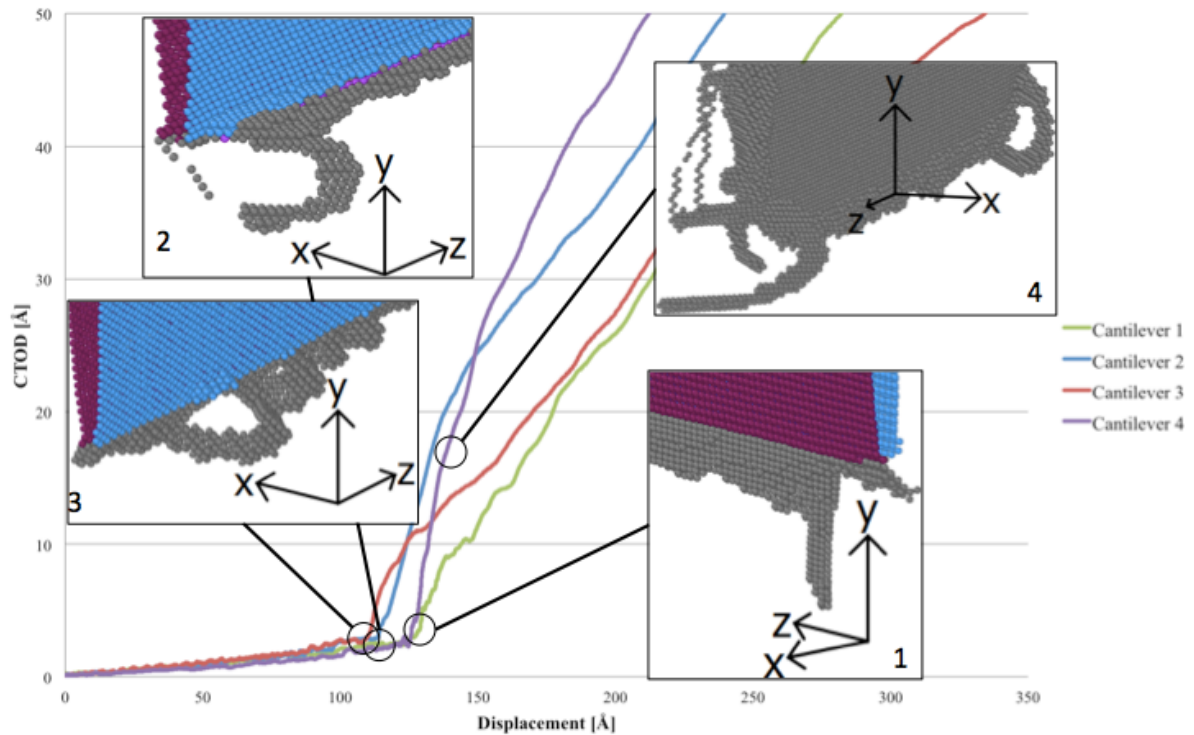


Figure 35: First dislocation event for cantilevers 1-4, placed on the related spot on the CTOD-displacement curve.

What we see in Figure 35 is that for cantilevers 1-3, the first dislocation event is happening around the point of initiation. Cantilever 4, however, has substantial crack growth before the first dislocation loop emits. This means that all the stress collected at the crack tip contributes to the cleavage fracture rather than dislocation nucleation. Cantilever 4 also emits dislocations from both edges at the same time, whereas the dislocations in beams 1-3 generally start near one of the edges.

4.5 Linear Elastic Fracture Mechanics Approach

4.5.1 Stress Intensity Factor

The stress intensity factor K is calculated at the point of crack initiation for cantilevers 1-4. This is keeping in line with the project work done preceding this thesis [2]. The three geometric shape factors presented in section 2.5.1 are applied to all cantilevers. As these calculations are done on a singular point where there is no significant crack growth, both the a/h -ratio in the shape factors and the initial crack length a are used at initial values.

Table 9: Calculated K_Q values at point of crack initiation.

K_Q [$MPa\sqrt{m}$]	Load [nN]	Wurster ²	Di Maio ³	Zhao ⁴
Cantilever 1	580	0.88	1.19	0.95
Cantilever 2	737	1.11	1.52	1.21
Cantilever 3	748	1.13	1.54	1.23
Cantilever 4	609	0.92	1.25	1.00

Table 9 shows the calculated K_Q values for cantilever 1-4 and 7. The values are well within the expected range, based on project work [2] and previous findings [20, 25, 31]. The Di Maio approach gives the largest values. The shape factor proposed by Di Maio and Roberts was based on a different width to height-ratio than Zhao's approach, and this might explain the increase in values. The Wurster approach gives the lowest numbers, though not by much. The small deviation might again be explained by the shape factor being based on a different cross section, and the adjustment made to try and meet the criteria, ref. section 2.5.1.

Cantilever 1 was researched in 2014 at a temperature of 5 K [2], and the Zhao approach was used to calculate K at the point of initiation. This research gave $K_{Zhao} = 1.03 MPa\sqrt{m}$, a value higher than the currently obtained value at 300 K. The physical parameters for these models were the same with the exception of the rounding part at the bottom of the pentagonal, but the loading is different. The beam at 5 K was run to a higher load, and the crack initiated at 838 nN. The loading for the more recent 300 K beam simulations was adjusted based on the previous 5 K research, and this will influence the values.

4.5.2 Energy Release Rate

The theoretical Griffith criterion for the energy release rate $\mathcal{G}_{Gr} = 2\gamma_s$ was compared to the K -based energy release rate $\mathcal{G} = \frac{K^2(1-\nu^2)}{E}$. The values for γ_s are found in [20], and the elasticity modulus values for the different orientation systems are obtained from [25]. It is reasonable to assume that the theoretical energy release rate will not be on point, as it is based on perfectly brittle materials such as glass. Table 10 shows \mathcal{G} obtained for each K in Table 9.

² Equations (14)-(16)

³ Equations (8)-(11), (13)

⁴ Equations (8)-(12)

Table 10: Theoretical vs. calculated energy release rate for cantilevers 1-4.

	γ_s [J/m ²]	\mathcal{G}_{Gr} [N/m]	E [GPa]	\mathcal{G}_{Wu}	\mathcal{G}_{DiM}	\mathcal{G}_{Zhao}
Cantilever 1 ₍₁₀₀₎	1.79	3.58	131	5.32	9.86	6.30
Cantilever 1 ₍₁₁₀₎	1.65	3.30	202	4.15	7.69	4.91
Cantilever 2 ₍₁₁₀₎	1.65	3.30	202	5.58	10.35	6.61
Cantilever 3 ₍₁₁₀₎	1.65	3.30	204	5.69	10.54	6.73
Cantilever 4 ₍₁₀₀₎	1.79	3.58	132	5.83	10.80	6.90

What is clear in Table 10 is that the obtained values for \mathcal{G} imply a tougher material than the Griffith criterion suggests, i.e. a higher energy level is needed for the material to break. Especially the Di Maio approach gives a very large outcome, deviating far from the Zhao and Wurster approaches which are more alike. The values obtained by the Di Maio approach may thus not be completely reliable. Pure iron has a tendency to emit dislocations and twinning, and as seen in the simulations performed, even brittle crack growth experiences dislocation emission. Dislocations require energy to move, and this will go into the consideration of \mathcal{G} . This is also explained in [8], where the Griffith equation is modified to

$$\sigma_f = \left(\frac{2E(\gamma_s + \gamma_p)}{\pi a} \right)^{1/2} \quad (29)$$

where σ_f is the fracture stress and γ_p is the *plastic work* per unit area of surface created. γ_p is typically much larger than γ_s . Ersland et al. [9] defines the total work of fracture, including plastic deformation and irreversible work, as γ_{eff} , and in turn $\mathcal{G}_C = 2\gamma_{eff}$. Based on the results in Table 10, γ_{eff} is lying in the range of 2.5 - 3.5 N/m for the Wurster and Zhao approaches, which is considerably larger than γ_s .

In cantilever 1, the crack changes direction and starts to grow on a (110) plane rather than along the crack plane (100), which is expected due to its lower surface energy. Due to the anisotropy of a BCC crystal, the modulus of elasticity changes for different orientations. Both (100) and (110) planes have been considered on the calculations of \mathcal{G} , and shown in Table 10. The calculations for the (110) plane have been made at the point of direction change rather than the first initiation. By considering the new crack direction, the values for the energy release rate decrease notably. It is reasonable that the \mathcal{G} is lower; since the crack decides to change direction, but it is questionable whether this is a more valid value to consider, as this cantilever exhibit both substantial dislocation emission and twinning.

4.6 Elastic-Plastic Fracture Mechanics Approach

4.6.1 J -integral

In a physical experiment on cantilevers, the beam is unloaded regularly to measure the compliance, and the J -integral is calculated based on the ligament size at these points. As the cantilevers modeled in this thesis do not unload, calculation points were chosen by a regular pattern: the closest 50 000th time step *before* initiation, and every 50 000 time step throughout the simulation. This was chosen based on accessible dump files of all atoms around the crack. One J for each K -approach is calculated for every step, and the shape factor is taking crack growth, i.e. a changing a/h -ratio, into consideration. The procedure for the J -calculations is explained in section 2.6.1. The crack growth is found by measuring the ligament, i.e. the length from the deepest crack point to the lowest point on the beam, for every step.

Figure 36 on the next page shows the calculated J -values plotted against the measured crack growth for cantilevers 1-4. The shape factor largely influence the outcome of J , with the Zhao approach being particularly sensitive to the growing crack. The three methods are most coherent for cantilever 3, the most ductile orientation of the four. This is also the only orientation, for which the Zhao approach does not give the highest values. This makes sense, as the Zhao approach is obviously very sensitive to crack propagation, and cantilever 3 does not propagate as the other cantilevers do.

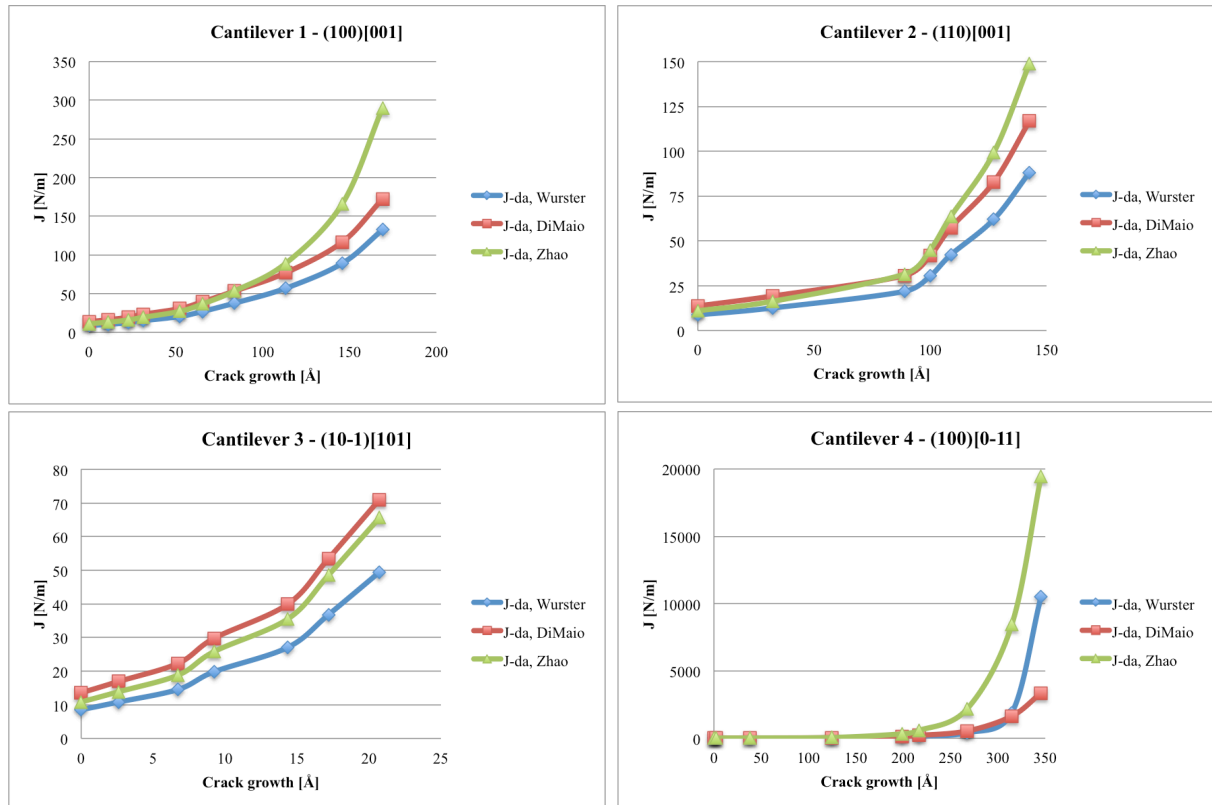


Figure 36: J vs. crack growth for cantilevers 1-4. The full size plots are included in Appendix A.

Very few reports have been made on the J -integral in atomistic modeling. Jin and Yuan [32] modeled 2D graphene and assessed the J -integral, but graphene and iron are fundamentally different and their results are not comparable. Zimmerman and Jones [33] applied the J -integral to atomistic simulations of BCC iron, and reported values of 3.42 and 3.78 J/m^2 , for first and second dislocation emission, respectively. The J -values obtained in this report is not based on dislocation emission specifically, but even so, the values reported in [33] are considerably lower. Zimmerman and Jones used a different approach than is used here; they applied the actual integral on given paths around the crack. Wurster et al. [13], which a lot of this work is based on, gets values for J in the range of about 150-1400 J/m^2 . These are however calculated for physical cantilevers and may not be comparable with the atomistic models. If we were to compare them nonetheless, the atomistic models gain lower J -values than physical cantilever, with the exception of cantilever 4. As cantilever 4 is cracking almost all the way through, crack growth and a/h -ratio is severely affected, obviously. This gives extremely high values for J , the highest almost 20 000 J/m^2 , which is not a good number for measuring fracture toughness.

In general, the values obtained for J seem to be quite large. When compared to the energy release rate, the values should be quite similar during the elastic part of the simulation, according to theory [8]. Figure 37 shows the values for J at step 1, which is still before initiation, compared to \mathcal{G} , which is calculated at the point of initiation. This small difference in calculation parameters is not considered to be of high relevance to the outcome. It is clear from the comparison that the J -integral gives much larger values for fracture toughness than

\mathcal{G} . Given that \mathcal{G} is calculated from K , and K is already argued to be quite reasonable, the J -values may be higher than they should be for this kind of experiment. What one has here, is an approach made for continuum mechanics applied directly to an atomistic model, and many approximations are done. For example, the choice of evaluation points due to lack of unloading may influence on the outcome of J . A refining of the method is probably needed for the J -integral to be more precise in atomistic simulations. It may be worth looking into obtaining it by creating a path and calculating the integral over it.

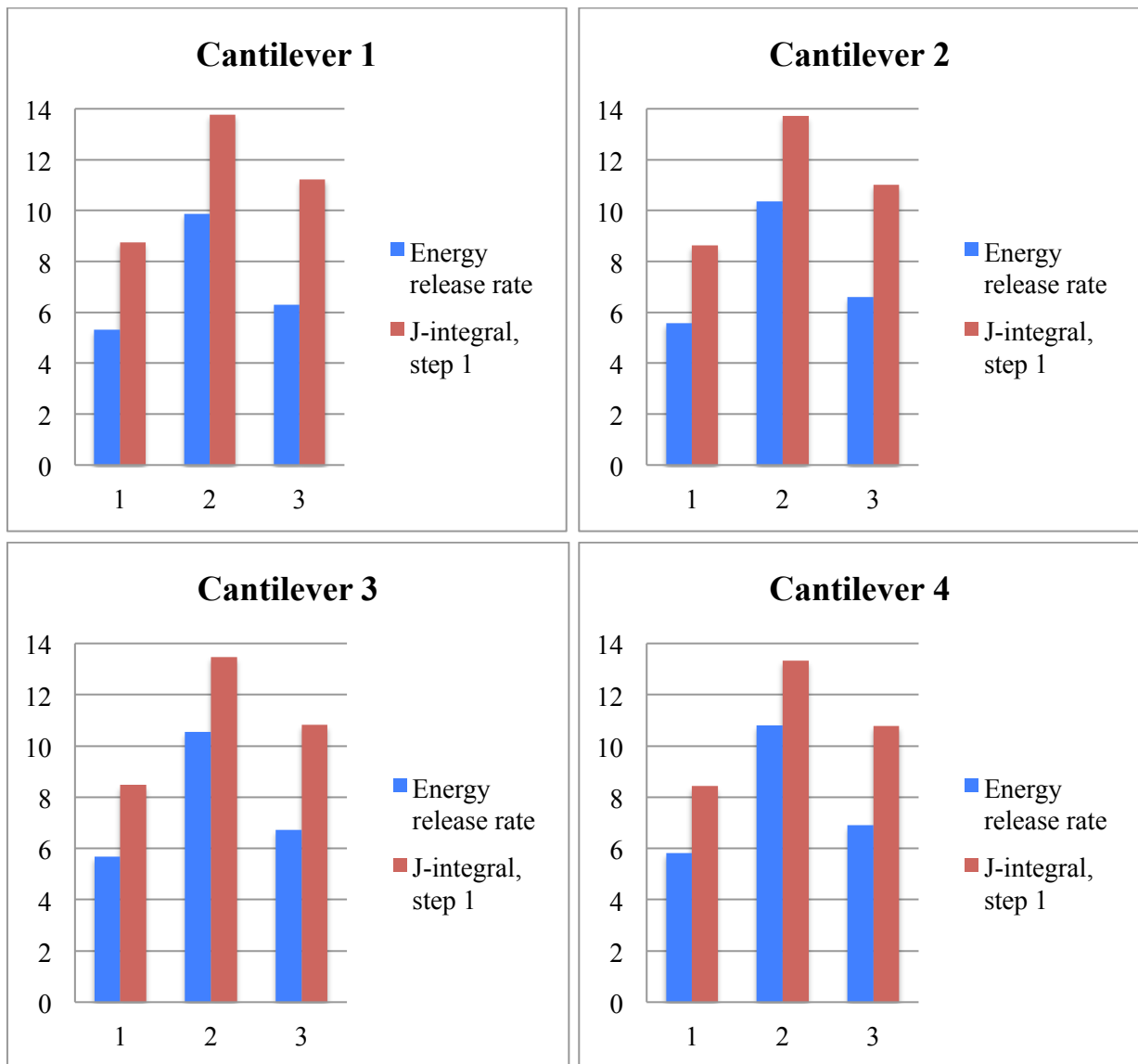


Figure 37: Energy release rate \mathcal{G} compared to the J -integral for cantilevers 1-4. Both energy release rate and J -integral are given in J/m^2 . (1) is Wurster approach, (2) is Di Maio approach and (3) is Zhao approach.

Effect of constant shape factor

Figure 38 shows the calculated J -values when crack growth is not taken into consideration, for cantilever 1. Compared to the plots for cantilever 1 in Figure 36, the obtained values for J are much lower, and will therefore give a more conservative result. This also concludes the Zhao approach's sensitivity for crack growth. The general look of the plots on Figure 38 is much more similar to that of orientation 3 in Figure 36.

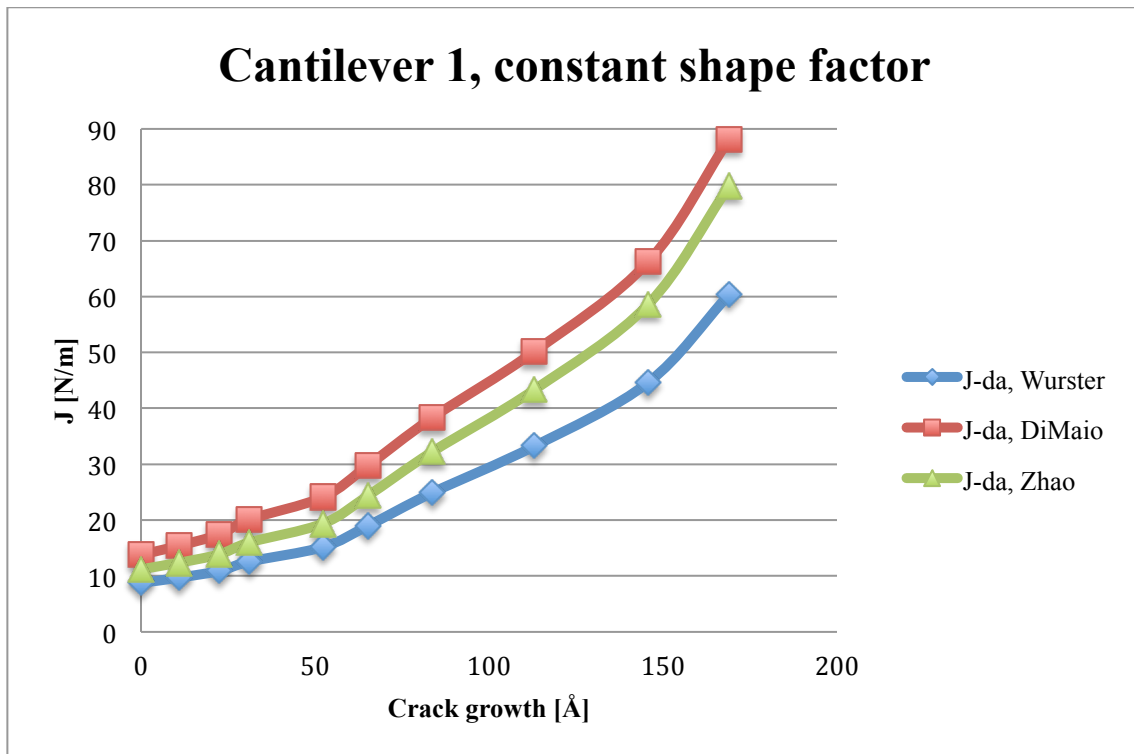


Figure 38: J vs. crack growth for cantilever 1, with a constant shape factor and crack depth a .

4.6.2 Stress Intensity Factor

A new value for K was obtained by the use of J and equation (23). The value for $K_{Q,J}$ is chosen at evaluation point 2 of the J -calculations, and shown in Figure 39 compared to its corresponding K_Q found by the LEFM approach. The evaluation point was chosen due to it being the first point after crack initiation, as J has not been calculated at exactly the initiation point.

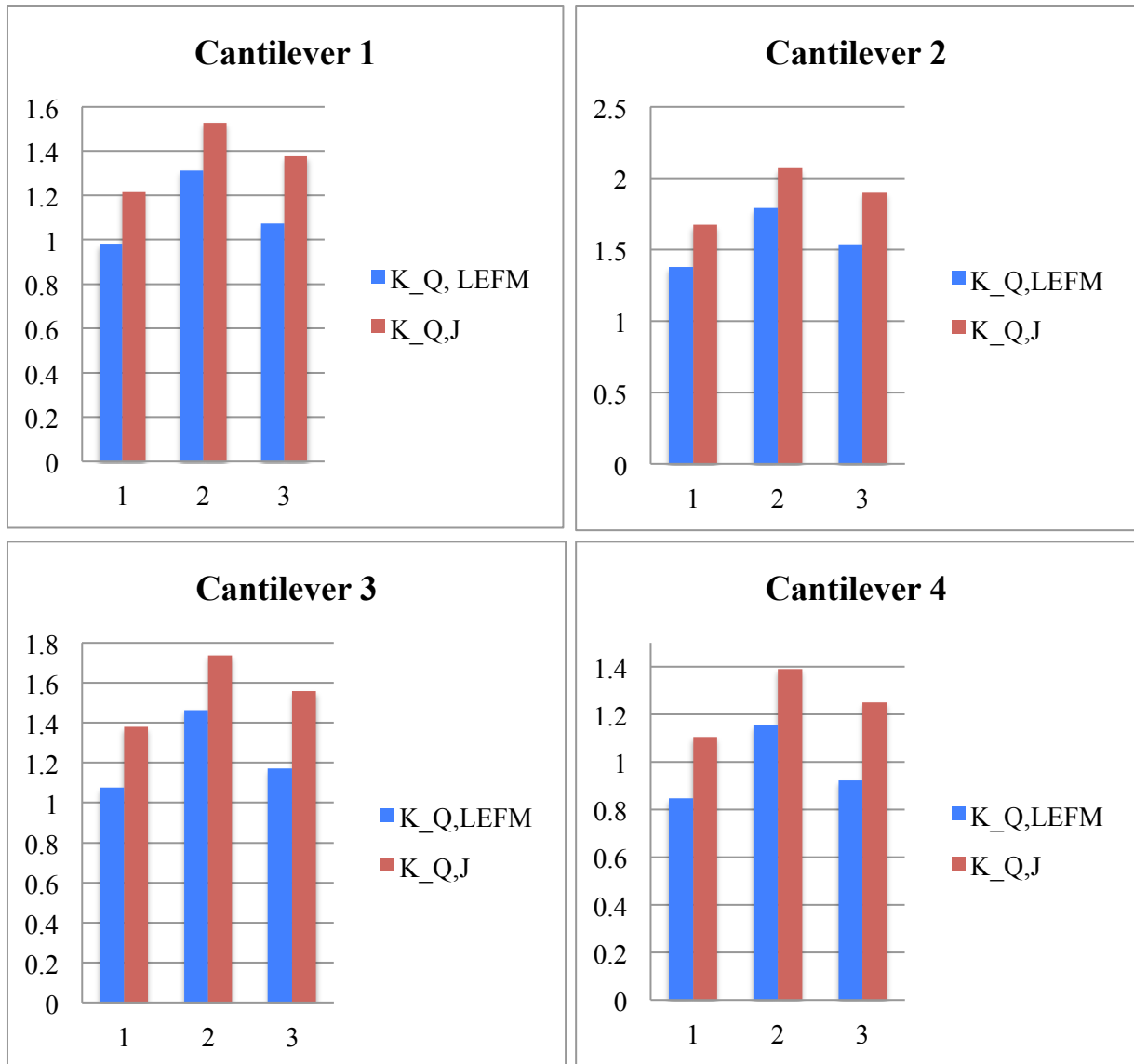


Figure 39: The two different K -values for cantilevers 1-4, at evaluation point 2. (1) is Wurster approach, (2) is Di Maio approach and (3) is Zhao approach.

The trend in Figure 39 is that the J -based K is higher than the LEFM-based K . This is expected, due to the fact that J grows with a growing crack, and the LEFM approach is only valid for the linear elastic part of the simulation. The Di Maio approach also gives the largest outcome, which is consistent with what is already presented in section 4.5.1. It is interesting to observe that the highest values, both LEFM and J -based, occur in cantilever 2, since cantilever 3 displays the most resistance to crack growth. Contrary to what one would expect, the difference in fracture behavior does not influence much on the calculations.

4.6.3 Crack Tip Opening Displacement

The energy release rate \mathcal{G} and the measured CTOD value at the point of initiation is utilized further by calculating a value for the yield stress σ_y by the use of equation (25). Even though the crack growth at this point is set to be zero, the crack has still started to open, hence the

available value for CTOD. The results are shown in Table 11. Based on the crack behavior of the cantilever beams, a state of plane strain is assumed, and the m mentioned in equation (25) is set to be 2.0 [8].

Table 11: The calculated values for yield stress σ_y .

	$CTOD [\text{\AA}]$	$\sigma_{y,theory}$ [GPa]	$\sigma_{y,Wurster}$ [GPa]	$\sigma_{y,DiMaio}$ [GPa]	$\sigma_{y,Zhao}$ [GPa]
Cantilever 1 ₍₁₀₀₎	4.15	4.31	6.40	11.87	7.58
Cantilever 1 ₍₁₁₀₎	6.45	2.56	3.22	5.96	3.81
Cantilever 2	2.99	5.52	9.34	17.31	11.06
Cantilever 3	3.86	4.28	7.37	13.66	8.72
Cantilever 4	2.82	6.35	10.33	19.15	12.23

Based on simulations done on pure iron nanopillars [34], the yield stress was expected to lie in the 8-10 GPa range. As expected based on the obtained values for \mathcal{G} , the Di Maio method gives very high yield stress values, whereas the other two methods produce numbers for the yield stress that are well within the expected values. Going back to section 4.5.2, this would suggest that the calculated values for \mathcal{G} are reasonable, agreeing with the notion that the simplest Griffith criterion is not well fitted for this kind of experiment. It also implies that the measuring of CTOD is a good procedure. As previously discussed in section 4.6.1, the J -values seemed a bit high compared to the values for \mathcal{G} . When concluding that \mathcal{G} is reasonable, that will also suggest that the values for J are higher than they should. It is also reasonable to conclude that the Di Maio approach is not the most reliable for these calculations.

Cantilever 1 grows on two different planes; first (100) and then it changes to the (110) plane. The values calculated for this beam is done at the point of crack initiation for (100), and at the point of direction change for (110). The lower energy release rates presented in section 4.5.2 will obviously provide a lower yield stress. The yield stresses for cantilever 1₍₁₁₀₎ are way below what is expected. This might be due to the fact that it is obtained at a point after what can be conceived as yield in the specimen, but there is no evident reason why this beam should display a lower yield stress than the other beams.

The validity of K_Q was checked based on the obtained yield stress values, by the use of equation (7). Excluding the values for the Di Maio approach and the lowest yield stresses for cantilever 1, the validity was checked for the highest and lowest yield stress, and their corresponding K-value. For the lowest yield stress (Wurster approach, cantilever 1), w , a and $(h-a)$ need to be larger than 473 Å, hence this K is not valid as K_{Ic} . For the highest yield stress (Zhao approach, cantilever 4), the same parameters need to be larger than 167 Å. This would be OK for $(h-a)$ and w , but the notch depth at 120 Å is still too small for the value to be defined as K_{Ic} .

4.7 Comparison with Physical Experiments

NOTE: This section is written in cooperation with Brage D. Snartland and Aksel L.L. Kvaal, and will as a whole also appear in their theses.

M. Jørum has in this thesis been modeling pure iron cantilevers atomistically at room temperature, and B.D. Snartland [35] and A.L.L. Kvaal [36] have been loading pure iron cantilevers. This section is dedicated to identify possible correlations between practical experiments and atomistic modeling. The cantilevers are pentagonal, calculations have been executed based on the same assumptions, and using the same methods. Detailed theory related to atomistic modeling and fracture mechanics is described in Jørum's Master thesis, and theory related to material behavior and fracture mechanics is described in Snartland's and Kvaal's Master theses.

Figure 40 shows the calculated or measured crack growth for both pure iron cantilevers and a modeled cantilever. The modeled cantilever is connected to the right hand side y-axis due to its smaller size resulting in smaller values. There is a clear correlation in crack behavior for the cantilevers. All cantilevers exhibit slow crack growth after the initial unloading steps, before accelerating at the later unloading steps. Note that the modeled cantilever does not unload, and the measuring steps are chosen according to simulation time steps.

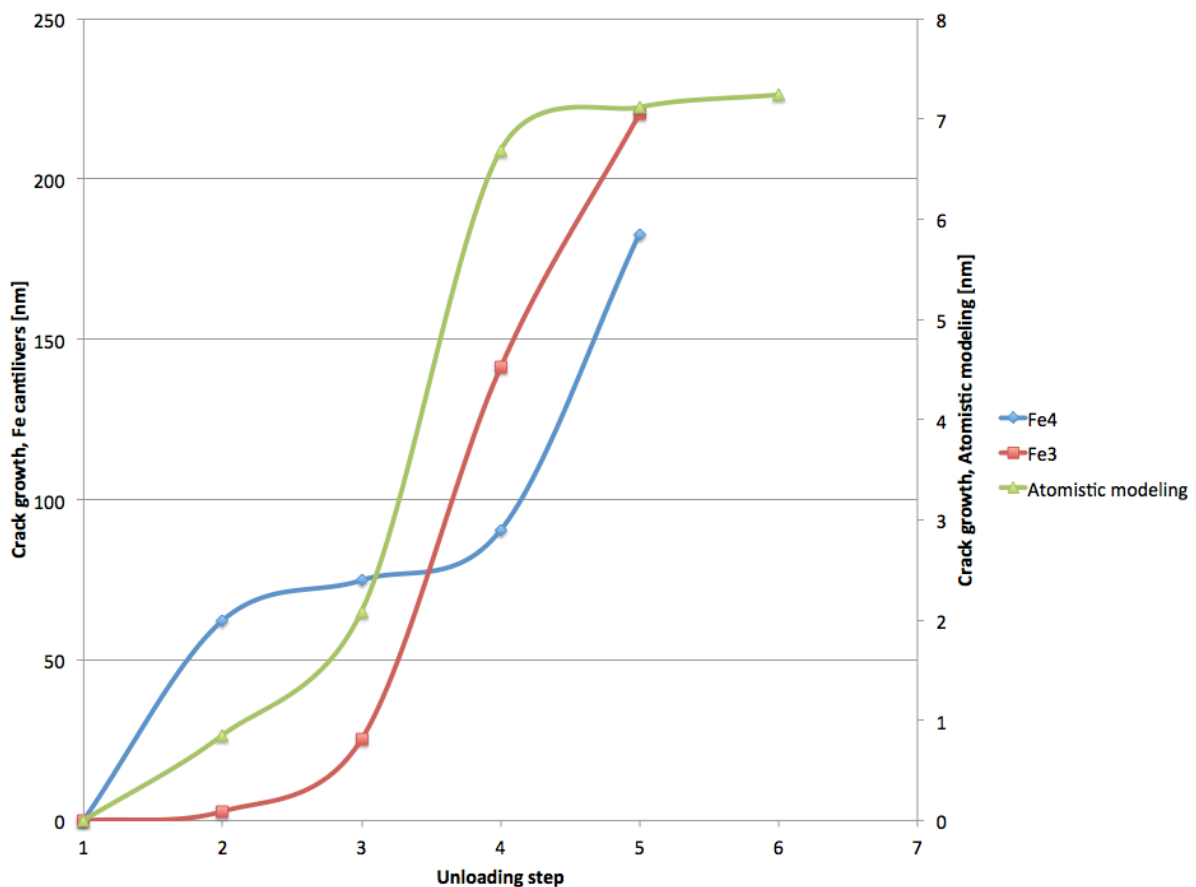


Figure 40: Crack growth for physical pure iron cantilevers compared to atomistic model of cantilever beam.

Figure 41 shows J - Δa curves for the atomistically modeled cantilever and both pure iron cantilevers. Both the pure iron cantilevers have higher J -values than the simulated cantilever, meaning that the modeled cantilever is less tough than the pure iron cantilevers. A possible explanation is the difference in loading rate, which is significantly larger for the atomistic model. The modeled notch is also atomistically sharp, while the machined notches are substantially blunter. A sharp tip requires less energy to propagate a crack compared to a blunt tip.

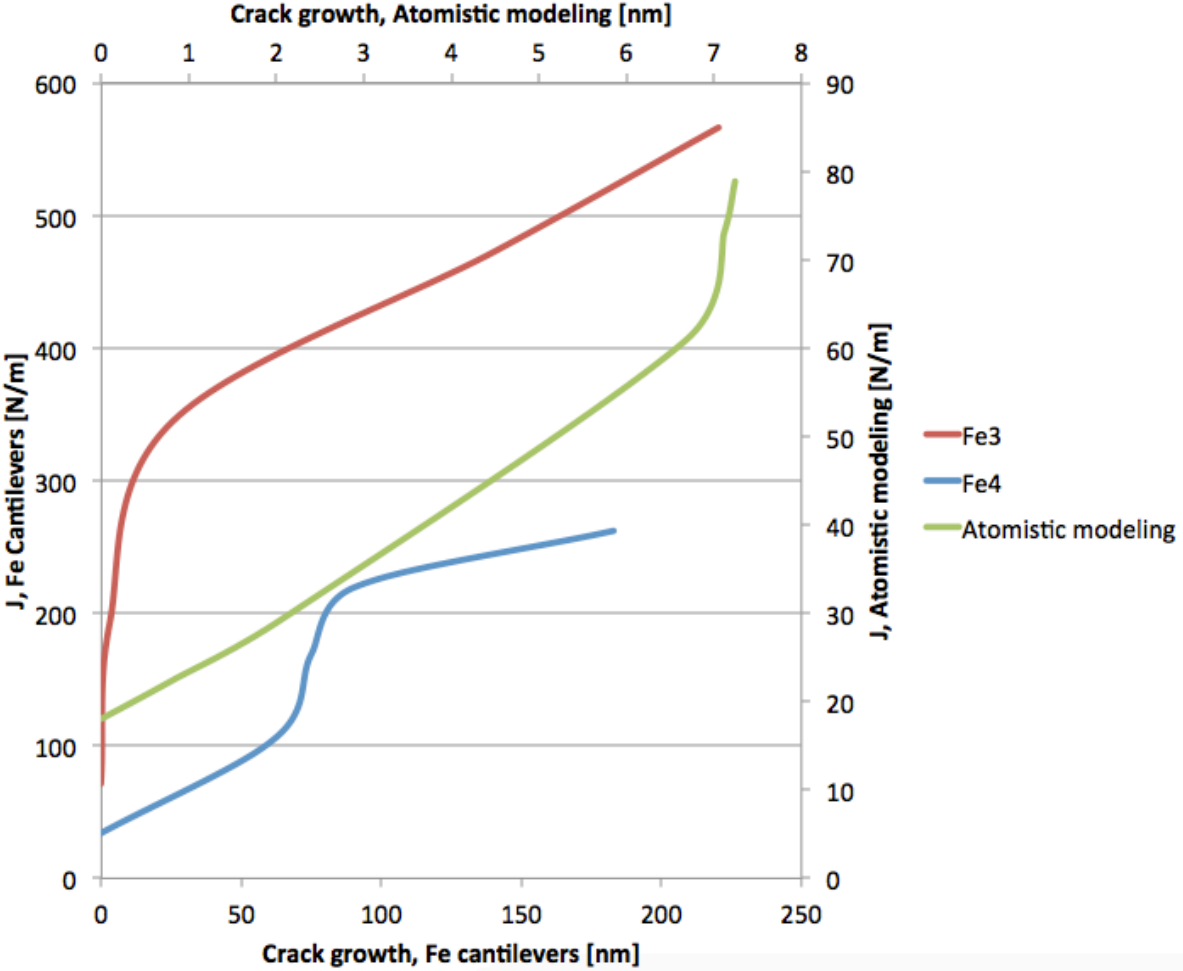


Figure 41: J vs. crack growth for physical cantilever and atomistic model of cantilever beam.

Figure 42 shows the critical stress intensity factors for the different cantilevers, taken after the largest jump in crack growth. The K -values are lower for the modeled cantilever than the machined cantilevers. This was expected due to the differences in the calculated J -values, already, and is also attributed to the differences in loading rate and notch geometry.

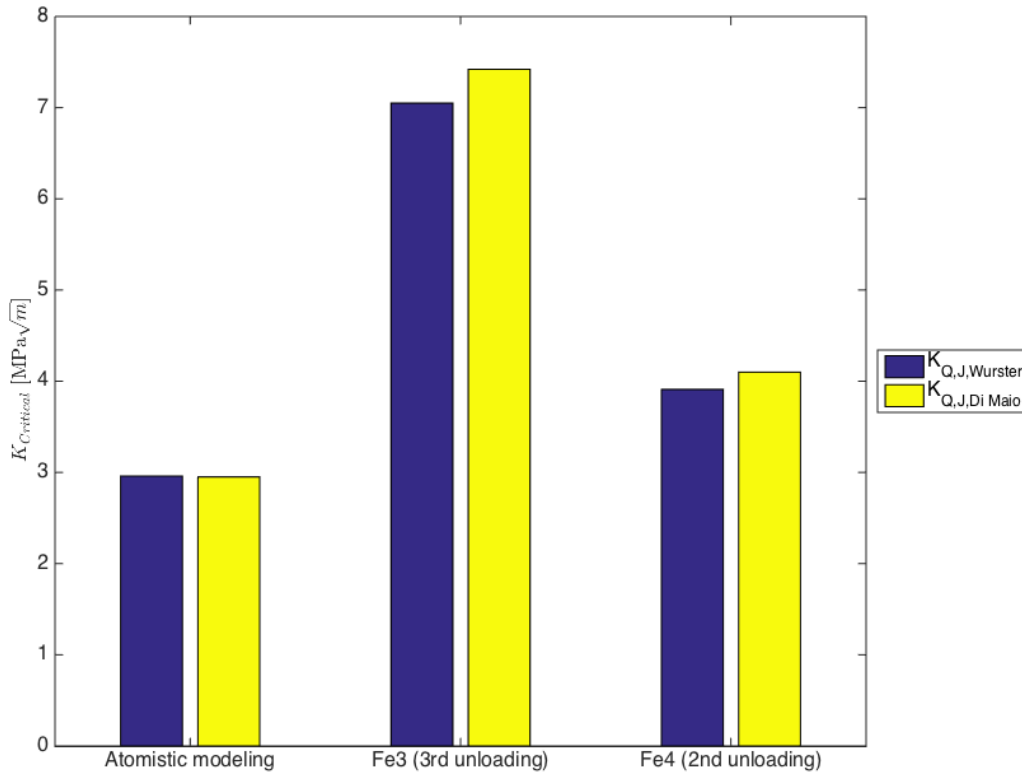


Figure 42: K_{QJ} for physical cantilever and atomistic model of cantilever beam. The value is calculated with Wurster and Di Maio approaches, at the step after most crack growth (step 4 for atomistic model).

The real cantilevers and the modeled cantilever displayed similar deformation behavior. However, the notch geometry, loading rate and specimen size influence the quantitative data obtained. The loading rate is significantly different; the machined cantilevers are loaded by a unit of $\mu\text{m}/\text{min}$, while the modeled beams are loaded by a real time rate of m/s . The different notch geometries are strongly affecting the fracture properties of the cantilevers, which is in accordance with literature [37, 38]. The size is typically differing by one order of magnitude. Another aspect to consider is that the modeled material is perfect and defect-free, whereas the pure iron used to machine cantilevers in the lab contains several types of defects; these affect the material properties and fracture behavior.

4.8 Remarks

There are many obstacles to cross when going from continuum mechanics to the atomistic level. MD simulations depend on computational power, and even though the computers are getting more powerful every year, there is still a long way to go before MD meet physical experiments. The deformation rate used in simulations is usually in the 10^8 s^{-1} order of magnitude, whereas a similar physical experiment will be performed at the order of 10^{-3} s^{-1} . High deformation rate is known to affect the material behavior during fracture, and the rate obtained in MD simulations is particularly high. The time steps need to be small enough to capture the highest frequency motion of the vibrating atom bonds, giving a typical time step

value in the order of femtoseconds (fs, 1×10^{-15} s). In the case of this thesis, the time step is set to be 1.5 fs. This gives a simulation of 1 million time steps a real time of 1×10^{-9} s, namely 1 nanosecond.

Size is another issue, again limited by computational power. The largest reasonable simulation scenario lies at approximately 50 million atoms, suggesting a three-dimensional box of about 50 nm^3 , whereas the smallest reasonable volume for equivalent testing in the laboratory would be closer to 5000 nm^3 .

Another aspect is the potentials used for atomistic simulations. There are a vast number of potentials to choose from, but they are all approximations to the real material and will always have some limitations. For instance, as mentioned in section 2.1.1, the EAM potential does not take directional bonding into consideration, whereas the more accurate bond-order potential requires such a high level of computational power for it to be a reasonable choice in many applications. In addition, while there are well-developed potentials for pure materials, there are still no potentials for the classic engineering material: steel. This means that the simulations performed in this work are done in pure iron, in contrast to a structure in the Arctic that would most likely be made of steel.

5 Conclusion

Molecular Dynamics simulations have been conducted to highlight the fracture behavior of a full-3D cantilever beam on the nano scale. The effect of crystallographic orientations, crack geometry and loading rate was researched, and both stress intensity factor K and J -integral were calculated for the cantilevers. In general, the behavior of the beam seems to agree with continuum theory, and shows promise of being a realistic model for further research.

Crystallographic orientation proved to have high influence on the general fracture behavior of the cantilever beams. They all showed signs of continuum mechanics manners, which is interesting due to the very small sample size. Two of the beams were influenced by a triaxial stress state, causing the crack to cleave in the middle of the model, yet blunt the crack tip on the edges. The remaining two cantilevers displayed ductile and brittle fracture respectively. The behavior of the cantilever beams with the different orientations was discussed with regards to relevant theory and previous studies on similar models, and showed generally good agreement with previous findings.

Two different loading rates were investigated, with simulations running over 1 million time steps and 2 million time steps, respectively. The difference in loading rate did not in any particular way influence the fracture behavior. The difference between the two loading rates may be too small for it to be very significant, as the loading rate is still very high. Due to computational time being quite long for these large models, no longer attempts were made in this report, but would be interesting to look further into.

Two different crack geometries were investigated, by the cooperation with concurrent Ph.D. work. A sharper crack produced more brittle, clean crack growth, but the general crack behavior showed the same trends.

Stress intensity factor K_Q was obtained for cantilevers 1-4, giving expected values for the most part. The K values were used further, by calculating the energy release rate \mathcal{G} , and comparing it to the theoretical energy release rate as given by the Griffith criterion. The Di Maio approach to the problem gave very large values, about three times the Griffith values, whereas the Wurster and Zhao approaches gave values about 1.5 times the Griffith value. This yields that the Griffith criterion is not valid for materials that are not perfectly brittle, which is in good agreement with theory.

J was computed for cantilevers 1-4, including all three shape factors considered. The values are highly affected by their corresponding shape factor. When calculating J , crack growth Δa and thus an increasing a/h -ratio was taken into consideration, and especially the Zhao approach showed high sensitivity to crack growth. The effect of keeping the shape factor at constant a and a/h values was displayed for cantilever 1, and proved to give a more conservative result than for a changing shape factor. The values for J was compared to the energy release rate \mathcal{G} , and concluded to be slightly higher than expected. The method for

obtaining J in these kinds of simulations will probably need some adjustments to be a better measure.

The measured CTOD was connected to the calculated values for energy release rate \mathcal{G} to find prospective values for the yield stress σ_y . The Di Maio approach was disqualified in this calculation, as it returned unreasonably large values for yield stress. The Zhao and Wurster approaches, however, returned very good values well within what has been obtained in atomistic modeling of nanopillars. This implies that the acquired values for \mathcal{G} are good and valid. The yield stress was in turn used to check the validity of K_Q as K_{Ic} , but it was deemed not valid.

The atomistic model was compared to similar, physical experiments. The values for J and $K_{Q,J}$ were plotted against one another, and showed that the atomistic model had lower values, indicating a lower stress needed to initiate crack propagation. This was probably caused by the substantial difference in loading rate, as well as notch geometry and size effects.

6 Further Work

The journey of atomistic modeling has only just begun, and with the ever-evolving technology it will be interesting to watch the development of these kinds of simulations. If time had allowed, more aspects of this work would have been interesting to research further.

Considering this work is meant for investigating the Arctic environment, the effect of temperature should definitely be researched better. It is common to do MD simulations at temperatures of 0 K, but as this temperature is not really feasible in real life, the range from 0°C to -100°C is more interesting.

Computational time is an issue with MD simulations, even running on a high-class supercomputer, a simulation over 1 million time steps takes several days to finish. But if time allows, an as low as possible loading rate would be highly interesting to study, as loading rate is one of the biggest factors limiting MD from real life experiments.

The crack tip response is mentioned in the background part of this thesis, but was not taken into consideration when analyzing results. The effect of stacking faults is a very interesting field to look into.

An attempt to unload the beam, similar to what is done in the lab, was done while working with this thesis. A special dump file for restarting the simulation was put out regularly, and then the simulation was reversed from the current load. There were issues with the boundary conditions, and the attempt was categorized as a failure, but it would be interesting to see if this will have any impact on the full deformation process of the beam.

A lot of other factors could be taken into consideration when doing these kinds of computational experiments, such as other orientations, specimen size, notch depth and general beam geometry. The deflection could also be displacement controlled instead of load controlled.

7 References

1. Buehler, M.J., *Atomistic Modeling of Materials Failure*. 2008: Springer US.
2. Jørum, M., *Atomistic Modeling of Cantilever Beam* in *Department of Engineering Design & Materials*. 2014, NTNU.
3. Erslund, C.H., *Atomistic Modeling of Fracture in Iron*, in *Engineering Design and Materials*. 2012, NTNU: NTNU.
4. Callister, W.D., *Materials Science and Engineering, 8th Edition SI Version*. 2010: Wiley. 1000.
5. Hull, D. and D.J. Bacon, *Introduction to Dislocations*. 2011: Elsevier Science.
6. Alexander, S., V.B. Vasily, and A. Athanasios, *Automated identification and indexing of dislocations in crystal interfaces*. *Modelling and Simulation in Materials Science and Engineering*, 2012. **20**(8): p. 085007.
7. Alexander, S. and A. Karsten, *Extracting dislocations and non-dislocation crystal defects from atomistic simulation data*. *Modelling and Simulation in Materials Science and Engineering*, 2010. **18**(8): p. 085001.
8. Anderson, T.L., *Fracture Mechanics Third Edition*. 2005: CRC Press. 640.
9. Erslund, C.H., et al., *Atomistic modeling of micromechanisms and T-stress effects in fracture of iron*. *Engineering Fracture Mechanics*, 2012. **79**(0): p. 180-190.
10. ASTM International, W.C., PA, *ASTM E-399-12e3, Standard test Method for Linear-Elastic Plane-Strain Fracture Toughness K_{Ic} of Metallic Materials*. 2012.
11. Zhao, X., et al., *Mechanical properties of SiC coatings on spherical particles measured using the micro-beam method*. *Scripta Materialia*, 2008. **59**(1): p. 39-42.
12. Di Maio, D. and S.G. Roberts, *Measuring fracture toughness of coatings using focused-ion-beam-machined microbeams*. *Journal of Materials Research*, 2005. **20**(02): p. 299-302.
13. Wurster, S., C. Motz, and R. Pippan, *Characterization of the fracture toughness of micro-sized tungsten single crystal notched specimens*. *Philosophical Magazine*, 2012. **92**(14): p. 1803-1825.
14. Rice, J.R., *A Path Independent Integral and the Approximate Analysis of Strain Concentration by Notches and Cracks*. *Journal of Applied Mechanics*, 1968. **35**(2): p. 379-386.
15. Rice, J.R. and G.F. Rosengren, *Plane strain deformation near a crack tip in a power-law hardening material*. *Journal of the Mechanics and Physics of Solids*, 1968. **16**(1): p. 1-12.
16. Hutchinson, J.W., *Singular behaviour at the end of a tensile crack in a hardening material*. *Journal of the Mechanics and Physics of Solids*, 1968. **16**(1): p. 13-31.
17. ASTM International, W.C., PA, *ASTM E1820-13, Standard Test Method for Measurement of Fracture Toughness*. 2013.
18. Wells, A.A., *Unstable Crack Propagation in Metals: Cleavage and Fast Fracture*. *Proceedings of the Crack Propagation Symposium*, 1961. **1**.
19. deCelis, B., A.S. Argon, and S. Yip, *Molecular dynamics simulation of crack tip processes in alpha - iron and copper*. *Journal of Applied Physics*, 1983. **54**(9): p. 4864-4878.
20. Gordon, P., et al., *Crack-Tip Deformation Mechanisms in α -Fe and Binary Fe Alloys: An Atomistic Study on Single Crystals*. *Metallurgical and Materials Transactions A*, 2007. **38**(13): p. 2191-2202.
21. Machová, A. and G.E. Beltz, *Ductile–brittle behavior of (001)[110] nano-cracks in bcc iron*. *Materials Science and Engineering: A*, 2004. **387–389**(0): p. 414-418.

22. Hora, P., et al., *Crack induced slip processes in 3D*. Engineering Fracture Mechanics, 2008. **75**(12): p. 3612-3623.
23. Vatne, I.R., et al., *Quasicontinuum simulation of crack propagation in bcc-Fe*. Materials Science and Engineering: A, 2011. **528**(15): p. 5122-5134.
24. Vatne, I.R., et al., *Three-dimensional crack initiation mechanisms in bcc-Fe under loading modes I, II and III*. Materials Science and Engineering: A, 2013. **560**(0): p. 306-314.
25. Erslund, C.H., I.R. Vatne, and C. Thaulow, *Atomistic modeling of penny-shaped and through-thickness cracks in bcc iron*. Modelling and Simulation in Materials Science and Engineering, 2012. **20**(7): p. 075004.
26. Kelly, A., W.R. Tyson, and A.H. Cottrell, *Ductile and brittle crystals*. Philosophical Magazine, 1967. **15**(135): p. 567-586.
27. Rice, J.R. and R. Thomson, *Ductile versus brittle behaviour of crystals*. Philosophical Magazine, 1974. **29**(1): p. 73-97.
28. Rice, J.R., *Dislocation nucleation from a crack tip: An analysis based on the Peierls concept*. Journal of the Mechanics and Physics of Solids, 1992. **40**(2): p. 239-271.
29. Plimpton, S., *Fast Parallel Algorithms for Short-Range Molecular Dynamics*. Journal of Computational Physics, 1995. **117**: p. 19.
30. Stukowski, A., *Visualization and analysis of atomistic data with OVITO - the Open Visualization Tool*. Modelling and Simulation in Materials Science and Engineering, 2010. **18**(1).
31. Möller, J.J. and E. Bitzek, *Comparative study of embedded atom potentials for atomistic simulations of fracture in α -iron*. Modelling and Simulation in Materials Science and Engineering, 2014. **22**(4): p. 045002.
32. Jin, Y. and F.G. Yuan, *Atomistic simulations of J-integral in 2D graphene nanosystems*. Journal of Nanoscience and Nanotechnology, 2005. **5**(12): p. 2099-107.
33. Zimmerman, J.A. and R.E. Jones, *The application of an atomistic J-integral to a ductile crack*. Journal of Physics: Condensed Matter, 2013. **25**(15): p. 155402.
34. Rogne, B.R.S., *Nanomechanical testing of iron and steel*, in *Engineering Design and Materials*. 2014, NTNU: NTNU.
35. Snartland, B.D., *Nanomechanical Testing of CGHAZ of Arctic Steel*, in *Engineering Design and Materials*. 2015, NTNU: NTNU.
36. Kvaal, A.L.L., *Nanomechanical Testing of ICCGHAZ of Arctic Steel*, in *Engineering Design and Materials*. 2015, NTNU: NTNU.
37. Ciornei, F.C., et al., *The Effect of Notch Geometry upon Shear Stress State in a Beam*. Mechanical Testing and Diagnosis, 2012. **2**: p. 68-76.
38. Matoy, K., et al., *A comparative micro-cantilever study of the mechanical behavior of silicon based passivation films*. Thin Solid Films, 2009. **518**(1): p. 247-256.

8 Acknowledgments

Working with this thesis has been a challenging and wonderful journey. I have gotten lost in the atomistic world, and found my way back again. Along the way I learned a lot, both dos and don'ts, and I am left with a feeling of knowing everything and nothing at the same time. I am lucky to have had a lot of people around me to help me through all the ups and downs, and so many deserve my thanks.

First of all, I would like to thank my supervisor professor dr.ing. Christian Thaulow for being ever so inspiring and enthusiastic, and always having an open door for his students. I hope your plants start humming Mozart soon ☺

PhD candidate Jørn Skogsrud has been my go-to guy through this whole experience, and he has become a good friend as well as always helping me with all my questions. Thank you so much for sushi, mango, cake and all the fun we have had!

Håkon A. Gundersen, Anette B. Hagen and Bjørn Rune S. Rogne deserve thanks for being patient, listening and always supplying information where needed.

Brage D. Snartland and Aksel L.L. Kvaal have been good cooperators and very helpful in times of need, and I thank them for this.

A big thank you must go to Inga G. Ringdalen for invaluable input, and to her colleagues for choosing an impeccable time to stop by her office.

Heikki Sjöman for providing valuable feedback in the crucial finishing week.

Special thanks go to NTNU and the Department of Engineering Design and Materials, NOTUR (Norwegian High Performance Computing), and Sintef's project Arctic Materials 2 for giving me the opportunity to work on such an interesting subject.

And to all the rest of the people around me, thanks for the lunches, dinners, talks, laughs and for making every day brighter!

Appendix A: J - Δa Plots

This appendix contains the full-sized version of the plots shown in Figure 36 in section 4.6.1.

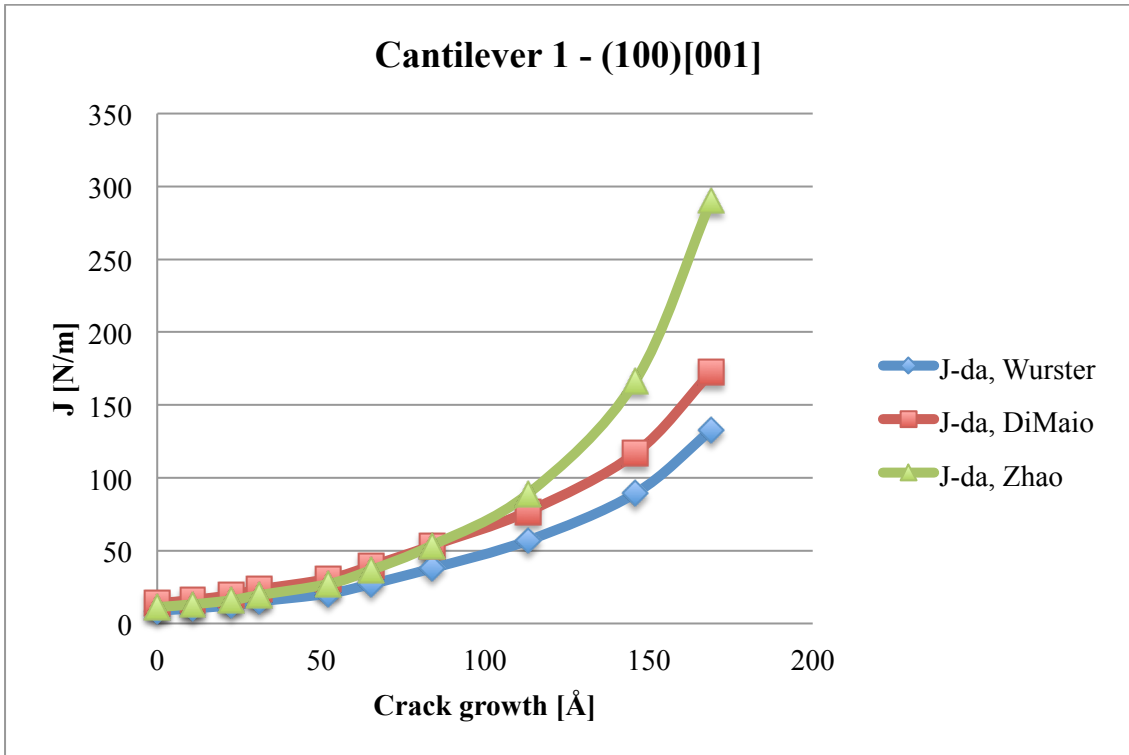


Figure 43: J - Δa plots for cantilever 1.

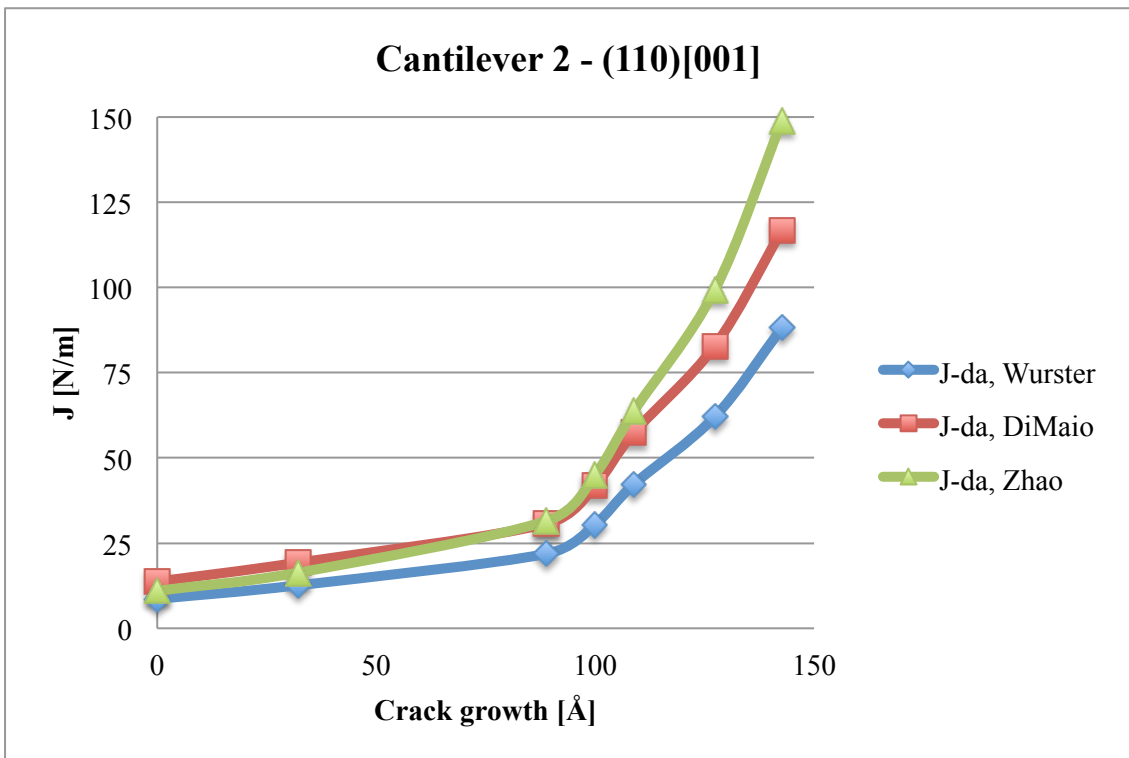


Figure 44: J - Δa plots for cantilever 2.

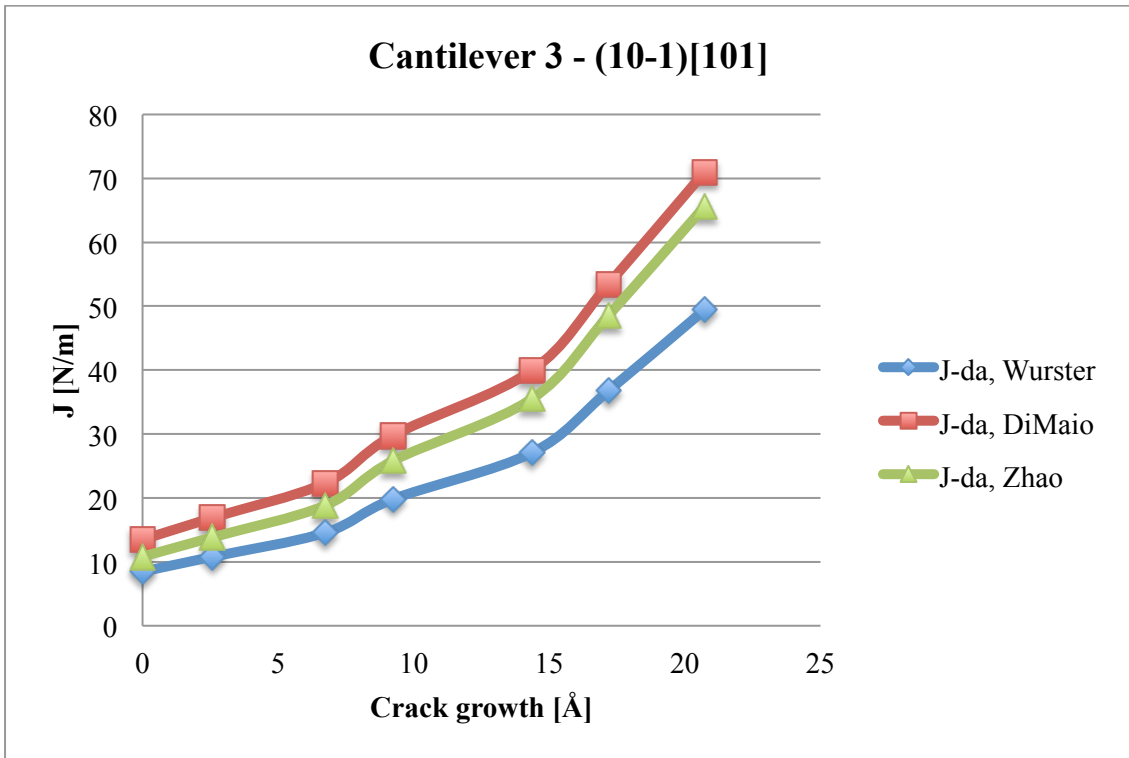


Figure 45: J - Δa plots for cantilever 3.

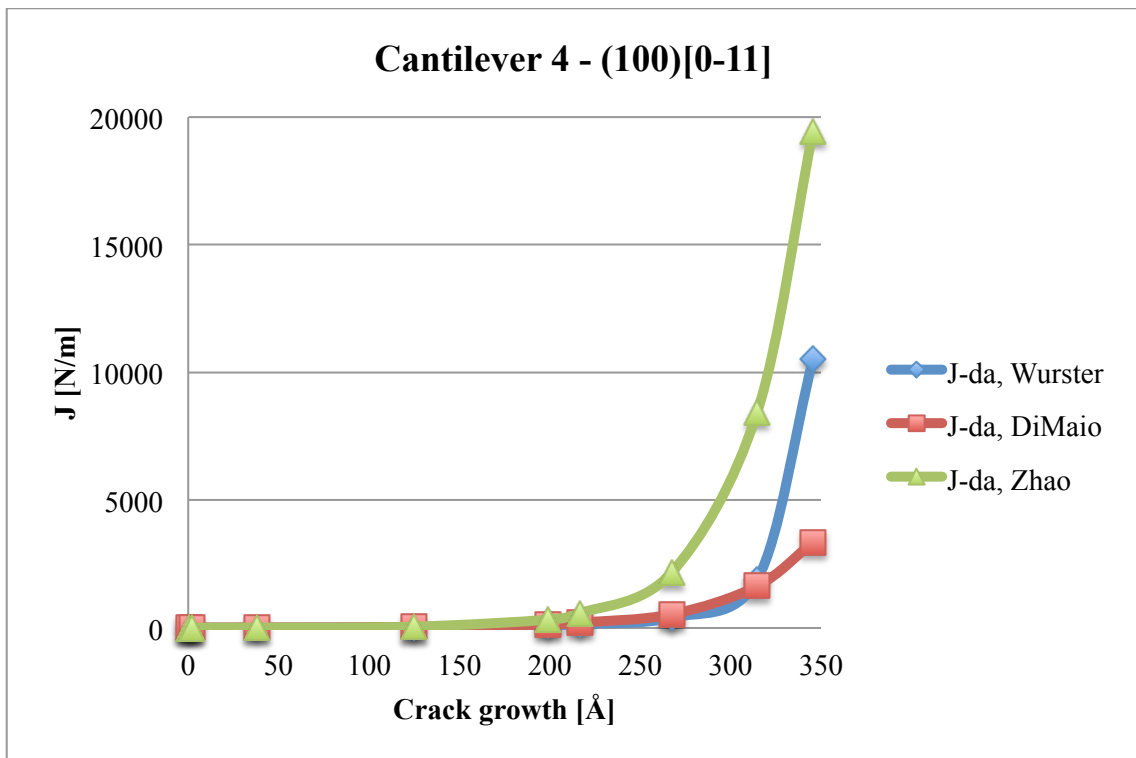


Figure 46: J - Δa plots for cantilever 4.

Appendix B: Through-thickness Crack Growth

The following figure illustrates the growth for cantilevers 1-4 at both edges and in the center of the beam, at CTOD values ranging from 35-39 Å.

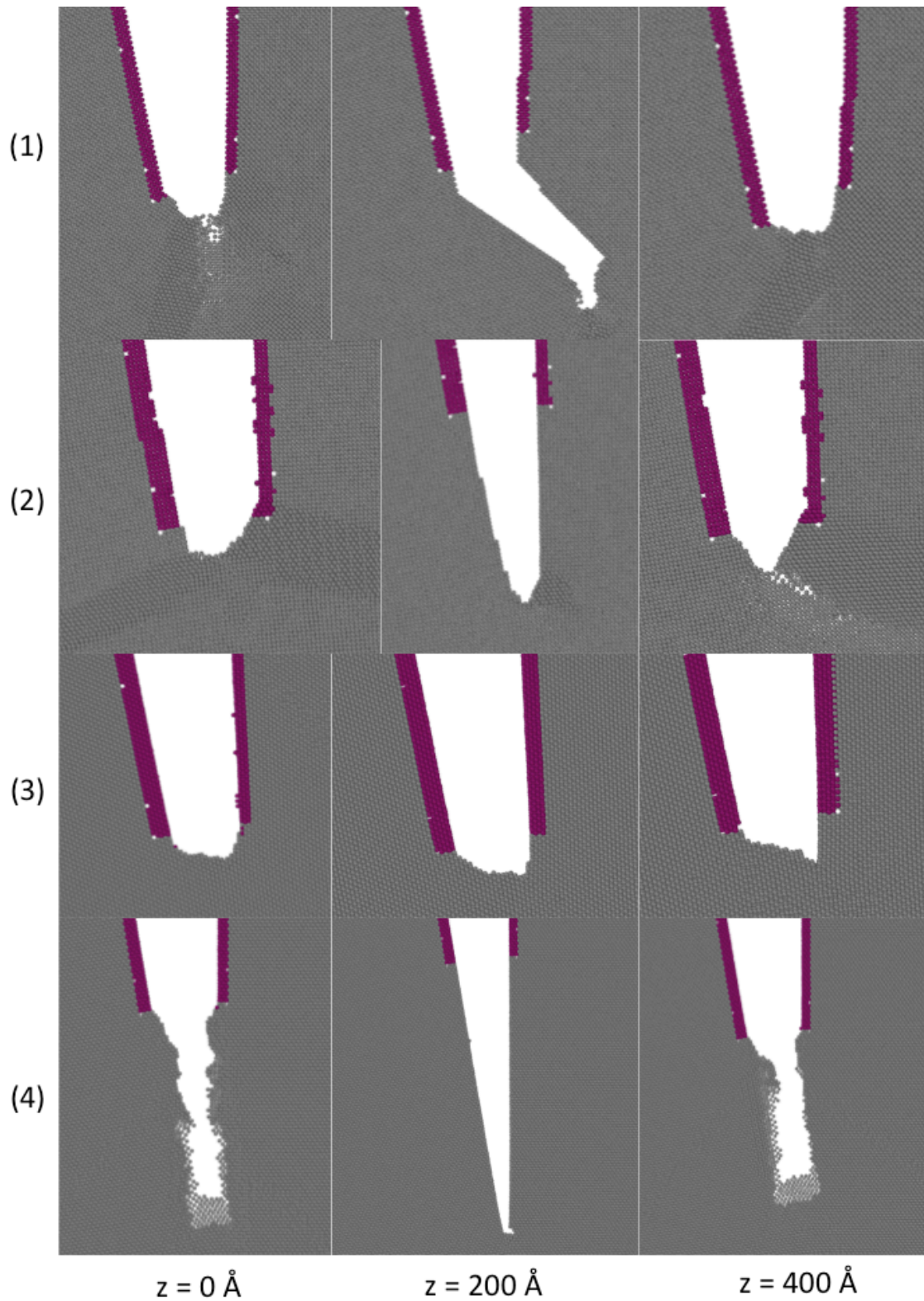


Figure 47: Through-thickness crack growth for cantilevers 1-4. CTOD(1) = 36.9 Å, CTOD(2) = 35.4 Å, CTOD(3) = 38.9 Å, CTOD(4) = 39.6 Å.

Appendix C: Input Script

The following is an example of the input script for cantilever 1.

```
#####  
#####  
# Simulation of a fib-milled beam with crack  
#  
# Beam party script made by the awesome duo of Marie and Jørn  
#  
#####  
#####  
  
# Dimensions and boundary conditions  
#package gpu 1 force  
package omp 8  
processors * 4 2  
dimension 3  
boundary s p p # Choose the type of boundary conditions to  
use in x-, y- and z-direction  
units metal # Determines the units that all  
properties will be given in  
  
# Define variables  
variable filename string orient1_round_short # Define  
ending of filename, to change name of log and dump files  
further down  
variable latlength equal 2.85896 # Unit cell length  
used for iron  
variable temp equal 300.0  
variable xlatfactor equal 1.0 # Normalization factor  
for y lattice direction.  
variable ylatfactor equal 1.0 # Normalization factor  
for x lattice direction.  
variable zlatfactor equal 1.0 # Normalization factor for z  
lattice direction.  
  
variable scale equal 20/latlength  
variable height equal ceil(scale*20/ylatfactor)  
variable heightx equal ceil(scale*20/xlatfactor)  
variable w equal ceil(scale*20/zlatfactor)  
variable halfw equal $w/2  
variable crackwall equal heightx*1  
variable crackbeam equal heightx*3  
variable length equal crackwall+crackbeam  
variable high equal height*0.75  
variable sidewidth equal $w*0.3  
variable low equal high+height  
variable loose equal ceil(scale*0.2)/xlatfactor  
variable fix equal ceil(scale*0.1)/xlatfactor  
variable wall equal loose+fix  
variable a equal height*0.3  
variable ctodL equal round(crackwall)-2
```

```

variable ctodR equal round({crackwall})+2
variable ctodCL equal {ctodL}+0.2
variable ctodCR equal {ctodR}-0.2
variable left equal {crackwall}-2
variable right equal {crackwall}+2
variable H1_hi equal 0.1/{ylatfactor}
variable H1_lo equal -0.1/{ylatfactor}
variable H2_hi equal -round($a*0.3)+0.1/{ylatfactor}
variable H2_lo equal -round($a*0.3)-0.1/{ylatfactor}
variable H3_hi equal -round($a*0.85)+0.1/{ylatfactor}
variable H3_lo equal -round($a*0.85)-0.1/{ylatfactor}
variable H4_hi equal -round($a)+0.1/{ylatfactor}
variable H4_lo equal -round($a)-0.1/{ylatfactor}

variable radius equal $w*0.25*({zlatfactor}/{xlatfactor})

variable highz equal $w+{sidewidth}
variable theta equal 45

variable cornerlength equal {length}-0.5*{heightx}
variable cornerheight equal {height}*0.2

variable          ts equal 0.0015
variable          trelax equal 200000 # Time-steps to relax
system initially
variable          trun equal 1000000 # Time-steps we wish to
run deformation
variable ramp equal -ramp(0.0,0.0035)

# Create geometry and atoms

lattice          bcc {latlength} orient x 1 0 0 orient y 0 1 0
orient z 0 0 1 # Orient bjelkefest!
region          box block -{wall} {length} -{low} {high} -
{sidewidth} {highz} # Size of the system in x-, y- and z-
direction, in units of the lattice unit length
create_box      7 box # Create the system box
region          bjelke block 0 {length} -{height} 0 0 $w
#Bjelkeutsikker
region          feste block -{wall} 0 INF INF INF INF
#Bakstykke
variable yz equal
0.5*$w*tan({theta}*3.14/180)*({zlatfactor}/{ylatfactor})
variable peak equal -{height}-{yz}
variable peak2 equal -{height}+{yz}

## variables for the rounding part
variable          round_r equal $w/4*{zlatfactor} # the radius
for the rounding part
variable          round_highy equal {round_r}/{ylatfactor}

```

```

variable      round_lowy equal -${height}-
${round_r}/${ylatfactor}
variable      round_highz equal $w+${round_r}/${zlatfactor}
variable      round_lowz equal -${round_r}/${zlatfactor}
variable      round_ry equal ${round_r}/${ylatfactor}
variable      round_rx equal ${round_r}/${xlatfactor}
variable      round_rz equal ${round_r}/${zlatfactor}

region        cyl_hiy cylinder z ${round_rx} ${round_highy}
${round_rx} INF INF side out
region        cyl_loy cylinder z ${round_rx} ${round_lowy}
${round_rx} INF INF side out
region        cyl_hiz cylinder y ${round_rx} ${round_highz}
${round_rx} INF INF side out
region        cyl_loz cylinder y ${round_rx} ${round_lowz}
${round_rx} INF INF side out
region        round_block block 0 ${round_rx} ${round_lowy}
${round_highy} ${round_lowz} ${round_highz}
region        round intersect 5 cyl_hiy cyl_loy cyl_hiz
cyl_loz round_block

variable      beardroundy equal ${peak}+${round_ry}/sin((90-
${theta})*3.14/180)/${ylatfactor}
variable      beardboxy equal ${peak}+${round_ry}*(1/sin((90-
${theta})*3.14/180)-sin((90-${theta})*3.14/180))/${ylatfactor}

region        cyl_beard cylinder x ${beardroundy} ${halfw}
${round_ry} 0 INF side out
#region      cyl_beard2 cylinder x ${beardroundy} ${halfw}
${round_rz} 20 INF side in
region        box_beard block 0 INF INF ${beardboxy} INF INF
side in

region        beardcut intersect 2 cyl_beard box_beard

# A = (xhi-xlo,0,0); B = (xy,yhi-ylo,0); C = (xz,yz,zhi-zlo)
region        bottomL prism 0 ${length} -${height} ${peak2} 0
${halfw} 0 0 -${yz}
region        bottomR prism 0 ${length} ${peak} -${height}
${halfw} $w 0 0 ${yz}

region        total union 5 round bjelke feste bottomL bottomR
create_atoms 1 region total # Create the atoms inside the
system box

delete_atoms region beardcut

# Potential
mass          * 55.845 # Atom mass

```

```

pair_style      eam/fs
pair_style      eam/fs/omp
pair_coeff      * * Fe_2.eam.fs Fe Fe Fe Fe Fe Fe Fe

# Define groups
region          fixed block -${wall} -${loose} INF INF INF INF
#Fixed atoms
group           fixed region fixed
group           mobile subtract all fixed
region          leftcrack block ${left} ${crackwall} -$a 0 INF
INF #Left of crack
group           leftcrack region leftcrack
region          rightcrack block ${crackwall} ${right} -$a 0 INF
INF #Right of crack
group           rightcrack region rightcrack
region          ctodL1 block ${ctodL} ${ctodCL} ${H1_lo}
${H1_hi} INF INF
region          ctodL2 block ${ctodL} ${ctodCL} ${H2_lo}
${H2_hi} INF INF
region          ctodL3 block ${ctodL} ${ctodCL} ${H3_lo}
${H3_hi} INF INF
region          ctodL4 block ${ctodL} ${ctodCL} ${H4_lo}
${H4_hi} INF INF
region          ctodR1 block ${ctodCR} ${ctodR} ${H1_lo}
${H1_hi} INF INF
region          ctodR2 block ${ctodCR} ${ctodR} ${H2_lo}
${H2_hi} INF INF
region          ctodR3 block ${ctodCR} ${ctodR} ${H3_lo}
${H3_hi} INF INF
region          ctodR4 block ${ctodCR} ${ctodR} ${H4_lo}
${H4_hi} INF INF
#region         corner block ${cornerlength} ${length} -
${cornerheight} 0 INF INF
region          corner sphere ${cornerlength} 0 ${halfw}
${radius}
group           corner region corner
#region         sprekk block ${crackwall} ${crackwall} -$a 0 INF
INF
#group          sprekk region sprekk
#delete_atoms  group sprekk

# Define which atoms to dump
variable        dumplength equal (2/3)*${length}
region          dump block 0 ${dumplength} INF INF INF INF
group           mdump region dump

group           ctodL1 region ctodL1
group           ctodL2 region ctodL2
group           ctodL3 region ctodL3
group           ctodL4 region ctodL4

group           ctodR1 region ctodR1

```

```

group          ctodR2 region ctodR2
group          ctodR3 region ctodR3
group          ctodR4 region ctodR4

group          ctodR union ctodR1 ctodR2 ctodR3 ctodR4
group          ctodL union ctodL1 ctodL2 ctodL3 ctodL4

set           group fixed type 2
set           group leftcrack type 3
set           group rightcrack type 4
set           group corner type 5
set           group ctodR type 6
set           group ctodL type 7

# Define some computes to be used for system and atom output
during simulation run
compute       myTemp mobile temp
compute       pot all pe/atom          # Computes
potential energy per atom
compute       stress all stress/atom NULL # Computes virial stress
per atom
variable      mises atom "0.707106781 * sqrt( (c_stress[1] -
c_stress[2])^2 + (c_stress[2] - c_stress[3])^2 + (c_stress[1]
- c_stress[3])^2 + 6*(c_stress[4]^2 + c_stress[5]^2 +
c_stress[6]^2))" # Computes the von Mises stress for each atom

compute       ctodL1x ctodL1 reduce ave x
compute       ctodL1y ctodL1 reduce ave y
compute       ctodL2x ctodL2 reduce ave x
compute       ctodL2y ctodL2 reduce ave y
compute       ctodL3x ctodL3 reduce ave x
compute       ctodL3y ctodL3 reduce ave y
compute       ctodL4x ctodL4 reduce ave x
compute       ctodL4y ctodL4 reduce ave y

compute       ctodR1x ctodR1 reduce ave x
compute       ctodR1y ctodR1 reduce ave y
compute       ctodR2x ctodR2 reduce ave x
compute       ctodR2y ctodR2 reduce ave y
compute       ctodR3x ctodR3 reduce ave x
compute       ctodR3y ctodR3 reduce ave y
compute       ctodR4x ctodR4 reduce ave x
compute       ctodR4y ctodR4 reduce ave y

compute       cornerx corner reduce ave x
compute       cornery corner reduce ave y

variable      ctod1 equal sqrt((sqrt((c_ctodL1x)^2)-
sqrt((c_ctodR1x)^2))^2+(sqrt((c_ctodL1y)^2)-
sqrt((c_ctodR1y)^2))^2)

```

```

variable ctod2 equal sqrt((sqrt((c_ctodL2x)^2)-
sqrt((c_ctodR2x)^2))^2+(sqrt((c_ctodL2y)^2)-
sqrt((c_ctodR2y)^2))^2)
variable ctod3 equal sqrt((sqrt((c_ctodL3x)^2)-
sqrt((c_ctodR3x)^2))^2+(sqrt((c_ctodL3y)^2)-
sqrt((c_ctodR3y)^2))^2)
variable ctod4 equal sqrt((sqrt((c_ctodL4x)^2)-
sqrt((c_ctodR4x)^2))^2+(sqrt((c_ctodL4y)^2)-
sqrt((c_ctodR4y)^2))^2)

# Initial velocities
velocity mobile create ${temp} 887723

# Fix to be used during relaxation
fix      1 mobile npt temp ${temp} ${temp} 0.1 drag 2.0 y 0.0
0.0 1.0 z 0.0 0.0 1.0 drag 2.0 couple none # Use NPT
ensemble with zero pressure in y- and z-directions
#fix      1 all nvt temp ${temp} ${temp} 0.1 drag 2.0

# Set timestep and temperature
timestep ${ts}
thermo      200

# fix CNA stuff
compute      cna all cna/atom 3.46
compute      current all reduce sum c_cna
thermo_style custom step temp c_current
run          0
variable cnaatom atom "c_cna == 3"
group        bcc variable cnaatom

# fix back thermo output
thermo_style custom step temp pxx pyy pzz ly v_ramp cpu
v_ctod1 v_ctod2 v_ctod3 v_ctod4 c_cornerx c_cornery c_ctodL1x
c_ctodR1x c_ctodL1y c_ctodR1y c_ctodL2x c_ctodR2x c_ctodL2y
c_ctodR2y c_ctodL3x c_ctodR3x c_ctodL3y c_ctodR3y c_ctodL4x
c_ctodR4x c_ctodL4y c_ctodR4y
thermo_modify temp myTemp
thermo_modify lost warn

# Relax the simulation with a crack
neigh_modify exclude type 3 4
delete_atoms overlap 0.01 all all
fix          balance all balance 100000 1.05 shift x 20
1.05
fix          yzbal all balance ${trelax} 1.05 shift yz 20
1.05

# Dump properties for each atom to file dump.indent
dump         1 mdump custom 50000 mdump.${filename}.* id type xs
ys zs c_pot v_mises

```

```

dump      2 all custom 100000 dump.${filename}.* id type xs ys
zs c_pot v_mises
fix      fixatoms fixed setforce 0.0 0.0 0.0

run      ${trelax}

reset_timestep 0

dump      bccdump bcc custom 500 dump.beta.${filename}.*
id type xs ys zs c_pot v_mises c_cna
dump      alphadump all custom 2500
dump.alpha.${filename}.* id type xs ys zs c_pot v_mises c_cna
dump_modify bccdump thresh c_cna != 3
dump_modify alphadump thresh c_cna != 3

restart   200000 restart.${filename}.*

# Run with deformation
unfix      1
fix      1 mobile nvt temp ${temp} ${temp} 0.1 drag 2.0
fix      move corner addforce 0.0 v_ramp 0.0
log      log.${filename} # Write to logfile
run      ${trun} # Number of timesteps to run with these
conditions

```


Appendix D: Risk Evaluation


Here follows the obligatory risk evaluation performed in the beginning of the semester.

NTNU	Kartlegging av risikofylt aktivitet			Utarbeidet av	Nummer	Dato
HMS				HMS-avd.	HMSRV2601	22.03.2011
		Godkjent av		Erstatter		
		Rektor		01.12.2006		

Enhet: IPM
Linjeleder: Christian Thaulow
Deltakere ved kartleggingen (m/ funksjon): Marie Jørum, student
(Ansv. veileder, student, evt. medveiledere, evt. andre m. kompetanse)
Kort beskrivelse av hovedaktivitet/hovedprosess: Masteroppgave Marie Jørum: Atomistic Modeling of Fracture Mechanics Testing
Er oppgaven rent teoretisk? (JA/NEI): Nei
(Ansv. veileder, Dersom «JA»: Beskriv kort aktiviteten i kartleggingskjemaet under. Risikovurdering trenger ikke å fylles ut.)
Signaturer: Ansv. veileder: *Chr. Thaulow* Student: *Marie Jørum*

Dato: 02.02.2015

ID nr.	Aktivitet/prosess	Ansv. ansvarlig	Eksisterende dokumentasjon	Eksisterende sikringstiltak	Lov, forskrift o.l.	Kommentar
1	Arbeid på PC, simuleringer, research	MJ		Ergonomisk mus, stol		
2	Bruk av supercomputer Vije	MJ	Brukermanual	Egen server til værmeldingen		

NTNU		Risikovurdering		Utarbeidet av		Nummer		Dato	
				HMS-avd.		HMSRV2601		22.03.2011	
HMS				Godkjent av				Erstatter	
				Rektor				01.12.2006	

Enhet: IPM **Dato:** 02.02.2015

Linjeleder: Christian Thaulow

Deltakere ved kartleggingen (m/ funksjon): Marie Jørum, student
(Ansv. Veileder, student, evt. medveiledere, evt. andre m. kompetanse)

Risikovurderingen gjelder hovedaktivitet: Masteroppgave Marie Jørum: Atomistic Modeling of Fracture Mechanics Testing

Signaturer: Ansvarlig veileder: *Jan. Thaulow* Student: *Marie Jørum*

ID nr	Aktivitet fra kartleggings-skjemaet	Mulig uønsket hendelse/ belastning	Vurdering av sannsynlighet (1-5)	Vurdering av konsekvens:			Risiko-verdi	Kommentarer/status Forslag til tiltak
				Menneske (A-E)	Ytre miljø (A-E)	ØK/ materiell dørmme (A-E)		
1	Databruk	Spenningsmerter i rygg/nakke, musearm, slitne øyne	3	B			3B	Ergonomisk stol og mus Ta hyppige pauser
2	Bruk av supercomputer	Krasje supercomputer	2		A		2A	Ikke bruke Æ, Ø, Å

Risikovurdering

Utarbeidet av	Nummer	Dato
HMS-avd.	HMSRV2601	22.03.2011
Godkjent av		Erstatter
Riktør		01.12.2006

Sannsynlighet vurderes etter følgende kriterier:

Svært liten 1	Liten 2	Middels 3	Stor 4	Svært stor 5
1 gang pr 50 år eller sjeldnere	1 gang pr 10 år eller sjeldnere	1 gang pr år eller sjeldnere	1 gang pr måned eller sjeldnere	Skjer ukjentlig

Konsekvens vurderes etter følgende kriterier:


Gradering	Menneske	Ytre miljø Vann, jord og luft	Øk./materieill	Omdømme
E Svært Alvorlig	Død	Svært langvarig og ikke reversibel skade	Drifts- eller aktivitetsstans > 1 år.	Troverdighet og respekt betydelig og varig svekket
D Alvorlig	Alvorlig personskade. Mulig utarhet.	Langvarig skade. Lang restitusjonstid	Driftstans > 1/2 år Aktivitetstans i opp til 1 år	Troverdighet og respekt betydelig svekket
C Moderat	Alvorlig personskade.	Mindre skade og lang restitusjonstid	Drifts- eller aktivitetsstans < 1 mnd	Troverdighet og respekt svekket
B Liten	Skade som krever medisinsk behandling	Mindre skade og kort restitusjonstid	Drifts- eller aktivitetsstans < 1 uke	Negativ påvirkning på troverdighet og respekt
A Svært liten	Skade som krever førstehjelp	Ubetydelig skade og kort restitusjonstid	Drifts- eller aktivitetsstans < 1 dag	Liten påvirkning på troverdighet og respekt

Risikoverdi = Sannsynlighet x Konsekvens

Beregn risikoverdi for Menneske. Enheten vurderer selv om de i tillegg vil beregne risikoverdi for Ytre miljø, Økonomi/materieill og Omdømme. I så fall beregnes disse hver for seg.

Til kolonnen "Kommentarer/status, forslag til forebyggende og korrigerende tiltak":

Tiltak kan påvirke både sannsynlighet og konsekvens. Prioriter tiltak som kan forhindre at hendelsen inntreffer, dvs. sannsynlighetsreduserende tiltak foran skjerpet beredskap, dvs. konsekvensreduserende tiltak.

NTNU		Risikomatrix		Dato	
				08.03.2010	
HMS/IKS				Erstatet	
		utarbeidet av		Nummer	
		HMS-avd.		HMS/IV2004	
		godkjent av			
		Faktor		09.02.2010	

MATRISSE FOR RISIKOVURDERINGER ved NTNU

		SANNSYNLIGHET				
		Svært liten	Liten	Middels	Stor	Svært stor
KONSEKVENNS	Svært alvorlig	E1	E2	E3	E4	E5
	Alvorlig	D1	D2	D3	D4	D5
	Moderat	C1	C2	C3	C4	C5
	Liten	B1	B2	B3	B4	B5
	Svært liten	A1	A2	A3	A4	A5

Prinsipp over akseptkriterium. Forklaring av fargene som er brukt i risikomatrixen.

Farge	Beskrivelse
Rød	Uakseptabel risiko. Tiltak skal gjennomføres for å redusere risikoen.
Gul	Vurderingsområde. Tiltak skal vurderes.
Grønn	Akseptabel risiko. Tiltak kan vurderes ut fra andre hensyn.